Creation of cold and dense ensembles of calcium atoms

Von der Fakultät für Mathematik und Physik der
Gottfried Wilhelm Leibniz Universität Hannover
zur Erlangung des Grades

Doktor der Naturwissenschaften
Dr. rer. nat.
genehmigte Dissertation
von

Dipl.-Phys. Felix Vogt
geboren am 13. Januar 1975 in Braunschweig

2009

Referent: Prof. Dr. Wolfgang Ertmer

Korreferent: Prof. Dr. Fritz Riehle

Tag der Promotion: 23. Juni 2009

Kurzzusammenfassung

Das Verhalten von kalten ($15\ \mu$K) Calcium-Atomen in einer geeigneten optischen Dipolfalle wurde untersucht. Prozesse, die die Phasenraumdichte des in der Dipolfalle gespeicherten Calcium-Ensembles begrenzen, wurden identifiziert und untersucht. Zusammen mit der experimentell bestimmten Grundzustands-Streulänge wurden die Aussichten für die Realisierung eines Calcium Bose-Einstein-Kondensats erörtert. Die Dipolfalle wurde so konzipiert, dass ihr Betrieb mit der Laserkühlung auf dem schmalen Interkombinationsübergang $4s^2\ {}^1\mathrm{S}_0 \rightarrow 4s4p\ {}^3\mathrm{P}_1$ bei 657 nm verträglich ist. Atome, die in einer auf dem Interkombinationsübergang operierenden magneto-optischen Falle gekühlt und gespeichert werden, können nur begrenzt in die Dipolfalle transferiert werden, da das 657 nm Laserlicht zur Photoassoziation von Ca_2-Molekülen führt, die aus der Dipolfalle verloren gehen. Die entsprechende Zweikörper-Verlustrate konnte zusammen mit der Einfangrate der Dipolfalle und den Verlustraten der magneto-optischen Falle in einem Modell erfaßt werden, das die Ladedynamik der Dipolfalle beschreibt. Eine maximale Steigerung der Phasenraumdichte des Calcium-Ensembles auf 0.045 konnte im Kreuzungsbereich zweier Dipolfallen erreicht werden. Der Transfer von Atomen aus einer Einzelfalle in den Kreuzungsbereich beider Fallen wird durch elastische Stöße hervorgerufen. Die Teilchenzahl im Kreuzungsbereich wird durch inelastische Dreikörper-Stöße begrenzt, deren Rate jedoch mehr als eine Größenordnung kleiner ist als die elastische Stoßrate. Die Ladedynamik des Kreuzungsbereichs wird durch ein Modell beschrieben, das die verschiedenen Raten berücksichtigt. Die Grundzustands-Streulänge wurde durch Photoassoziations-Spektroskopie unterhalb der $4s^2\ {}^1\mathrm{S}_0 + 4s4p^1\mathrm{P}_1$ Asymptote bestimmt. Im Vergleich zu früheren Messungen erlaubten verbesserte experimentelle Bedingungen einen größeren Bereich von Kernabständen zu erfassen. Die damit verbundenen genaueren Messungen liefern nun einen Bereich der Streulänge zwischen $340a_0$ und $700a_0$ und lösen damit die Diskrepanz zwischen den Ergebnissen früherer Messungen. Als Ergebnis der Untersuchungen ist es nun möglich den experimentell aussichtsreichsten Weg für die Erzeugung eines Calcium Bose-Einstein-Kondensats aufzuzeigen, das zahlreiche neue und faszinierende Forschungsmöglichkeiten bietet.

Schlagworte: kalte Calcium-Atome, optische Dipolfallen, elastische und inelastische Stöße, Photoassoziations-Spektroskopie

Abstract

The behavior of cold calcium atoms in a suitable optical dipole trap was investigated. Processes which limit the phase-space density of the calcium ensemble, stored in the dipole trap, were identified and investigated. The ground state scattering length was experimentally determined. The consideration of these results allowed to discuss the perspectives for the realization of a calcium Bose-Einstein condensate. The realized dipole trap is compatible with the laser cooling on the narrow intercombination transition $4s^2\ {}^1\mathrm{S}_0 \rightarrow 4s4p\ {}^3\mathrm{P}_1$ at 657 nm. The atoms are cooled and stored in a magneto-optical trap (MOT) operating on the intercombination transition. The transfer of the atoms from the MOT into the dipole trap is limited by density dependent losses, caused by the 657 nm radiation. This laser light induces the photoassociation of Ca_2 molecules, which can not be trapped in the dipole trap. The respective two-body loss rate and the capture rate of the dipole trap as well as the loss rates of the MOT could be combined in a model, which describes the loading dynamics of the dipole trap. A maximum phase-space density of 0.045 could be realized in the crossing region of two dipole traps, which are spatially overlapped. The number of particles in the crossing region is limited by inelastic three-body losses, whose loss rate is more than one order of magnitude smaller in comparison to the rate of elastic collisions. The loading dynamics of the crossing region is described by a model, which considers the different rates. The ground state scattering length was determined by photoassociation spectroscopy at the $4s^2\ {}^1\mathrm{S}_0 + 4s4p{}^1\mathrm{P}_1$ asymptote. In comparison to previous measurements the improved experimental conditions allowed to investigate with the photoassociation spectroscopy an enlarged range of internuclear separations. This was accompanied with a more accurate determination of the scattering length. Its value covers a range between $340a_0$ and $700a_0$ and resolves therefore the discrepancy between the results of previous measurements. As a result of the presented investigations it is now clear, which most promising methods can be employed to reach a calcium Bose-Einstein condensate with a number of fascinating novel research opportunities.

Keywords: cold calcium atoms, optical dipole traps, elastic and inelastic collisions, photoassociation spectroscopy

Contents

1 Introduction **9**

2 Laser cooling of calcium in a two-stage magneto-optical trap **15**
2.1 Calcium level scheme - standard Doppler cooling and narrow-line cooling . . . 15
2.2 Experimental setup . . . 16
2.3 Optimization of the phase-space density in the second stage of the magneto-optical trap . . . 21
2.3.1 Configuration of the quench laser beam . . . 22
2.3.2 Detuning of the cooling laser and magnetic field gradient . . . 24
2.3.3 Broad- and small-band spectrum of the cooling laser . . . 25
2.3.4 Conclusion . . . 26

3 Collisional properties of calcium atoms **29**
3.1 Photoassociation spectroscopy . . . 29
3.2 Experimental realization . . . 30
3.2.1 Photoassociation-induced loss coefficient . . . 32
3.3 Theoretical description . . . 33
3.4 Results . . . 36
3.4.1 Saturation behavior . . . 36
3.4.2 Level structure . . . 37
3.4.3 Scattering length . . . 38
3.5 Conclusion . . . 39

4 Optical dipole traps for calcium and their properties **41**
4.1 Theoretical description of the trapping potential . . . 41
4.2 An optical dipole trap suitable for calcium . . . 45
4.2.1 Experimental setup and measurement sequence . . . 45
4.2.2 Loading rate of the dipole trap . . . 48
4.2.3 Loss processes in the dipole trap . . . 50
4.2.4 Loading dynamics of the dipole trap . . . 54
4.3 Conclusion . . . 56

5 Crossed-beam optical dipole trap **59**
5.1 Characterization of the crossed-beam dipole trap . . . 60

5.1.1 Optical dipole potential - influence of gravity 60
5.1.2 Influence of the power ratio $P_{\mathrm{hor}}/P_{\mathrm{tilt}}$ on the sample properties 64
5.1.3 Adiabatic generation of the crossed-beam dipole trap 68
5.2 Three-body losses in the crossing region 70
5.3 Loading behavior of the crossing region 74
5.4 Conclusion 78

6 Conclusion and outlook **79**

Chapter 1

Introduction

During the last decades the creation and investigation of cold and dilute gases has enabled a great progress in the understanding of atomic and molecular physics. Moreover, microkelvin cold atomic samples found important applications for precision measurements, e. g. in time and frequency standards [Did04], and they are used to investigate ultracold collisions [Wei99, Jon06]. The experimental demonstration of fascinating quantum mechanical phenomenons like Bose-Einstein condensation and the creation and investigation of quantum gases [Ang02] are as well part of this research field.

An important tool for the creation and manipulation of these cold gaseous ensembles is the laser. Already in the 1970´s the cooling of atomic ensembles by laser radiation was suggested by Hänsch and Schawlow [Hän75]. In the 1980´s a successful deceleration of atoms could be demonstrated [Ert85, Pro85] as well as the cooling of an ensemble by an arrangement of six counterpropagating laser beams [Chu85], the so-called optical molasses. In 1987 the magneto-optical trap [Raa87] was developed, which combines the optical molasses with an inhomogeneous magnetic field and allows beside cooling a spatial confinement of the atoms.

The method of laser cooling provides cold dilute atomic clouds with temperatures below hundred microkelvin and offered the perspective for the experimental realization of the Bose-Einstein condensation, which was predicted by A. Einstein in 1925 [Ein25]. Based on S. N. Bose´s work on the statistics of photons [Bos24], Einstein concluded that in an ideal gas of massive non-interacting bosons[1] a large fraction of particles would occupy the lowest quantum state, if the gas temperature falls below a certain critical value. Particles can be regarded as wave packets with a spatial extension described by the thermal de Broglie wavelength $\lambda_{\mathrm{dB}} = \sqrt{h^2/(2\pi m k_{\mathrm{B}} T)}$, which depends on particle mass m and temperature T as well as the constants h (Planck´s constant) and k_{B} (Boltzmann´s constant). At the critical temperature the wavelength λ_{dB} becomes comparable to the particle distance and the wave packets start to overlap. The condition for this quantum-mechanical phase transition is achieved if $\rho_0 \lambda_{\mathrm{dB}}^3 = 2.612$, with ρ_0 as the peak atomic density[2]. To avoid a

[1] Bosons are particles with a zero or integer spin.

[2] For a harmonic trapping potential this condition is equivalent to $N_{\mathrm{c}} = 1.202(k_{\mathrm{B}}T)^3/(\hbar^3 \omega_x \omega_y \omega_z)$, with the critical number of atoms N_{c} and the oscillation frequencies $\omega_x, \omega_y, \omega_z$.

condensation into a liquid or solid sample before quantum-degeneracy is achieved, sample densities are necessary which are five orders of magnitude smaller than in earth atmosphere on the ground. Only at these densities ($\rho \approx 10^{15}$ cm^{-3}) the rate for the formation of molecules is significantly smaller than the elastic collision rate and the gas reaches a thermal equilibrium before molecules and clusters are created. The low density requires a sufficient long matter wavelength and therefore temperatures around a microkelvin to fulfill the condition of quantum-degeneracy.

Since the laser cooled ensemble temperatures are too high, it was necessary to develop a method to achieve temperatures around a microkelvin. This was done by evaporative cooling [Hes86] in a magnetic trap. By these means it became possible to achieve quantum-degeneracy for the three alkaline elements ^{87}Rb [And95], ^{23}Na [Dav95] and ^{7}Li [Bra95], seventy years after Einstein´s prediction.

With the Bose-Einstein condensate (BEC) a macroscopic matter wave is realized providing an ideal model system to experimentally investigate quantum phenomenons. Such phenomenons in solids can be modeled by a BEC in a periodic potential of an optical lattice. The optical lattice acts on the atoms of the BEC in the same way as the crystalline periodic potential on the electrons. With a ^{87}Rb BEC in an optical lattice the quantum phase transition from a superfluid to a Mott insulator could be demonstrated [Gre02]. Furthermore the dispersion of matter wave packets, realized by a BEC, could be controlled by using an optical periodic potential [Eie03].

Another important achievement of a BEC is the realization of a "laser" for matter waves. In analogy to a laser with light the atom laser generates a coherent atomic beam with a brightness that is orders of magnitude higher than that of conventional atomic beam sources [Blo99]. By means of a highly collimated and slow atomic beams it should be possible to create atom interferometers with a significant better signal-to-noise ratio than state of the art interferometers. In atom interferometry the wave character of the atoms is used comparable to the electromagnetic wave in optical interferometers. Here the mass of the particles offers the possibility to realize interferometers as inertial sensors for the determination of the gravitational acceleration g and the Newtonian gravitation constant G as well as the fine structure constant α.

For atom interferometric high precision experiments and for the realization of frequency standards the most abundant alkaline earth elements ^{24}Mg, ^{40}Ca and ^{88}Sr are of great importance. These elements possess no nuclear spin and a non-degenerate ground state, which does not split in external magnetic fields. Furthermore alkaline earth isotopes feature a very narrow intercombination transition between their singlet and triplet states, which enables high resolution atom interferometry. To benefit from the narrow linewidth and the insensitivity of the ground state to external magnetic fields, it is desirable to realize an alkaline earth BEC as a source for coherent matter waves.

Despite all efforts it was not possible to create an alkaline earth BEC until now. The electronic structure of these elements made it necessary to develop new cooling methods. After laser cooling on the singlet transition $^1S_0 - ^1P_1$ [Rus98, Kis94, Kat99a] the absence of a magnetic substructure of the ground state in alkaline earth elements prevents the application of sub-Doppler laser cooling techniques [Let88, Coh90].

Temperatures below the millikelvin range could be achieved after the development of Doppler cooling methods on the narrow intercombination transition $^1S_0 - ^3P_1$. This narrow-line cooling firstly succeed in ^{88}Sr [Kat99a, Vog99] and later in ^{40}Ca by artificially broadening (quenching) the upper level of the narrow line [Bin01]. In all cases the atoms are stored in a magneto-optical trap (MOT), which operates on the $^1S_0 - ^3P_1$ transition. The temperature of the atomic ensemble corresponds to one photon recoil of the cooling laser (400 nK) in the case of Sr and for Ca temperatures around 10 μK can be achieved.

The phase-space densities of up to 10^{-2} of the magneto-optical trapped Sr ensemble [Kat99a] was further increased in a crossed-beam far-off resonance optical dipole trap to a value of 0.1 [Ido00]. The achieved phase-space density in this dipole trap was limited by light-assisted two-body collisions, which occur during the loading of the crossed-beam trap. The laser which created the dipole trap operated at the so-called "magic wavelength". At this wavelength it is possible to trap the atoms and manipulate them like if they were in free space [Kat99b]. The trapping laser light of a specific polarization produces the same Stark shift of the ground state $^1S_0$ and of one Zeeman component of the excited state $^3P_1$. This allows narrow-line Doppler cooling inside the dipole trap and enables to transfer up to 80% of the MOT atoms into the dipole trap.

The necessary last step to reach quantum-degeneracy could be demonstrated for ^{174}Yb, which has a similar electronic structure as alkaline earth atoms and allows therefore direct comparisons. In a crossed-beam optical dipole trap the atoms were successfully evaporatively cooled towards BEC [Tak03a]. Here by gradually lowering the trapping potential the most energetic atoms were evaporated and the ensemble thermalized at a lower temperature. The evaporation process is driven by elastic collisions, whose corresponding rate is determined by the s-wave scattering length at microkelvin temperatures. The knowledge of the scattering length allows therefore to estimate the perspectives for the realization of a BEC. Here alkaline earth atoms offer an advantage in the investigation of cold collisions. The non-degenerate ground state simplifies the comparison between experiment and theory, which is more complicated for alkali atoms, due to their hyperfine structure in the ground state. A well established method for the investigation of cold collision properties is the analysis of the photoassociation process, in which to colliding ground state atoms form an excited molecule by absorbing a photon. The photoassociation process depends on the scattering properties of the ground state as well as of the excited molecular state. For alkaline earth-like atoms photoassociation spectroscopy was first applied in Ca [Zin00] and produced lately remarkable results for Sr [Yas06, Zel06] and Yb [Toj06]. Only for Ca data from molecular spectroscopy are available [All03], which allow to compare and verify the ground state scattering length, determined by photoassociation spectroscopy. Determinations of the Ca ground state s-wave scattering length showed different results: the value from classical molecular spectroscopy [All03] favors a longer scattering length between 250 a_0 and 1000 a_0 ($a_0 \approx 0.052918$ nm is the Bohr radius), whereas photoassociation measurements [Deg03] gave a length of 50 a_0 to 300 a_0. The results show a positive scattering length, which is considerably larger than the Sr length [Mic05] and

similar or larger than the ^{174}Yb ground state scattering length [Tak04]. Similar to ^{174}Yb, evaporative cooling in a crossed-beam optical dipole trap also seems to be a promising way to reach quantum-degeneracy in Ca.

Investigations showed, that the alternative route for the realization a Ca BEC in the metastable state $^3P_2$ is not successful. In the ensemble of the magnetically trapped metastable Ca atoms below $10\ \mu$K, the inelastic collision rates dominate the elastic ones, which prevents evaporative cooling [Han06]. However in the ground state, the perspectives for the realization of a Ca BEC seems to be promising. The Ca ensemble can be laser cooled down to temperatures around $10\ \mu$K. Similar to the very successful demonstration with Sr, the narrow-line cooled Ca atoms have been transfered to an optical dipole trap, operating at a magic wavelength. Previously the magic wavelengths of Ca have been experimentally determined [Deg04b] to 800 nm and $\approx 1\ \mu$m, which are well accessible for lasers.

This thesis had the purpose to address three questions, which are crucial for the realization of a calcium BEC:

- To clarify the discrepancy in the determined ground state scattering length,
- to find optimum conditions for an optical dipole trap with calcium and
- to identify and investigate the processes, which limit the phase-space densities in the dipole trap.

An improved value of the ground state scattering length has been determined by photoassociation spectroscopy. In comparison to the previous photoassociation measurements [Deg04a, Zin00], the new experimental conditions allowed to generate photoassociation spectra with a significant improved signal-to-noise ratio. With it an enlarged range of internuclear separations were accessible with the photoassociation spectroscopy, which allowed for a more accurate determination of the ground state scattering length.

An efficient loading of precooled atoms from the MOT into an optical dipole trap requires, that this trap is compatible with narrow-line Doppler cooling. This condition is realized if the dipole trap operates at a "magic wavelength". However investigations showed, that only one of the previously determined "magic wavelengths" promises an efficient transfer. By means of a model, which describes the narrow-line cooling inside a dipole trap, the choice of the optimal wavelength for the dipole trap will be explained. In order to find optimum conditions for the transfer of atoms from the MOT to the dipole trap a model was developed, which describes the loading process. A similar model is applied to describe the transfer of atoms from a single-beam dipole trap to a crossed-beam dipole trap.

From the analysis of the temporal decay of the number of atoms, stored in the dipole trap, the different loss processes could be identified. Of special interest are density dependent loss processes, which limit the phase-space densities. Considerable are losses due to the formation of molecules initiated by the light of the MOT as well as three-body losses at the highest densities, as they are expected in

a crossed-beam dipole trap. To distinguish between light-induced two-body losses and three-body losses, the decay measurements were carried out in a single-beam and in a crossed-beam dipole trap with and without light of the second stage of the MOT. The derived two-body loss coefficient was compared with the theoretical predictions of the photoassociation process at the asymptote of the intercombination transition [Ciu04]. The derived three-body loss constant was compared with other atomic species and with the expected elastic collision rates.

The thesis is organized as follows:

Chapter 2 describes the preparation of the $10\ \mu$K cold atomic ensemble in the two-stage magneto-optical trap. Special attention is paid to the preparation of a cold and dense sample in order to have optimum conditions for the transfer to an optical dipole trap. The chapter is introduced by a description of the experimental setup.

To evaluate the prospects for the creation of a ^{40}Ca BEC it is necessary to know the size and the sign of the ground state scattering length. The determination of the scattering length by photoassociation spectroscopy is therefore subject of the following chapter 3. Besides the scattering length an improved value of the atomic lifetime of the state $4s4p^1\mathrm{P}_1$ was derived.

In chapter 4 the transfer of atoms from the second stage of the magneto-optical trap to a suitable optical dipole trap for ^{40}Ca is investigated. As it was pointed out (see above), the choice of the wavelength of the dipole trapping laser is of importance for an efficient transfer of atoms. This circumstance is discussed at the beginning of the chapter, followed by a description of the dipole trap setup, realized with a laser of feasible wavelength. Subsequently a model is presented, which describes the loading and loss processes of the dipole trap. It appears that density dependent two-body losses limit the transfer of atoms, which are caused by the light of the MOT.

The realization of a crossed-beam optical dipole trap is the subject of chapter 5. It starts with a description of the trapping potential, which is created by two intersecting dipole traps. The transfer of atoms into the trap at the crossing region is analysed subsequently. The previously developed loading model for a single-beam dipole trap is adjusted for the crossed-beam trap. Here an additional loss process limits the transfer of atoms, caused by three-body collisions.

The present results will be concluded in chapter 6 and an outlook to further experiments and applications will be given.

Chapter 2

Laser cooling of calcium in a two-stage magneto-optical trap

In this chapter the preparation of a 10 μK cold ensemble of calcium atoms will be explained. After a discussion of the calcium level scheme and the cooling methods, the experimental setup will be described. Experimentally, the main focus is directed on the generation of a cold and dense ensemble of atoms, optimized for the transfer to an optical dipole trap, which will be investigated in detail in chapter 4.

2.1 Calcium level scheme - standard Doppler cooling and narrow-line cooling

The generation of a cold ensemble of ^{40}Ca atoms is performed by laser cooling in a two-stage magneto-optical trap (MOT) [Raa87, Met99]. The first stage uses the dipole allowed transition $4s^2\ {}^1\mathrm{S}_0$ - $4s4p\ {}^1\mathrm{P}_1$ in the singlet system at 423 nm (see fig. 2.1). However a small fraction of excited atoms (10^{-5}) [Bev89] decays via the $4s3d\ {}^1\mathrm{D}_2$ state into the metastable states $4s4p\ {}^3\mathrm{P}_2$ and $4s4p\ {}^3\mathrm{P}_1$ and is therefore lost from the MOT. This leak in the cooling cycle is closed by repumping atoms from the $4s3d\ {}^1\mathrm{D}_2$ state to the $4s5p\ {}^1\mathrm{P}_1$ state from which they subsequently decay into the ground state. The expected final temperature of the ensemble is given by the Doppler limit $T_\mathrm{D} = \frac{h\gamma_\mathrm{at}}{4\pi k_\mathrm{B}} = 0.8$ mK, where γ_at denotes the transition linewidth, k_B Boltzmann´s constant and h Planck´s constant. In the experiment ensemble temperatures of 1.5 mK can be realized.

The non-degenerate ground state of ^{40}Ca does not allow for sub-Doppler cooling [Let88, Coh90]. Hence to reach temperatures suitable for further evaporative cooling in an optical dipole trap other methods have to be applied. The second stage of the MOT uses the narrow intercombination line ($\gamma_\mathrm{at} = 2\pi \cdot 380$ Hz) between the ground state ${}^1\mathrm{S}_0$ and the triplet state ${}^3\mathrm{P}_1$ for laser cooling of the ensemble. This cooling method (narrow-line cooling [Vog99]) differs from the standard Doppler cooling on a strong transition as used in the first stage. The linewidth γ_at of the intercombi-

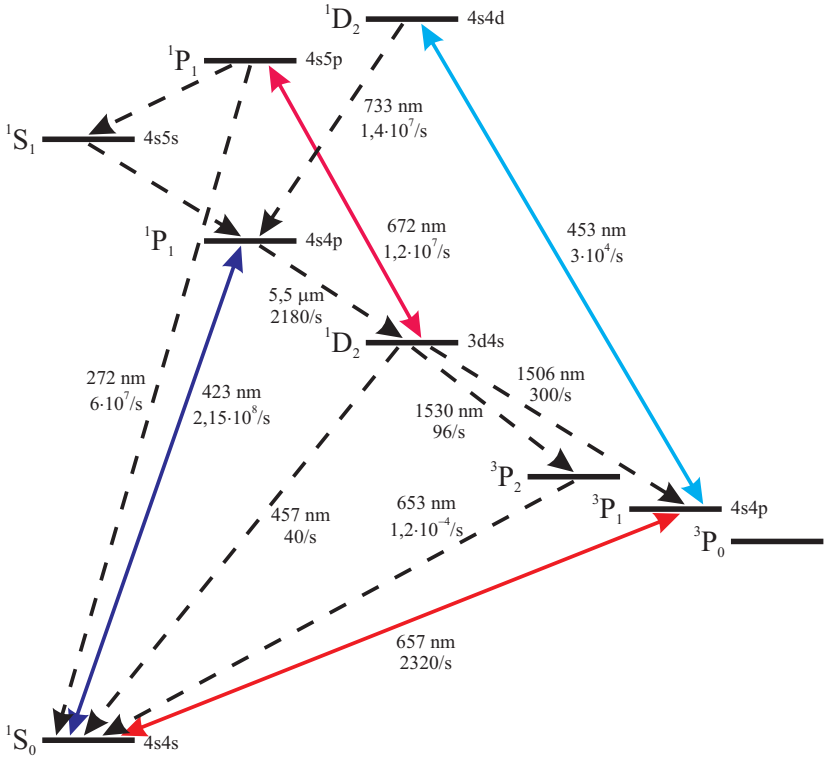

Figure 2.1: *Excerpt from the energy level diagram of ^{40}Ca. The optical transitions which are involved in the cooling scheme are shown as colored lines. The dashed lines indicate spontaneous decays. For the most relevant transitions the wavelengths and the corresponding Einstein A-coefficients are shown.*

nation transition is smaller than the change in the Doppler shift caused by the recoil of a single cooling photon $\frac{\hbar k_{ex}^2}{m} = 2\pi \cdot 23$ kHz, where m denotes the atomic mass and k_{ex} is the norm of the wave vector of the exciting light. It is therefore necessary to use a broad band of laser frequencies for efficient cooling since, otherwise an atom would be out of resonance after absorbing a cooling photon [Wal89]. If only a single frequency for cooling is used, another problem would be, that only a small range of velocities could be addressed. Because of the narrow intercombination line the cooling force is only 1.5 times larger than the gravitational force and its compensation by the cooling force is experimentally difficult. The scattering rate and therefore the cooling force is increased by an artificial reduction of the lifetime of the $4s4p\ ^3P_1$ state. This is done by exciting atoms from the $4s4p\ ^3P_1$ state to a third level ($4s4d\ ^1D_2$) from which they quickly decay via the $4s4p\ ^3P_1$ level to the ground state. With this so-called quench technique [Bin01, Cur01] temperatures of about $10\ \mu$K could be achieved.

2.2 Experimental setup

For the generation of a sample of cold calcium atoms an extensive experimental setup is needed. It mainly consists of different laser systems, which are necessary

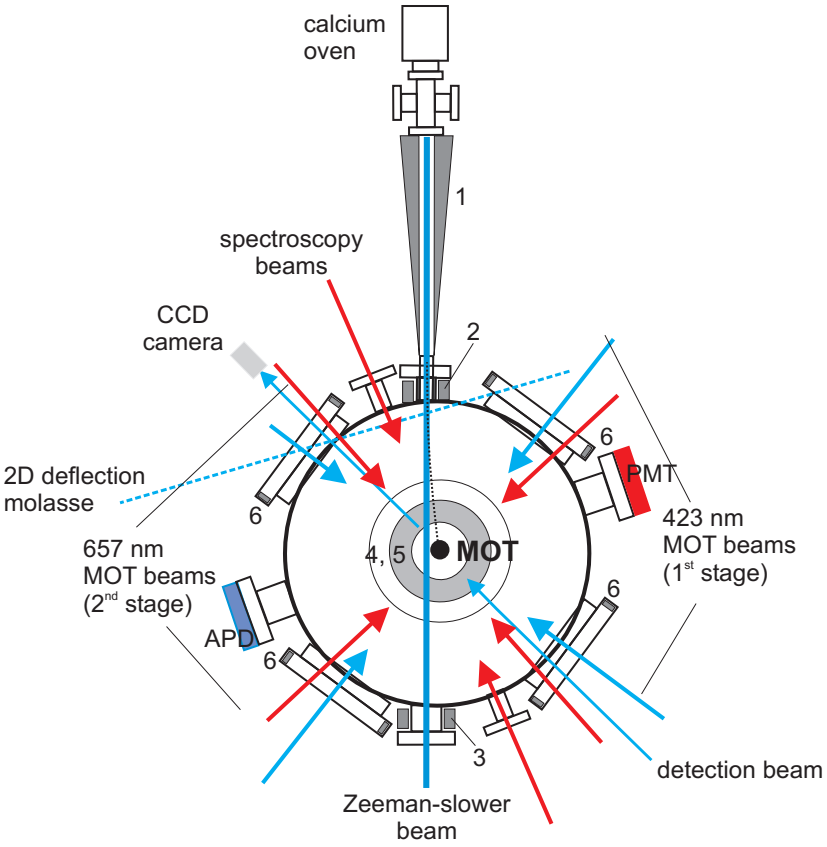

Figure 2.2: *Schematic sketch of the horizontal plane of the central part of the experiment. Illustrated are the relevant laser beams of the two-stage MOT and the spectroscopy and reference beams with its detection devices: photo multiplier tube (PMT) (657 nm fluorescence), avalanche photo diode (APD)(423 nm fluorescence) and CCD camera (absorption images). The different coils of the setup are depicted in grey: 1. main and 2. secondary coil (Zeeman slower), 3. counter coil, 4. quadrupole coils, 5. Helmholtz coils and 6. compensation coils.*

for cooling and detecting the atoms, of a vacuum chamber with the coils for the MOT inside and of a source of calcium atoms (for details see [Naz07]). A schematic drawing of the horizontal plane of the main part of the experimental setup is shown in figure 2.2. Table 2.1 summarizes the properties of the different laser beams needed at the experiment. Table 2.2 gives an overview of the magnetic fields used for preparation and detection of the atomic sample. In the spherical vacuum chamber a base pressure of 10^{-9} mbar is realized. The six main windows of the chamber and the windows for the Zeeman slower beam, the molasses beams and the spectroscopy beams have an antireflection coating in the visible range. For dipole traps six windows with coatings from the visible to the near infrared are available.

An oven filled with approximately 2 g of calcium granulate serves as a source of atoms. The oven consists of a stainless steel cylinder of 40 mm length and an inner diameter of 9 mm mounted in vacuum. The cylinder is surrounded by a wire, which heats the granulate up to 620°C. The evaporated hot atoms pass through a nozzle of

10 mm length, which consists of seven bores of 0.5 mm diameter. From their average initial velocity of 750 m/s the atoms are then decelerated by a Zeeman slower setup. This part consists of two coils with currents flowing in opposite directions and of cooling light, which is 510 MHz red-detuned from the $^1S_0$ - $^1P_1$ transition. Over the length of the main coil (300 mm), the spatially varying magnetic field makes sure, that the cooling light is always in resonance with the decelerating atoms at the corresponding position. Behind the main and the secondary coil, the magnetic field returns to zero and the laser is no longer in resonance with the slow atoms. At the end of the 380 mm long decelerating distance the atoms have a velocity of 40 m/s. A two-dimensional optical molasses collimates and deflects the slowed atomic beam by an angle of 15° into the center of the MOT.

The first stage of the MOT is generated by six independent, pairwise counter-propagating and mutually perpendicular laser beams and by a magnetic quadrupole field. The water cooled coils for the quadrupole field are placed inside the vacuum chamber, which allows a fast switching of the field within 200 μs. The two coils are in anti-Helmholtz configuration and create a quadrupole field gradient along the symmetry axis of 0.6 T/m at a current of 40 A. The symmetry axis is oriented along the vertical direction, which is denoted by the z-axis in the following.

For the second stage of the MOT the same coils are used at a lower current of 1 A (0.015 T/m). Here the pairs of counterpropagating circularly polarized beams are generated by retroreflection. In the vertical direction the beam of the quench laser (quench beam) is irradiated from below and retroreflected from the top. During the cooling the change in the Doppler shift and therefore the acceleration is significantly smaller than in the first stage of the MOT and the magnetic field gradient must be reduced. Otherwise, if the change of the Zeeman shift would become bigger than the change of the Doppler shift, the atoms run out of resonance and the cooling stops. Hence the second stage of the cooling is very sensitive to external magnetic fields. With three pairs of compensation coils these perturbations could be eliminated. Furthermore for the second stage of the MOT it is necessary to operate an additional coil, which compensates a magnetic field gradient of 0.5 mT/m caused by the second coil of the Zeeman slower setup [Naz07].

Beside cooling, the narrow intercombination line is also used for spectroscopy. Two counterpropagating beams are therefore sent into the chamber. In addition a homogeneous field is necessary, which is generated by a pair of coils in Helmholtz configuration. Each of the coils surrounds one of the quadrupole coils. The fluorescence light of the intercombination line is detected by a photo multiplier tube (PMT) and that of the 423 nm transition by an avalanche photo diode (APD). Inside the chamber plane convex lenses with a focal length of 90 mm collimates the 423 nm and the 657 nm fluorescence light. Afterwards a combination of a color and interference filter blocks remaining non-resonant light. The resonant detection beam is used to take 1:1 absorption images of the atomic cloud. The imaging system consists of two achromats with a resolution of ≈ 16 μm and a CCD-camera.

Table 2.1: Experimental parameters 1: Beam properties

beam	radius[1]	detuning	power
Zeeman slower	-	-510.0 MHz	22.5 mW
molasses	5 mm	-18.0 MHz	20.0 mW
1st MOT	10 mm	-28.0 MHz	0.6 mW
detection	4.2 mm	0.0 MHz	0.015 mW
2nd MOT	2.5 mm	-0.24 MHz	3.9 mW (hor.)
2nd MOT	2.5 mm	-0.24 MHz	7.8 mW (vert.)
quench	4 mm	-	80 mW
spectroscopy 1	1.85 mm	0.0 MHz	13.0 mW
spectroscopy 2	1.64 mm	0.0 MHz	10.2 mW

Table 2.2: Experimental parameters 2: Magnetic fields

coil	current	magentic field	magnetic field gradient
Zeeman slower (main coil)	9.8 A	0.1 T (B_{max})	-
Zeeman slower (secondary coil)	12.8 A	0.04 T	-
counter coil	13.0 A	-	0.5 mT/m
quadrupole coils (1st MOT)	25 A...80 A	-	0.015 T/(Am)
quadrupole coils (2nd MOT)	1.0 A...3.0 A	-	0.015 T/(Am)
Helmholtz coils	5 A	0.2 mT/A	-

The light for the first stage of the MOT, the Zeeman slower, the molasses as well as the detection beam is generated by a frequency doubled titanium-sapphire laser (Coherent MBR 110). As frequency doubler serves a lithiumtriborat crystal (LiB_3O_5, LBO) placed in an external built-up cavity (refer to [Deg04a]). The frequency of the 423 nm radiation is stabilized to a separate calcium atomic beam. In total an optical power of 0.5 W is available, which is subsequently split up by polarization optics and frequency shifted by acousto-optical modulators (AOM).

The number of stored atoms in the first stage of the MOT can be increased by a factor of three, if the decay channel across the $4s3d\ ^1D_2$ state is closed (see Fig. 2.1). This is done by repumping the atoms from $4s3d\ ^1D_2$ state to the $4s5p\ ^1P_1$ state. The corresponding laser radiation at 672 nm is generated by a diode laser (Toptica DL100) with an output power of 5 mW. It is stabilized by means of a lock-in technique to a cavity with fixed length. The cavity consists of a glass-ceramic spacer (Ohara Clear Ceram) with optically contacted mirrors. The long term drift amounts to approximately 30 MHz per year. The offset frequency between laser and cavity is

[1]The radius of a laser beam is defined at the point, where the intensity is decreased to $1/e^2$.

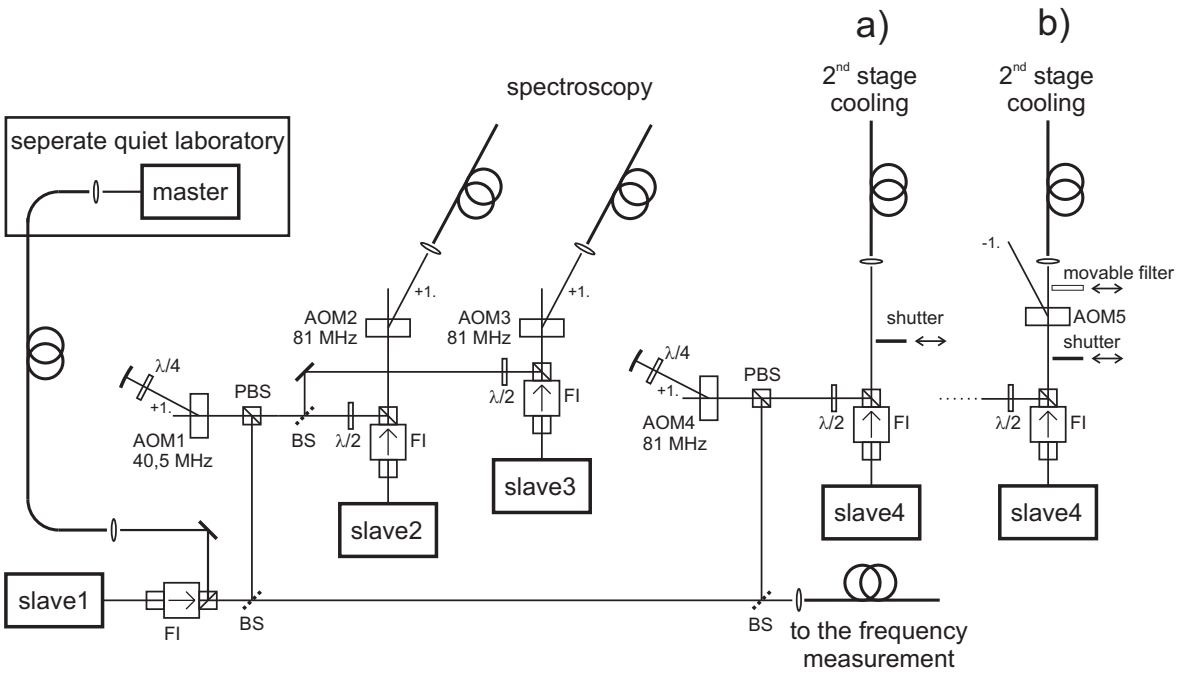

Figure 2.3: *The laser system at 657 nm for spectroscopy and the second stage of the MOT. The different slaves are injection locked to the stabilized light of the master. AOM: acousto-optic modulator, FI: Faraday isolator, BS: beam splitter, PBS: polarizing beam splitter, $\lambda/2$, $\lambda/4$: retardation plates. Second stage cooling without a) and with b) the possibility to reduce the optical power of the cooling light in the zeroth order of an AOM and additional by a movable filter glass.*

adjusted by a double pass AOM that also introduces the frequency modulation for the stabilization. In order to switch the repumping light, the first order of a further AOM is coupled into a fiber, which carries the light to the vacuum chamber.

The 657 nm radiation for the second stage of the MOT and for the spectroscopy is provided by a master diode laser, which injection locks slave diode lasers. The diode lasers are temperature stabilized and provide an optical output power of 50 mW (Mitsubishi, 120G14-01). The master laser is stabilized by the Pound-Drever-Hall technique [Dre83] to a reference cavity made of ultra low expansion glass. The temperature stabilized cavity is placed in vacuum. A special mounting reduces the sensitivity to vibrations [Naz07]. Beside its function as reference, the cavity furthermore serves as a filter for the high-frequency laser frequency noise [Naz07]. To minimize acoustic perturbations of the cavity, the whole setup of the master is situated in a separate quiet room. Hence the stabilized and filtered light is sent through a fiber to the experiment after an amplification of the power by a slave laser. Frequency fluctuations caused by the fiber are actively compensated [Sto04].

Figure 2.3 shows the setup at the calcium experiment. First the stabilized light coming through the fiber is amplified by slave 1. The main part of the light power is intended for possible frequency measurements and is therefore sent through a fiber to a frequency comb. The remaining light power serves for the injection lock of three

more slaves. Slave 2 and 3 are used for the spectroscopy beams and slave 4 generates the light for the second cooling stage. The spectroscopy beams are switched by AOMs. The radio frequency of the AOM4 (81 MHz) in front of slave 4 is sinusoidally frequency modulated ($f_{\mathrm{mod}} = 15$ kHz, peak-to-peak amplitude 0.75 MHz) in order to broaden the spectrum for the cooling light (see above 2.1). The modulation is realized by a voltage controlled oscillator (VCO), which is controlled by a frequency generator. Since the AOM is operated in double pass configuration the frequency of the cooling light is shifted by 162 MHz and the peak-to-peak amplitude of the generated cooling spectrum amounts to 1.5 MHz. To eliminate stray light at the experiment and to get more power, the cooling light is switched by a mechanical shutter based on a galvanometer with a moving magnet. Cooling light and spectroscopy light are sent through an optical fiber to the experiment.

For the cooling at the intercombination transition the quench technique is applied. As quench laser at 453 nm serves a commercial system (Toptica, TA/DL-SHG 110), which consists of a tunable, grating stabilized diode laser, a tapered amplifier and an external frequency doubling stage. The doubling stage is a folded ring cavity, which contains a potassium niobate crystal ($KNbO_3$). Up to 200 mW of optical power in the frequency doubled light can be achieved. The laser is stabilized to a tunable cavity. To assure long term stability, an additional laser is stabilized to the same cavity. The beat of this helium-neon laser with an iodine stabilized helium-neon laser is kept constant by means of the voltage at the piezo element of the cavity (cf. [Deg04a]). The 453 nm radiation is switched by an AOM, whose first order is coupled into a fiber, which carries the light to the experiment.

2.3 Optimization of the phase-space density in the second stage of the magneto-optical trap

The laser cooled ensemble in the two-stage MOT is intended to be transfered to an optical dipole trap. To a good approximation an optical dipole trap can be regarded as a conservative trap without any additional dissipation mechanism or thermalizing conditions beside elastic collisions. Therefore only atoms at the position of the dipole trap with sufficient low kinetic energy to remain trapped can be transfered from the MOT. This section investigates the optimum conditions for the creation of a high phase-space density in the second stage of the MOT, in order to have an ideal starting point for the loading of the dipole trap (see chapter 4).

As it was described above (see section 2.1) and illustrated in Figure 2.4, the two-stage cooling sequence starts with the 423 nm MOT loaded from the Zeeman slowed atomic beam by the two-dimensional deflection molasses. The loading of the first stage of the MOT is typically completed after a time of 1 s when the number of atoms saturated due to light-induced losses. At a quadrupole field of 0.38 T/m the number of stored atoms reaches $4.5 \cdot 10^8$ at a peak density of $1.4 \cdot 10^{10}$ cm^{-3} and a temperature of 2 mK (see table 2.3). After 1 s of first stage cooling, the second stage of the MOT followed by irradiating the atoms with the broadened spectrum of the

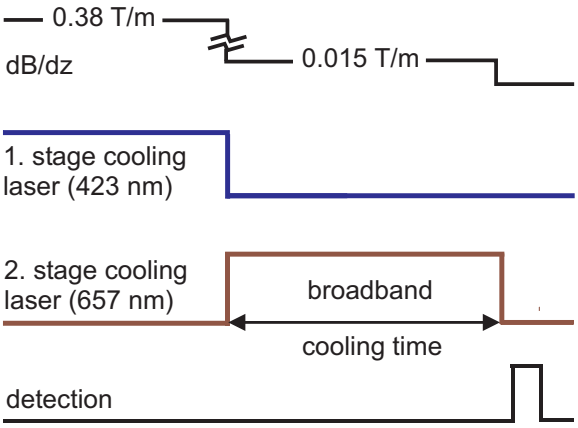

Figure 2.4: *Cooling sequence for the preparation of a 12 μK cold sample (refer to the text).*

657 nm cooling light together with the 453 nm quench light. Simultaneously the quadrupole gradient is reduced to a value of 0.015 T/m.

In the following subsections the configuration of the quench beams, the parameters of the 657 nm cooling light and the parameters of the magnetic field gradient are varied in order to find the optimum cooling conditions.

2.3.1 Configuration of the quench laser beam

The lowest temperatures and highest densities could be observed simultaneously only if the quench beam is realized as a standing wave in the vertical direction. If the quench beam irradiates the atoms in three directions (3 standing waves), the temperature increases by a factor of 1.5, the number of atoms and the density decreases to about one half. Here the cloud has a root mean square radius (rms) in the vertical direction of $\sigma_z = 0.33$ mm and in the horizontal plane of $\sigma_x = \sigma_y = 0.55$ mm. If the quench beam is only applied in the vertical direction the cloud radius in this direction amounts $\sigma_z = 0.26$ mm and $\sigma_x = \sigma_y = 0.63$ mm. The unfavorable conditions for three dimensional quench cooling are probably due to a higher total quench rate, which produces more 423 nm photons in the cooling cycle and a power imbalance between the beams, which results in a heating effect. This is connected with the loss of atoms with high kinetic energy, since observations for longer cooling times showed that the ensemble temperature falls to a value near 10 μK but this takes three times longer than in the case of only vertical quench cooling. Due to the quench effect, the cooling force is also increased in the horizontal plane which results in the smaller horizontal dimensions of the cloud.

After the first stage the quadrupole field is decreased within 200 μs to 0.015 T/m. The cooling spectrum is broadened to 1.5 MHz and its high frequency edge is detuned with respect to the resonance by about -240 kHz. Up to 15% of the atoms can be transfered to the second stage of the MOT. If the cooling transition is only quenched in the vertical direction the cooling is finished after a duration between 50 ms and 100 ms. The ensemble achieved a temperature around 10 μK, which

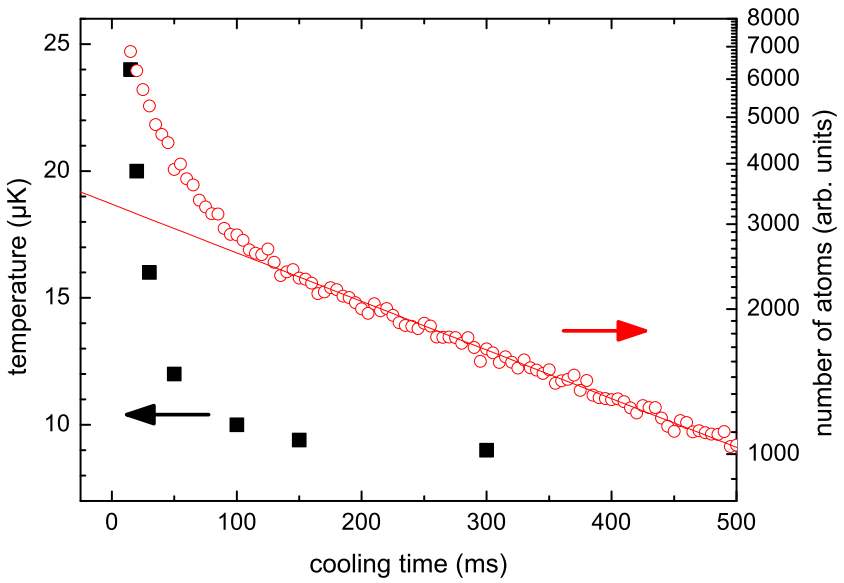

Figure 2.5: *Development of temperature (black squares) and number of atoms (red circles) as a function of cooling time, if quenching is only applied in the vertical direction. The particle numbers are measured by the blue fluorescence of the sample. After* 100 *ms the final temperature around* 10 μK *is reached. The initial fast decay of atoms is attributed to the loss of the hottest atoms. The measured lifetime of the MOT is between* 400 *ms and* 600 *ms (red line).*

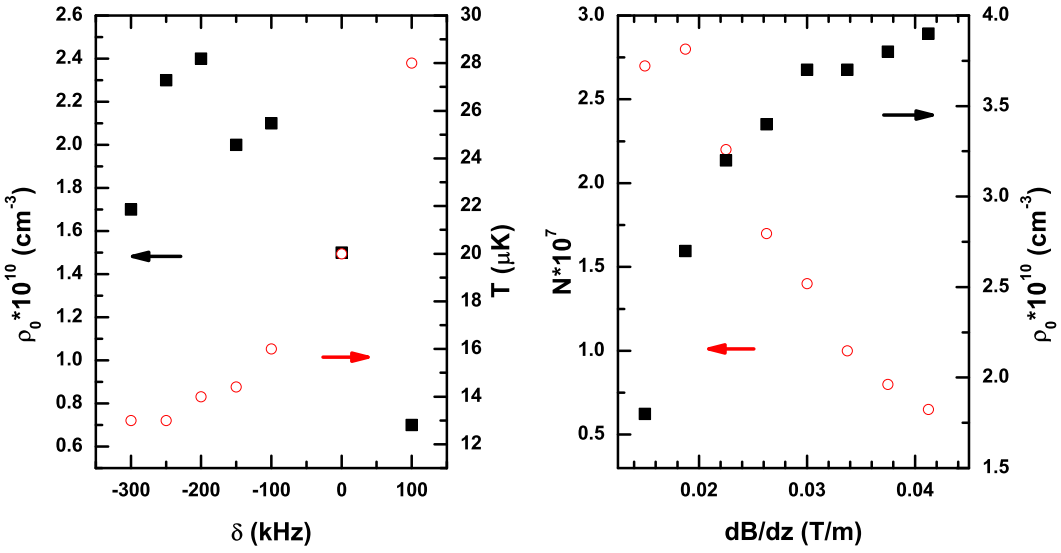

Figure 2.6: *Left: Temperature (red circles) and density (black squares) in the second stage of the MOT as function of the detuning of the high frequency edge of the cooling comb. The measurement was carried out at a quadrupole gradient of* 0.015 *T/m. Right: Number of atoms (red cicles) and the corresponding density (black squares) against the quadrupole gradient for a detuning of* −200 *kHz.*

changes for longer cooling times only marginally.

2.3.2 Detuning of the cooling laser and magnetic field gradient

The detuning of the high frequency edge of the cooling comb achieves the highest peak densities ρ_0 and lowest temperatures T around -200 kHz at a magnetic field gradient of 0.015 T/m (see fig. 2.6, left). An increase of the sample density can be realized by higher quadrupole fields. As can be seen in the right part of figure 2.6, the density starts to saturate at higher quadrupole fields around a two times higher density. The temperature is slightly increased (16 μK) but the number of atoms drops to a fourth of the value at 0.015 T/m. Therefore the atoms are captured at a low gradient (8 mT/m) of the magnetic field and subsequently the gradient is increased during 45 ms by a factor of four. With this compression sequence the number of atoms in the MOT is two times higher as if it would be in the case of a continuous loading at high gradient. The achieved phase-space density of an ensemble of $2.6 \cdot 10^7$ atoms is only 1.5 times higher in comparison to an ensemble of $4.9 \cdot 10^7$ atoms at a continuous loading at a lower gradient. If the sample is compressed in such a manner, a faster decay of atoms is observed than in the case of a continuous loading at a gradient of 1.5 G/cm. Density dependent losses are unlikely, if the estimated

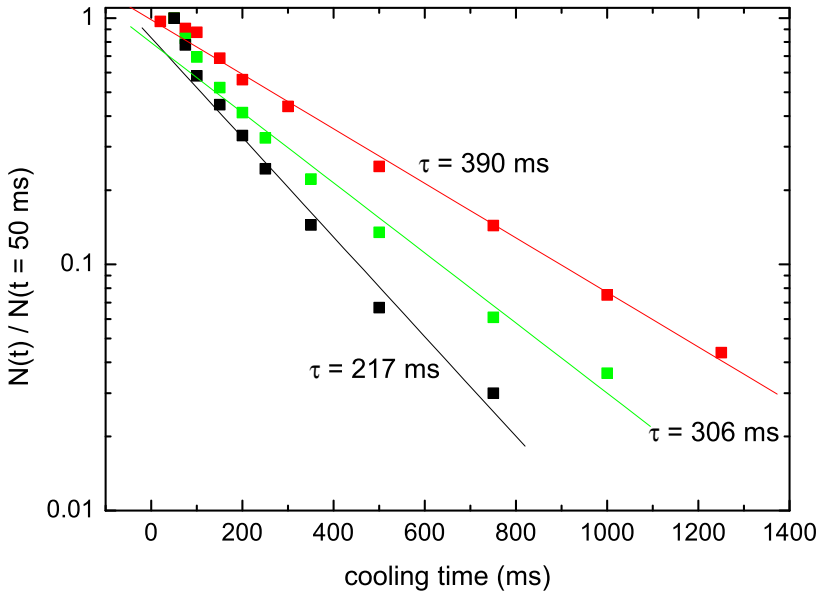

Figure 2.7: *Decay measurements of the second stage of the MOT. Red curve: the MOT is realized at a constant quadrupole field of* 0.015 *T/m and a detuning of* -250 *kHz. The quadrupole field is increased from* 8 *mT/m by a factor of four during the cycle (green curve). If in addition the detuning is decreased (*-200 *kHz) the highest densities and fastest decays are observed (black curve).*

two-body loss coefficient ($\beta \approx 2 \cdot 10^{-13}$ cm^3/s, see chapter 4) is taken into account, because the loss rates are two orders of magnitude smaller than the trap lifetime of about 0.5 s. Again in the denser and hotter samples the decay is given by the loss of atoms with high kinetic energy, comparable to the observations with the different configurations of the quench beam (see fig. 2.7).

2.3.3 Broad- and small-band spectrum of the cooling laser

In further investigations a decrease of the sample temperature could be realized by changing the laser spectrum of the cooling laser from broad-band to small-band comparable to the case of strontium [Kat99a]. The small-band consists of five single frequencies separated by 15 kHz and was realized by a VCO, controlled by a frequency generator. The VCO has two modulation inputs and can be controlled either by the frequency generator with which the broadened spectrum is generated or by that one for the small-band spectrum. A TTL-signal controls, which frequency generator modulates the VCO. Aside from the cooling spectrum a setup was realized, which allows a simultaneously reduction of the optical power in the cooling beam (see fig. 2.3b)). The zeroth order of an AOM (AOM5 in fig. 2.3b)) allows to vary the power between 100% and 50%. An additional filter glass, which was moved in the

Table 2.3: Parameters of the two-stage MOT

parameter	1.stage of the MOT	2.stage of the MOT
quadrupole field	0.38 T/m	0.015 T/m
intensity (horizontal beams)	0.5 mW/cm^2	40 mW/cm^2
intensity (vertical beams)	0.5 mW/cm^2	80 mW/cm^2
intensity (single quench beam)	–	320 mW/cm^2
detuning	-28 MHz	-240 kHz
comb width	–	1.5 MHz
temperature	2 mK	12 μK
peak density	$1.4 \cdot 10^{10}$ cm^{-3}	$3.2 \cdot 10^{10}$ cm^{-3}
number of atoms	$4.8 \cdot 10^8$	$4.5 \cdot 10^7$
trap radius	$\sigma_x = \sigma_y = \sigma_z = 1.3$ mm	$\sigma_x = \sigma_y = 0.63$ mm, $\sigma_z = 0.26$ mm
phase-space density	$2 \cdot 10^{-9}$	$1.5 \cdot 10^{-5}$

optical path, transmits 10% of this power. The filter glass is mounted on the movable arm of a mechanical shutter, realized in the same way as the shutter for switching the cooling light. After 50 ms of broad-band cooling the spectrum is switched to the small-band. Best results were obtained, when the center of the small-band spectrum was detuned by -400 kHz to the resonance. Furthermore the total optical power is decreased to 10% of the broad-band power. In this configuration a temperature of 7 μK and a density of $1.4 \cdot 10^{10}$ cm^{-3} (50% of the broad-band density) could be realized. The number of stored atoms was reduced to 50% of the atoms stored in the broad-band case.

2.3.4 Conclusion

The investigations of the second stage of the MOT showed the best conditions concerning density, temperature and lifetime, if a quenching of the cooling transitions is only applied in the vertical direction. Efforts to increase the density by compressing the sample by means of the quadrupole field resulted in a two times higher density, but this approach halves the number of atoms and the trap lifetime. A change of the cooling spectrum from broad- to small-band is by far not as successful as in the case of strontium [Kat99a]. The temperature only halves, in comparison to a decrease of one order of magnitude in the case of strontium. Also the number of atoms and the density halves in this approach. If the loading model of the dipole trap (see 4.2.2) is applied to the different sequences similar particle numbers are expected for the compression sequence and the sequence with a constant gradient of 0.015 T/m. Because of the better geometrical overlap between MOT and dipole trap when the gradient is ramped, the loading rate r_0 (see 4.2.2) could be increased by a factor of about five, however the smaller MOT lifetime (217 ms) and particle number as well

as the higher temperature ($17\ \mu$K) prevented a higher absolute number of atoms in the dipole trap. For the sequence with the change of the cooling spectra, a higher loading rate is expected, since the capture range is increased due to the lower temperature of the MOT atoms. However the absolute number of transfered atoms to the dipole trap is smaller, since the MOT contains less atoms ($1.4 \cdot 10^7$) compared to the MOT with constant low magnetic field gradient.

Because of the good reproducibility in the number of atoms, temperature and density, the further experiments with the dipole trap are carried out with a MOT realized at a constant low gradient of 0.015 T/m. Table 2.3 summarizes the optimum transfer conditions for the preparation of the second stage of the MOT.

Chapter 3

Collisional properties of calcium atoms

3.1 Photoassociation spectroscopy

The photoassociation measurements presented in this chapter were originally published in The European Physical Journal D **44**, 73-79 (2007). The results and considerations that are reproduced from there, are clarified by quotation marks. The subsection 3.2.1 and the sections 3.3, 3.4, 3.5 are completely cited.

Photoassociation (PA) describes the process if two colliding ground state atoms are excited to a bound molecular state by absorbing a photon, which is resonant with the molecular line. The generated molecule is in a vibrational level close to the dissociation limit, where the molecular properties are mainly determined by the long range part of the molecular potential. This region of the potential is easier to describe than the short range part and is directly related to atomic properties, such as the lifetime of the excited state and the ground state scattering length. In the case of ^{40}Ca, the theoretical description of the PA process is simplified by the non-degenerate ground state. The obtained PA spectra contain therefore informations of the interatomic collision properties of cold atoms. In contrast to the PA spectroscopy, the molecular spectroscopy investigates the deepest bound vibrational levels. A comparison of the results from both methods yielded a significant deviation in the calcium ground state scattering length [Deg03, All03]. Since an exact knowledge of the scattering length is necessary, to evaluate the perspective of the generation of a Ca BEC by evaporative cooling, a new PA measurement was carried out. It covers an extended energy interval of the B $^1\Sigma_u^+$ molecular state below the asymptote $4s^2\ ^1\mathrm{S}_0$ + $4s4p\ ^1\mathrm{P}_1$ (sec. 3.2). The measured PA spectra are theoretically described by a quantum mechanical model (sec. 3.3). "To precisely reproduce the observations and to determine absolute photoassociation rates, accurate potential curves are necessary for the ground and excited state. Via the adjusted potentials we gain access to the ground state scattering length and the dipole-dipole coupling constant C_3 of the excited state. In section 3.4 we discuss the results of the adjustment and give improved values for the lifetime of the atomic level $4s4p\ ^1\mathrm{P}_1$ and the ground state s-wave scattering length."

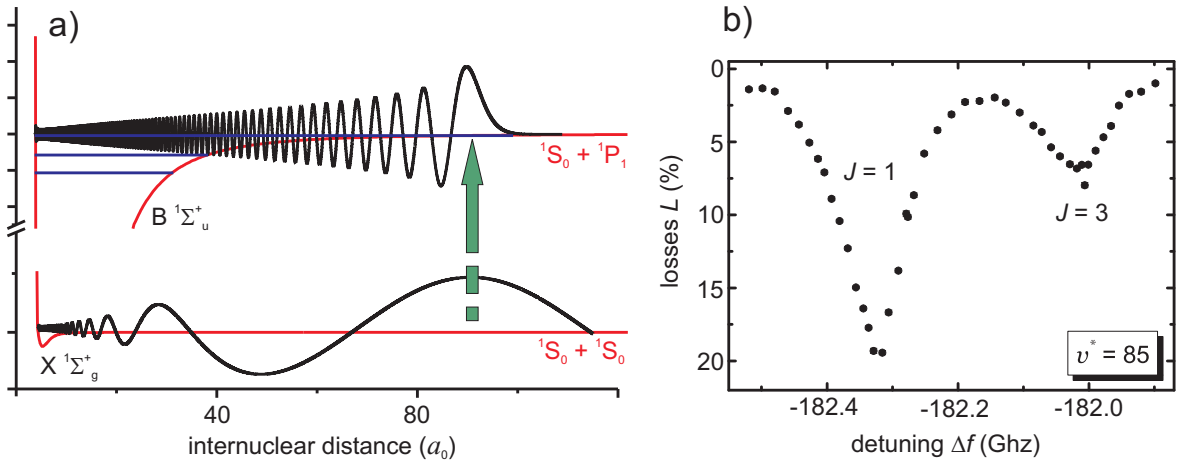

Figure 3.1: *Illustration of the photoassociation process. a) A pair of colliding ground state atoms, described by the s-wave scattering function (black curve in the lower part of the figure), is resonantly excited (green arrow) to a bound molecular state (black curve in the upper part of the figure) near the dissociation limit* $4s^2\ ^1S_0 + 4s4p\ ^1P_1$*. The corresponding molecular potentials of the ground* $X\ ^1\Sigma^+_g$ *and excited state* $B\ ^1\Sigma^+_u$ *are shown as red curves. The excitation to different molecular levels (blue lines in the upper part of the figure) probes the scattering wave function at different internuclear distances. The internuclear distance is given in units of the Bohr radius* a_0*. An example of such a photoassociation spectrum of the vibrational level* $v^* = 85$ *below the asymptote of state* $B\ ^1\Sigma^+_u$ *is shown in figure b). The detuning* Δf *is measured with respect to the dissociation limit* $4s^2\ ^1S_0 + 4s4p\ ^1P_1$*. At a temperature of* 1.5 *mK transitions to the rotational levels with quantum number* $J = 1$ *and* $J = 3$ *are observed.*

3.2 Experimental realization

The photoassociation (PA) measurements were carried out in the first stage of the MOT at a temperature of 1.5 mK. The frequency f_L of the PA laser is red-detuned ($\Delta f = f_L - f_0 \leq 0$) with respect to the $^1S_0 - ^1P_1$ transition frequency f_0. In the PA process a resonant photon excites two colliding ground state atoms to a bound molecular state $B\ ^1\Sigma^+_u$. "The spontaneous decay of the molecule produces with significant probability a pair of hot atoms, which is no longer trapped in the MOT. Thus, PA induces an additional, frequency dependent trap loss. The signature of this loss is a change of the number of trapped atoms." The PA induced trap loss achieves more than 35%, which is in comparison to previous PA measurements [Deg04a, Zin00] an increase of more than one order of magnitude. These clearly improved PA signals are due to an enhancement in lifetime (≤ 3 s) and peak density ($\approx 6 \cdot 10^{10}$ cm^{-3}) of the MOT. The former allows a longer illumination of the atomic cloud by the PA beam and more Ca_2 molecules will be generated and the latter results in a higher PA rate. "Under these improved experimental conditions it was possible to extend the region, in which photoassociation lines were observed, to 182 GHz below the asymptote. Typically, the maximum trap loss was kept below 20% by reducing the PA laser power to avoid saturation of the rotational lines." The increase in the den-

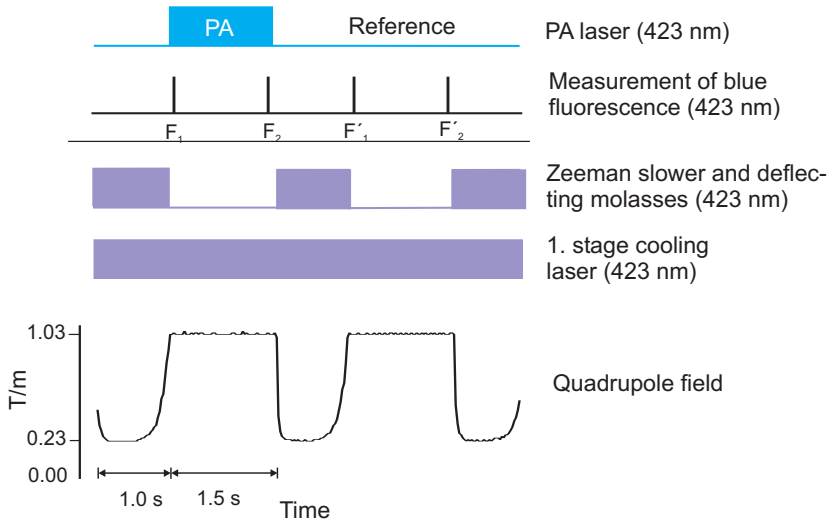

Figure 3.2: *Time sequence of the photoassociation measurement. At each detuning with respect to the atomic resonance the measurement consists of two cycles. The MOT is loaded at a low magnetic field gradient and subsequently compressed by increasing the gradient. The loading ends at the high gradient by switching off the Zeeman slower and the molasses. The generation of Ca_2 starts by shining in the photoassociation (PA) laser for 1.5 s. The blue fluorescence at the beginning and at the end of the PA process is detected (F_1, F_2) and compared with the respective fluorescence signals without the PA laser ($F´_1$, $F´_2$) in order to calculate the relative PA-induced losses L.*

sity is accomplished by an optimized loading scheme of the MOT: For 600 ms a high number of atoms are captured at a low gradient of the magnetic field of 0.23 T/m. In the following 400 ms the gradient is increased to a value of 1 T/m and the high densities are achieved. With this compression sequence the number of atoms in the MOT is 10 times higher compared to a continuous loading at a high gradient. The loading of the MOT is stopped by turning off the Zeeman slower and the deflection molasses. The atomic cloud is then illuminated by the PA laser for 1.5 s. At the beginning and at the end of the PA phase, the fluorescence of the atoms are detected by an avalanche photo diode. From the corresponding fluorescence signals (F_1 at the beginning, F_2 at the end) the fraction of remaining atoms $N = F_2/F_1$ is calculated. "The whole sequence of loading, ramping the gradient up and holding it for 1.5 s is repeated without the light from the photoassociation laser. Accordingly, the ratio $N' = F'_2/F'_1$ is determined that differs from N by the PA-induced losses." The relative PA losses L are then given by $L = 1 - N/N'$. Such a PA cycle is repeated for forty times at each detuning Δf to guarantee an optimum signal-to-noise ratio. Figure 3.2 summarizes the time sequence of the PA measurement. "For the first measurements, a standing wave was used for photoassociation. The intensity variation of the standing wave is included in the simulations to account for the different saturation behavior in nodes and antinodes. The standing wave was later omitted to simplify the theoretical description."

The PA laser is a frequency doubled titanium-sapphire laser, which is stabilized to a reference cavity to keep the laser frequency within ± 1 MHz. The AOM-switched

PA beam has a diameter of 3.8 mm. A spatial variation of the intensity is neglected in the quantitative description of the PA spectra, since the diameter of the atomic cloud only amounts to 1 mm. The typical peak intensity ranges between 2.0 W/cm^2 for $v^* = 72$ and 8.0 W/cm^2 for $v^* = 85$. "Here, the vibrational quantum number v^* is counted with respect to the asymptote [Zin00, Deg03], since the absolute assignment is unknown. Our calculations using an approximated potential for the state B give an absolute value for the vibrational assignment of about 177". Small detunings -73 GHz $\leq \Delta f \leq -65$ GHz are determined by observing the beat note between cooling and PA laser. Larger detunings -185 GHz $\leq \Delta f \leq -73$ GHz are measured by a wavelength meter and are calculated then from the calcium $^1S_0 - ^1P_1$ transition frequency of $709\ 078.382(1)$ GHz [Deg04a]. In both cases the determination of the detunings has an uncertainty of 1 MHz.

3.2.1 Photoassociation-induced loss coefficient

"The theoretical model, which we will describe in section 3.3, predicts the photoassociation-induced atomic density loss $\dot{\rho} = -\tilde{\beta}\rho^2$ using a loss coefficient $\tilde{\beta}$. This coefficient determines together with the background collision rate[1] γ_{MOT} the time evolution of the atom number $N(t)$ in the trap, when other many body effects can be neglected:

$$\begin{aligned} \dot{N} &= -\gamma_{\mathrm{MOT}} N - \tilde{\beta} \int d^3r \rho^2(\vec{r}) \\ &= -\gamma_{\mathrm{MOT}} N - \frac{\tilde{\beta}}{8\pi^{3/2}\sigma^3} N^2. \end{aligned} \tag{3.1}$$

Here, $\rho(\vec{r})$ is the local density and σ is the root-mean-square (rms) trap radius. We have assumed for the trap a Gaussian density distribution and that $\tilde{\beta}$ is constant over the trap dimension because of the wide photoassociation beam. This equation describes the decay correctly if no loading of the MOT is present, as it is the case in our experiment during the photoassociation phase. The solution of the differential equation 3.1 is

$$N(t) = N_0 \exp(-\gamma_{\mathrm{MOT}} t) \left[1 + \frac{N_0 \tilde{\beta} (1 - \exp(-\gamma_{\mathrm{MOT}} t))}{8\gamma_{\mathrm{MOT}} \sigma^3 \pi^{3/2}} \right]^{-1}, \tag{3.2}$$

with the initial atom number N_0. Equation 3.2 can be used to express the relative photoassociation-induced trap loss $L(t)$

$$L(t) = 1 - \left[1 + \frac{\rho_0 \tilde{\beta} (1 - \exp(-\gamma_{\mathrm{MOT}} t))}{2^{3/2} \gamma_{\mathrm{MOT}}} \right]^{-1}, \tag{3.3}$$

where we made use of the expression for the initial peak density ρ_0

$$\rho_0 = \frac{N_0}{(2\pi)^{3/2}\sigma^3}. \tag{3.4}$$

[1] Only in this chapter γ_{MOT} denotes the background collision rate of the first stage of the MOT. In the other chapters γ_{MOT} denotes the corresponding rate of the second stage of the MOT.

With the help of equation 3.3, one can express $\tilde{\beta}$ in terms of the experimentally observed trap loss L:

$$\tilde{\beta} = \frac{2^{3/2}\gamma_{\mathrm{MOT}}}{\rho_0(1-\exp(-\gamma_{\mathrm{MOT}}t))}\left(\frac{1}{1-L(t)}-1\right). \tag{3.5}$$

Note, that according to its definition at the beginning of this section $\tilde{\beta}$ depends neither on the PA time nor on the density. If the trap parameters ρ_0 and γ_{MOT} are known, it is possible to derive the absolute value of $\tilde{\beta}$ from the experimental results.

The trap lifetime $\gamma_{\mathrm{MOT}}^{-1}$ was determined several times during each PA measurement via recording the decrease of the trap fluorescence during hold times (> 10 s) at high MOT gradient. It showed a simple exponential decay at all times such that the assumption of negligible two and three-body losses is justified (compare eq. 3.1 for $\tilde{\beta} = 0$).

The peak density ρ_0 was determined by recording absorption images initially without imaging lens. We assumed cylindrical symmetry of the atomic cloud around the strong vertical axis and σ^3 in equation 3.4 is replaced by $\sigma_w^2\sigma_s$ for the weak and strong axis of the MOT, respectively. For high MOT gradient we observed peak densities ρ_0 between $3 \cdot 10^{10}$ cm^{-3} and $9 \cdot 10^{10}$ cm^{-3}. Additionally, we took absorption pictures of the released cloud and modeled the expansion using the atomic temperature, which is known from spectroscopy of the Doppler-broadened intercombination line $^3\mathrm{P}_1 - ^1\mathrm{S}_0$ [Deg05]. These measurements showed that the density deduced from earlier absorption images was slightly too small, probably due to a cloud seemingly enlarged by diffraction effects. Modeling the diffraction effects and later adding a lens to image the shadow of the cloud on the CCD-camera yielded that though the absolute measured densities are at most a factor of 2 too small, the relative densities are correct within a few percent. Hence, the experimentally determined absolute values of $\tilde{\beta}$ from equation 3.5 have a large uncertainty due to the renormalization of the density but relative ones can be compared with theory with high accuracy."

3.3 Theoretical description

"The trap loss signal, which is experimentally observed, depends on three factors: the excitation process, the subsequent decay mechanism including the recapture probability and the response of the trap to the PA-induced losses. The combination of the first two factors leads to the photoassociative loss coefficient $\tilde{\beta}$, which was introduced in section 3.2.1. The trap response on the PA-induced losses was analyzed in the same section. The aim of this section is the theoretical modeling of $\tilde{\beta}$. If $\tilde{\beta}$ is known for the experimental conditions of laser power and frequency, as well as for a given temperature of the atoms in the trap, the relative losses can be calculated according to equation 3.3.

To calculate the $\tilde{\beta}$ parameter, we follow the approach developed by Bohn and Julienne [Boh99] that can be applied very successfully for the description of photoassociation spectra [Lis02]. Using the reflexion approximation, the excitation /

stimulated emission rate $\Gamma/\hbar$ and the light shift E_1 of the transition due to coupling of the photoassociation laser field can be calculated:

$$\Gamma = 2\pi (V_{\mathrm{rad}})^2 \left(\frac{\partial E_b}{\partial v}\right) \frac{|f_0(R_C)|^2}{D_C}, \tag{3.6}$$

$$E_1 = -\pi (V_{\mathrm{rad}})^2 \left(\frac{\partial E_b}{\partial v}\right) \frac{f_0(R_C) g_0(R_C)}{D_C}. \tag{3.7}$$

This requires for a given collision energy ϵ the regular (f_0) and irregular (g_0) scattering wave function of ground state atoms at the Condon point R_C. Note the minus sign in equation 3.7, which corrects a typing error in equation (3.7) in reference [Boh99]. The vibrational spacing in the excited state B $^1\Sigma_u^+$ is expressed by $\partial E_b/\partial v$ at the energy of the molecular level (E_b). The ground state asymptote $^1\mathrm{S}_0$+$^1\mathrm{S}_0$ serves as energy reference.

V_{rad} is the radiative coupling between the continuum state and the excited bound molecular level. It incorporates selection rules and relative transition strengths to different rotational levels J from various partial waves ℓ according to the Wigner-Eckart theorem [Edm57] for a transition $\ell, m_\ell \rightarrow J, M$ for polarization q ($q = 0$: π polarization; $q = \pm 1$: $\sigma^\pm$ polarization):

$$\begin{aligned} (V_{\mathrm{rad}})^2 &= \frac{3\pi c^2 h}{\tau \omega^3} \frac{I}{4} f_{\mathrm{mol}}(R_C)(2\ell+1)(2J+1) \\ &\cdot \begin{pmatrix} \ell & 1 & J \\ m_\ell & q & -M \end{pmatrix}^2 \begin{pmatrix} \ell & 1 & J \\ 0 & 0 & 0 \end{pmatrix}^2. \end{aligned} \tag{3.8}$$

Here, τ is the lifetime of the atomic level $4s4p\ ^1\mathrm{P}_1$, ω denotes the angular transition frequency of the $^1\mathrm{S}_0$ to $^1\mathrm{P}_1$ transition, and I is the intensity of the PA laser field. The function $f_{\mathrm{mol}}(R)$ describes retardation effects of the dipole moment and is given in equation (4) of [Mac01]. The zeros in the second $3J$ symbol appear, since we are dealing with a so called parallel transition between two $^1\Sigma$ states.

Additionally, the derivative of the potential $U(R)$ of the excited state is needed at the Condon point

$$D_C \equiv \left.\frac{\partial U}{\partial R}\right|_{R_C}. \tag{3.9}$$

The regular and irregular wave functions are determined using the potential curve of the ground state given in reference [All03] as starting point. The B state potential curve is represented at large internuclear distance by the atomic pair energy D for $^1\mathrm{S}_0$+$^1\mathrm{P}_1$, dispersion coefficients C_3 and C_6, and the rotational barrier involving the reduced mass μ:

$$U(R) = D - \frac{C_3}{R^3} f_{\mathrm{ret}} - \frac{C_6}{R^6} + \frac{\hbar^2[J(J+1)+2]}{2\mu R^2}. \tag{3.10}$$

f_{ret} denotes the retardation of the resonant dipole-dipole interaction according to e.g. equation (3) in [Mac01]. The inner part of the potential ($R < 0.95$ nm) is

replaced by a boundary condition following the idea of the accumulated phase method [Cru99]. The boundary condition and the dipole-dipole coupling constant C_3 can be adjusted to match the observed level structure. The constant C_6 is included to check the sensitivity of the C_3 determination on higher order dispersion coefficients.

We checked the validity of the reflexion approximation, on which the formalism relies, by comparison with calculations involving the full integration over both wave functions. For this purpose, the potential of the state B had to be parametrized over the full range of internuclear distance, and the inner part was taken from reference [All04]. No significant deviation was found. Thus it was possible to use the reflexion approximation to reduce the numerical effort to a level that allows for systematical investigations of different experimental conditions and potentials.

Values of Γ and E_1 were tabulated for the vibrational and rotational levels of interest for a series of collision energies ϵ with $h \cdot 500$ kHz energy spacing at the respective experimental PA laser intensity. Partial waves ℓ are considered up to $\ell = 6$. Using Γ and E_1, the excitation probability $|S|^2$ to a given molecular level (v^*, J) can be expressed by

$$|S(\Delta, \epsilon, \ell, v^*, J)|^2 = \frac{1}{2\ell+1} \sum_{m_\ell} \frac{\hbar\gamma\Gamma(m_\ell)}{[\epsilon - (\Delta + E_1(m_\ell))]^2 + \left(\frac{\hbar\gamma + \Gamma(m_\ell)}{2}\right)^2}. \tag{3.11}$$

The decay rate γ is determined by the lifetime of the excited molecular level, which is for the long range levels of the state B in good approximation twice the atomic lifetime of the level $4s4p\ ^1\mathrm{P}_1$. The detuning $\Delta/h = [\nu(v^*, J) - \nu_\mathrm{L}]$ is defined between the molecular level at energy $h\nu(v^*, J)$ and the laser frequency ν_L.

We define a modified trap loss probability S^*, that reflects the probability that a spontaneous decay leads to a trap loss

$$|S^*|^2 = (1-p)|S|^2. \tag{3.12}$$

The pre-factor $(1-p)$ in equation 3.12 takes into account the probability p that a decay does not lead to a trap loss. Simulations of our MOT show that decay processes that produce atom pairs with a kinetic energy of below 0.7 K lead most likely to a recapture and therefore do not appear as trap loss. The probability of such decay processes can be calculated within the Franck-Condon approximation, which is well justified for the long range part, at which the decay predominantly takes place. The recapture probability p is calculated for each molecular level (v^*, J) summing over outgoing partial waves ℓ. It is in the order of 40% to 25% for v^* considered in this work.

Integrating $|S^*|^2$ over collision energies ϵ assuming a Boltzmann distribution in the trap and summing over ℓ yields the trap loss parameter $\tilde{\beta}$

$$\tilde{\beta}(\Delta, v^*, J) = \frac{2}{hQ_T} \sum_\ell (2\ell+1) \int d\epsilon \exp(-\epsilon/k_B T) \left|S_\ell^*\right|^2. \tag{3.13}$$

The factor 2 accounts for the fact that two atoms are lost if one molecule is decaying. The integration is truncated for high energies at values, for which the Boltzmann

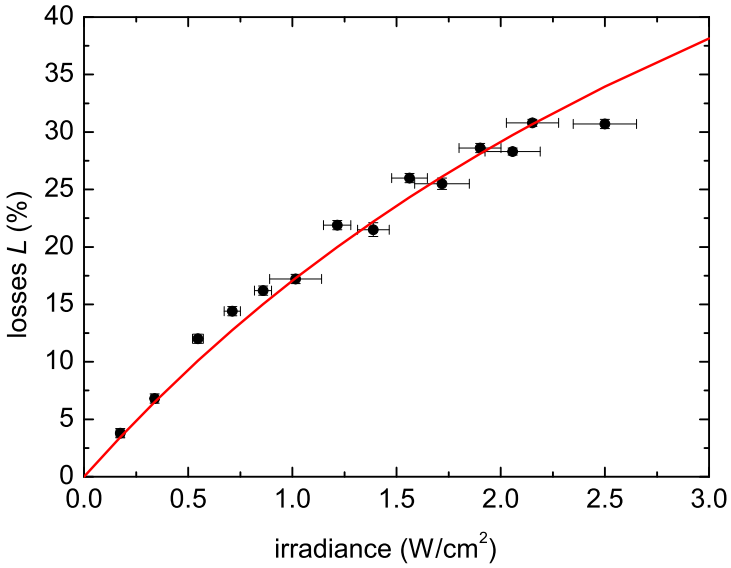

Figure 3.3: *Saturation behaviour of the photoassociation resonance* $v^* = 72$, $J = 1$. *The line is a fit according to equation 3.3 assuming a linear dependence of* $\tilde{\beta}$ *on the irradiance.*

factor has dropped to 10^{-4} of its maximum value for the experimentally determined atom temperature T. Q_T is the partition function for the atomic temperature T

$$Q_T = \left(\frac{2\pi\mu k_B T}{h^2}\right)^{3/2}. \tag{3.14}$$

Knowing our experimental conditions, equations 3.13 and 3.3 can be used to quantitatively describe the observed photoassociation spectra. As we will discuss in section 3.4.3, the relative intensity of the rotational lines is very sensitive to the ground state scattering wave function and in particular to the ground state scattering length [Tie96]."

3.4 Results

3.4.1 Saturation behavior

"To compare the relative intensities of the rotational lines belonging to one vibrational level observed by photoassociation, it is important to avoid saturation of the trap loss and thus leveling of the line intensities. On the other hand, strong signals with good signal-to-noise ratio are preferable for a precise determination of the line intensity.

Since we observe comparatively high atom loss and accordant density reduction, saturation due to the depletion of the trap can be expected [Wes04]. This effect

v^*	$J = 1$	$J = 3$	R_C
85	−182.470(10)	−182.115(10)	4.4 nm
80	−126.611(10)	−126.323(10)	5.0 nm
72	−67.087(10)	−66.901(10)	6.2 nm
69	−51.916(10)	−51.777(10)	6.7 nm

Table 3.1: *Summary of level binding energies E_b in the B $^1\Sigma_u^+$ potential curve determined by the line shape simulations (see text). The corresponding detunings E_b/h from the asymptote are given in GHz. The last column gives the classical outer turning point R_C.*

depends on the number of photoassociated molecules and therefore on the PA laser intensity and the photoassociation time. But saturation may also arise from the irradiance dependence of the PA loss coefficient $\tilde{\beta}$ itself.

To distinguish both processes and to determine a good working point, we have measured relative trap loss L as a function of the PA laser irradiance on the line $v^* = 72$, $J = 1$. The results are shown in figure 3.3, saturation is clearly visible. The line depicts a fit of the observed trap loss by equation 3.3 under the assumption that $\tilde{\beta}$ is proportional to the irradiance, thus not saturated. Only this proportionality constant was fitted, the other quantities in equation 3.3 were determined independently.

The good description of the data by the fit shows that the saturation is due to the depletion of atoms from the trap by photoassociative-induced losses. Indications for the saturation of $\tilde{\beta}$ are not visible. For the experiments described below, the irradiance was chosen such that a trap loss of 25% was not exceeded."

3.4.2 Level structure

"The newly observed photoassociative resonances down to -182 GHz below the asymptote $4s^2\ ^1\mathrm{S}_0 + 4s4p\ ^1\mathrm{P}_1$ allowed for an improved long range description of the state B $^1\Sigma_u^+$. The asymptotic model described in section 3.3 was used to fit the observed level energies. Since the classical outer turning point of $v^* = 85$ is located at 4.4 nm only, the potential description (see eq. 3.10) was extended with respect to reference [Deg03] by the van der Waals coefficient C_6. As energy reference the lowest asymptote $4s^2\ ^1\mathrm{S}_0 + 4s^2\ ^1\mathrm{S}_0$ was chosen. Hence the atomic pair energy D is given by the transition energy $\hbar\omega$ of the Ca resonance line $^1\mathrm{S}_0 - ^1\mathrm{P}_1$.

In the determination of the level energies from the photoassociation spectra, special care has to be taken to avoid errors by two effects: most importantly, the thermal averaging (see equation 3.13) leads to a line shift, which is not negligible at a temperature of the atom cloud of 1.5 mK. Secondly, light shifts as described by equation 3.7 can be significant.

Both effects can be modeled quantitatively by the formalism described in section 3.3. As we will discuss in the next section, a very satisfactory description of the spectra can be achieved. The level energies used to calculate the detuning Δ in equation 3.11 can be regarded as free of the above mentioned effects. Of course, the analysis invokes the potential of the excited state itself via equations 3.6 and 3.7

and the dependence of the rotational structure on the potential. Consequently, the calculations have to be done iteratively, but require a few iterations only to achieve convergence. A list of the determined level energies is given in table 3.4.2.

Since the leading C_3 coefficient originating from the resonant dipole-dipole interaction in the potential description (see eq. 3.10) is connected to the decay rate γ_{at} of the atomic level $4s4p\,{}^1\mathrm{P}_1$ via the expression

$$\gamma_{\mathrm{at}} = \frac{2\omega^3}{3\hbar c^3} C_3, \tag{3.15}$$

we can give an improved value for γ_{at}. With $C_3/hc = 0.52306(20) \cdot 10^3$ cm^{-1}nm^3, one finds $\gamma_{\mathrm{at}} = 2.1558(8) \cdot 10^8$ s^{-1}. The uncertainty stems mainly from the correlation with the C_6 coefficient, which was set to $C_6/hc = 32.2$ cm^{-1}nm^6 and is varied by a factor of 2 to give the error limit above. The fit quality of the observed photoassociation levels is not altered significantly. The uncertainty from the validity of the asymptotic description plays a minor role, which we verified by replacing the nodal line by an approximated short range potential (see sec. 3.3) and fitting the repulsive potential branch. The relative variation of C_3 was found to be below $5 \cdot 10^{-4}$. The new value for γ_{at} is in agreement with our previous one $(2.150(19) \cdot 10^8$ s^{-1} in reference [Deg03]) and in remarkable agreement with the theory value of $2.156(30) \cdot 10^8$ s^{-1} in reference [Por01], but shows some deviation from recent calculations (ref. [Bus06], $2.169 \cdot 10^8$ s^{-1})."

3.4.3 Scattering length

"Due to the comparatively high temperature in our experiment, the influence of higher partial waves than the s-wave is of importance. At least f-waves contribute considerably to the spectra, as can be seen by the presence of $J = 5$ resonances in the spectra depicted in figure 3.4. The lines show results of simulations using the model described in section 3.3 under the respective experimental conditions for selected different ground state scattering lengths. The scattering length was changed by slight variation of the repulsive branch of the ground state potential. As was mentioned before in section 3.2, the atomic density had to be adjusted by a factor of about 1.5 to match simulations and experiment. The long range potential of X ${}^1\Sigma_g^+$ is given by the parameters reported in [All03].

As can be seen in figure 3.4, the new measurements are well described by the simulations and fit best to a ground state s-wave scattering length in the interval of $340\ a_0$ to $700\ a_0$ ($a_0 \approx 0.052918$ nm is the Bohr radius). The sensitivity of the relative line intensity $J = 1/J = 3$ on the scattering length is due to a strong variation of the relative amplitude of s- and d-wave over the internuclear distance, which is probed at different R_{C} by the vibrational levels in the excited state (see eqs. 3.6 and 3.7). The range of $R_{\mathrm{C}} = 4.4$ nm ... 6.7 nm is around the maximum of the d-wave rotational barrier at about 5.85 nm.

For these measurements, the temporal stability of the setup is of great importance, since changes in the trap lifetime, atomic pair density, or PA laser power change the observed trap loss. Hence, in addition to the recordings in figure 3.4

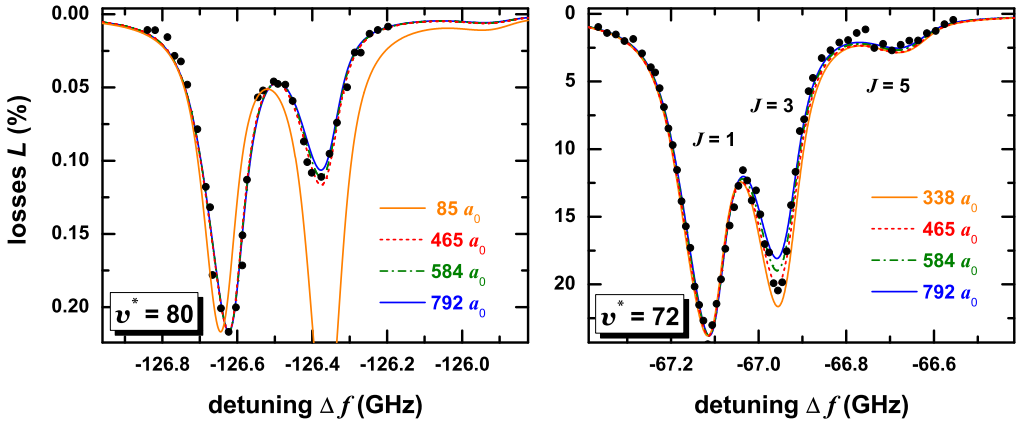

Figure 3.4: *Measured photoassociative spectra of $v^* = 72$ (right hand side) and $v^* = 80$ (left hand side) are depicted by dots. The lines show simulations according to the respective experimental conditions with different ground state s-wave scattering lengths.*

several spectra of the discussed lines were quickly recorded with low frequency resolution to be insensitive to drifts in the setup. These measurements confirm the interval of the scattering length given above. In a previous publication [Deg03] we reported on a determination of the ground state scattering length by similar means but with data up to $v^* = 72$. Then we found a description that favored scattering lengths around $85\ a_0$. We did not notice the ambiguous description of our previous data by the two scattering lengths $85\ a_0$ and $465\ a_0$ due to the lack of data at large detunings and a limited range of investigated scattering lengths. With the new measurements it became apparent that the small scattering length of $85\ a_0$ cannot describe the whole data set as can be seen in figure 3.4. Therefore, a scattering length of $85\ a_0$ has to be ruled out now. The new analysis is also in much better agreement with data from classical spectroscopy [All03], which gives a value between $200\ a_0$ and $800\ a_0$. Obviously, the old photoassociation data should be describable with the new potential parameters to give a consistent picture. We have checked this and as example a scan of $v^* = 72$ from 2003 is given together with a new and old ($85\ a_0$ scattering length) simulation in figure 3.5. The description is quite satisfactory."

3.5 Conclusion

"We described new photoassociation experiments at the asymptote $4s^2\,{}^1\mathrm{S}_0 + 4s4p\,{}^1\mathrm{P}_1$ of ^{40}Ca. A considerably extended energy interval was covered, which is related to an enlarged range of Condon points in internuclear separation. Therefore, we deduced more accurately the ground state scattering length from our new photoassociation

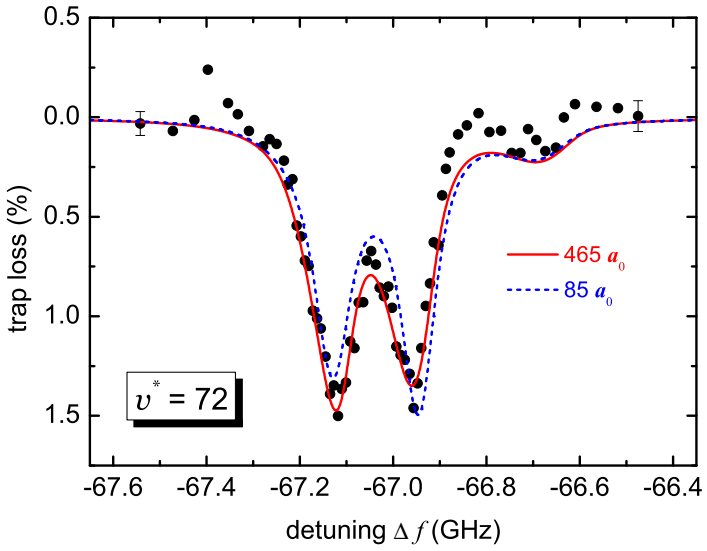

Figure 3.5: *Photoassociation data of $v^* = 72$ from 2003 (dots) [Deg03] together with a simulation according to the model described here (full line) and a s-wave ground state scattering length of $465\ a_0$. The dashed line is a simulation using a scattering length of $85\ a_0$. Experimental details are given in [Deg03].*

data.

The observations are quantitatively very well described by a model that uses the molecular potentials and experimental conditions to predict the photoassociation spectra. By comparison of simulation and experiment we are able to give an interval for the ground state s-wave scattering length of $340\ a_0$ to $700\ a_0$. This is in good agreement with values from classical spectroscopy [All03] and resolves the discrepancy to previous PA experiments [Deg03].

With the new data, we are also able to give an improved value of the long range dipole-dipole coupling constant C_3 of the excited state B $^1\Sigma_u^+$, from which we deduce the decay rate $\gamma_{\mathrm{at}} = 2.1558(8) \cdot 10^8\ \mathrm{s}^{-1}$ for the $4s4p\ ^1\mathrm{P}_1$ state of ^{40}Ca."

The scattering length and therefore the cross section of ^{40}Ca seems to be sufficient large in comparison to elements, which could be Bose-Einstein condensed by evaporative cooling in an optical dipole trap. ^{174}Yb has a similar electronic structure like earth alkaline elements and a smaller scattering length of $19a_0 \leq a \leq 57a_0$ [Tak04]. Also ^{87}Rb [Bar01], which was the first element with which a BEC in a dipole trap could be created, has a smaller scattering length of about $100\ a_0$. Therefore evaporative cooling in an optical dipole trap also seems to be a promising way to reach quantum-degeneracy in ^{40}Ca.

Consequently the following chapter 4 investigates optimum conditions for an optical dipole trap for ^{40}Ca and identifies possible loss processes, which limit the phase-space density in the dipole trap.

Chapter 4

Optical dipole traps for calcium and their properties

After the preparation of the calcium ensemble in the two-stage MOT (see chapter 2) an optical dipole trap is necessary to further increase the phase-space density. The conditions for an efficient transfer of atoms from the MOT to an optical dipole trap are subject of this chapter. A description of the trapping potential will be followed by an investigation, how laser cooling inside the dipole trap can be assured and therefore an efficient transfer of atoms to the dipole trap can be achieved. This investigation leads to a model, which allows the choice of a suitable dipole trap for calcium. The experimental setup of this dipole trap is described afterwards. Subsequently the loading dynamics and the processes, which limit the maximum achievable number of atoms in the trap are investigated.

4.1 Theoretical description of the trapping potential

The storage and trapping of neutral atoms in optical dipole traps relies on the electric dipole interaction with light, far-detuned from any atomic resonances. The electrical field $\vec{E}(\vec{r},t)$ of the laser beam polarizes the neutral atom and therefore induces an atomic dipole moment $\vec{P}(\vec{r},t)$, which oscillates with the frequency ω of the driving field. The interaction of the induced dipole moment $\vec{P}(\vec{r},t)$ and the driving field $\vec{E}(\vec{r},t)$ is described by the potential $U(\vec{r}) = -\frac{1}{2}\langle\vec{P}(\vec{r},t)\cdot\vec{E}(\vec{r},t)\rangle$, where the brackets denote the time average over the fast oscillations of the electric field. For the Zeeman component m_i of a considered atomic state i, the potential is given by the ac-Stark shift $U_i(\omega,p,m_i,\vec{r})$ and depends on frequency ω and polarization p of the electric field amplitude $\vec{E}(\vec{r})$. The dipole potential U_i of the state i can be expressed by the atomic polarizability α and intensity $I(\vec{r}) = \epsilon_0 c\vec{E}(\vec{r})^2$

$$U_i(\omega,p,m_i,\vec{r}) = \frac{-\alpha_i(\omega,p,m_i)}{2\epsilon_0 c} I(\vec{r}). \tag{4.1}$$

By using second-order perturbation theory it is possible to calculate the polarizabil-

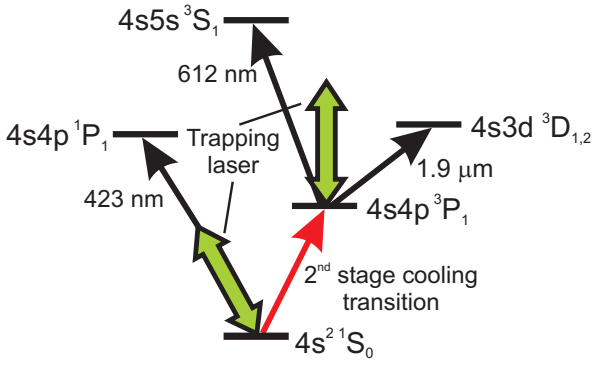

Figure 4.1: *The most important couplings of the $^1S_0$ and $^3P_1$ state, which contribute to their ac-Stark shifts.*

ity α_i [Deg04b]

$$\alpha_i(\omega, p, m_i) = 6\pi\epsilon_0 c^3 \sum_{k,m_k} \frac{A_{ki}(2J_k+1)}{\omega_{ik}^2(\omega_{ik}^2-\omega^2)} \begin{pmatrix} J_k & 1 & J_i \\ -m_k & p & m_i \end{pmatrix}^2. \tag{4.2}$$

The sum runs over all states k, which couple to the state of interest i by transitions with Einstein coefficients A_{ki} and frequencies ω_{ik}. Zeeman components m_i, m_k and total angular momenta J_i, J_k of the states i and k as well as the polarization p of the electric field are represented in the $3J$-symbol. From the intensity distribution $I(\vec{r})$ of a Gaussian laser beam with the optical power P propagating in z-direction[1]

$$I(r,z) = \frac{2P}{\pi w^2(z)} \exp\left(-2\frac{r^2}{w^2(z)}\right), w(z) = w_0\sqrt{1+\frac{z^2}{z_\mathrm{R}^2}}, \tag{4.3}$$

follows the radial and axial shape of the potential. Here $w(z)$ denotes the radius, where the intensity of the laser beam decreases to $1/e^2$ and $z_\mathrm{R} = \pi w_0^2/\lambda$ is the Rayleigh length.
Close to its minimum the dipole potential can be approximated by a harmonic potential

$$U(r,z) \simeq -|U_0|\left[1-2\left(\frac{r}{w_0}\right)^2-\left(\frac{z}{z_\mathrm{R}}\right)^2\right], \tag{4.4}$$

where $|U_0| = |U(r=0, z=0)|$ denotes the potential depth. In the harmonic trap the corresponding frequencies for the radial ω_r and axial motion ω_z of an atom with mass m are given by

$$\omega_r = \sqrt{\frac{4|U_0|}{mw_0^2}}, \ \omega_z = \sqrt{\frac{2|U_0|}{mz_\mathrm{R}^2}}. \tag{4.5}$$

[1]Differing from chapter 2, the z-axis defines in this chapter the direction of beam propagation and not the vertical axis.

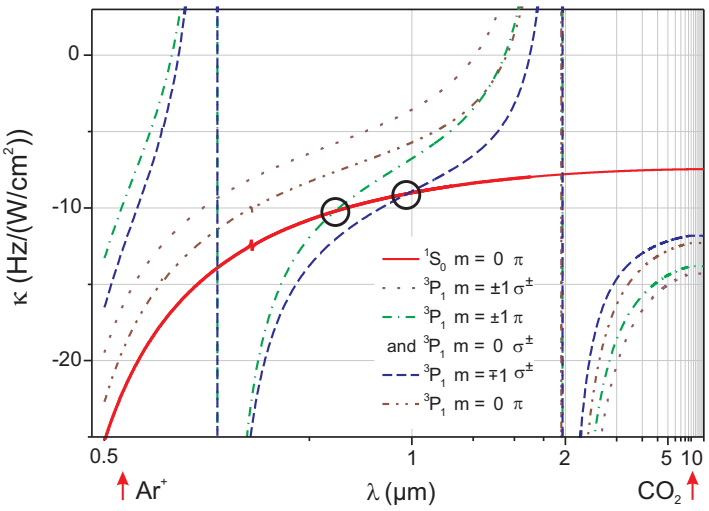

Figure 4.2: *Normalized light shifts κ for the ground state $^1S_0$ and for the excited state $^3P_1$ with its Zeeman sublevels m and different polarizations π or $\sigma^{\pm}$ of the dipole trapping laser as a function of its wavelength. At two wavelengths one can observe an equal shift of the $^1S_0$ state and of one component of the $^3P_1$ state. These are the magic wavelengths indicated by a circle. The vertical lines are due to poles in the polarizability from the transition $4s4p\ ^3P_1$ - $4s4d\ ^3D_{1,2}$ at 1.9 μm and $4s4p\ ^3P_1$ - $4s5s\ ^3S_1$ at 612 nm.*

As soon as the cooling process in the second stage of the MOT is finished, a transfer of the atoms into an optical dipole trap is necessary, to further increase the phase-space density. A far-detuned dipole trap can be regarded as a conservative trap, since a dissipation mechanism is not present in the trap. To efficiently transfer atoms into the dipole trap it is necessary that the trap is compatible with the dissipative cooling force of the MOT. In such a trap the number of atoms and the phase-space density will increase with time until loss mechanisms prevail. If one considers the dipole-allowed cooling transition at 423 nm the light field of a trapping laser with $\lambda \gg 423$ nm induces an attractive potential of the ground state $4s4s^1\mathrm{S}_0$ and a repulsive potential of the upper cooling state $4s4p^1\mathrm{P}_1$. For the spin-forbidden transition of the second cooling stage the situation differs. In both states an attractive potential is induced by the trapping laser, since they couple independently to the respective singlet and triplet states (see fig. 4.1). This different behavior is due to the small dipole moment of intercombination transitions in comparison to that of the allowed transition.

Figure 4.2 shows the normalized shifts $\kappa(\lambda) = -\alpha(\lambda)/(2\epsilon_0 ch)$ of the ground state $4s^2\ ^1\mathrm{S}_0$ and the excited state $4s4p\ ^3\mathrm{P}_1$ as function of the laser wavelength λ for different polarizations. At two wavelengths the ac-Stark shift of the ground state is equal to the shift of one of the Zeeman sublevels of the excited state. One zero-crossing for the $m_\mathrm{S} = 0$ - $m_\mathrm{P} = 0$ transition is realized at a trapping laser wavelength of 800.8 nm [Deg04b] for π-polarized radiation. At the same wavelength this can be observed for the $m_\mathrm{S} = 0$ - $m_\mathrm{P} = 0$ transition with $\sigma^{\pm}$-polarized light. At a laser wavelength of 983 nm [Deg04b] a second zero-crossing for the $m_\mathrm{S} = 0$ - $m_\mathrm{P} = \mp 1$

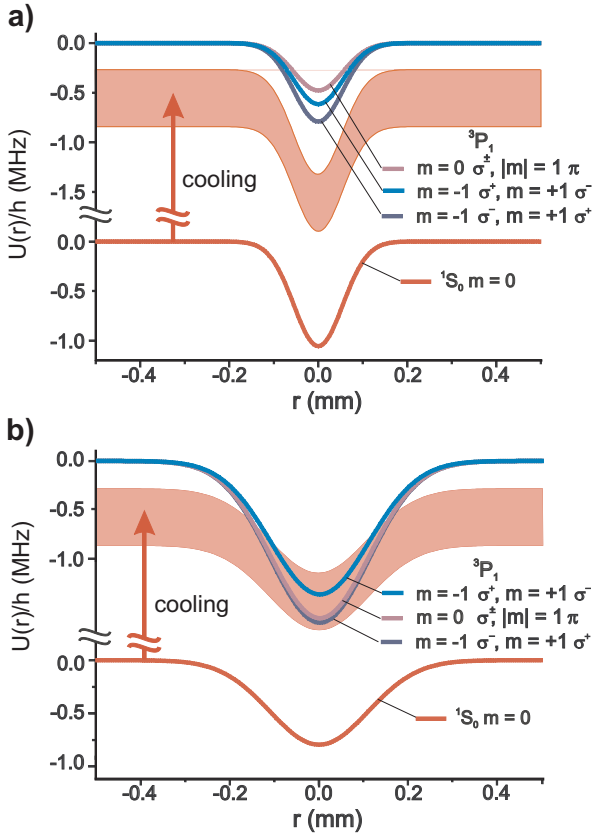

Figure 4.3: *The dipole potential of the ground and the excited states as a function of the distance r from the center of the trapping laser beam. In case a) at a wavelength of 514 nm (Ar^+ laser) the $^1S_0$ state has a bigger shift in comparison to the different states of $^3P_1$. In case b) the opposite situation is considered, realized by a dipole trap at a wavelength of 10.6 μm (CO_2 laser). The experimental parameters of case a) are an optical power of 8 W and a beam waist of 110 μm. In case b) a power of 80 W is focused to a beam waist of 220 μm. The band indicates the broadened spectrum of the cooling laser.*

transition occurs for $\sigma^{\pm}$-polarized light of the trapping laser. An operation of the dipole trap at these so-called "magic wavelengths" allows to manipulate the trapped atoms as if they were in free space [Kat99a].

The question arises at which of these two magic wavelengths the dipole trapping laser should operate in order to have the best possible transfer of atoms from the MOT to the dipole trap. This becomes clear if two limiting cases are considered. In the first case the light shifts of all Zeeman components of the excited state are smaller than the shift of the ground state. This situation was realized in a dipole trap, which operates at the wavelength of an Ar^+ laser at 514 nm (compare [Deg04a], [Gra07]). Figure 4.3 a) shows the radial dependence of the dipole potential for ground and excited state in the center of the trap. Also depicted is the spectrum of the cooling laser, which is red-detuned below the atomic resonance. Inside the dipole trap the cooling spectrum is red-detuned with respect to the $^3P_1$ states for all polarizations of the trapping laser. Thus the velocity dependent cooling forces are also present

in the dipole trap. In the center of the trap the detuning is up to 400 kHz increased in comparison to the outside, if the relevant trap parameters are taken into account. Therefore the scattering of cooling photons is decreased and an efficient cooling is only expected at the edges of the dipole trap. In the second case the opposite situation is considered: the light shift of the ground state is smaller than the shifts of the excited states. Experimentally this case was observed in a dipole trap, which operates at a wavelength of 10.6 μm, realized by a CO_2 laser [Gra07]. Hereby the spectrum of the cooling laser is no longer red-detuned inside the dipole trap, as can be seen in figure 4.3 b). Atoms which arrive at the dipole trap as well as atoms at rest will be directly excited, since velocity dependent cooling forces are not present inside the trap. In the center of the trap the increased resonant scattering on the narrow line and on the quench transition leads to heating and no atoms can be stored.

4.2 An optical dipole trap suitable for calcium

From previous investigations the best transfer of atoms from the MOT to the dipole trap is expected, if the dipole trap is realized at the magic wavelength of (983 ± 12) nm. At this wavelength one Zeeman component of the cooling transition is not shifted, if the dipole trap is operated with circular polarized light. For the other Zeeman components the cooling laser becomes further red-detuned and an additional heating should not appear. Close to this magic wavelength a Yb:YAG (ytterbium doped yttrium aluminum garnet) disc laser was available for the realization of the dipole trap, which provides at high optical power a good beam quality.

4.2.1 Experimental setup and measurement sequence

The dipole trap is realized by a Yb:YAG single-frequency disc laser, which has an output wavelength of 1030 nm. It is a prototype laser developed and built by the Institut für Strahlwerkzeuge at the university of Stuttgart. The Yb:YAG crystal disc is pumped by a diode laser, which provides up to 100 W optical power at a wavelength of 940 nm, resulting in an output power of 25 W at 1030 nm. Due to its special design, the laser provides at this high power a high beam quality. Different from usual solid state lasers the crystal is made of a 200 μm thin disc, whose backside is placed on a heat sink [Gie94]. This geometry avoids the spurious formation of thermal lenses at intensive optical excitation. The crystal is pumped from its front. The backside of the disc has a high reflecting coating for the pumping and the laser wavelength. Therefore the crystal disc also serves as a mirror of the resonator. As it is shown in figure 4.4 the resonator is z-shaped and contains an etalon and a Lyot filter to select different wavelengths than 1030 nm. In the present work a tuning closer to the magic wavelength around 980 nm was not carried out, since the emission cross section of Yb:YAG at these wavelengths is one order of magnitude smaller than around 1030 nm [Trä07]. The observed power instability at an output between 18 W and 25 W is smaller than $\pm 2\%$ after the warm-up of the system (≈ 1

hour).

The setup (see fig. 4.4) for the optical dipole trap consists of two similar optical paths, used for a trap in the horizontal plane ("horizontal trap") and for a 20° tilted trap ("tilted trap") with respect to the horizontal plane. Both optical paths, separated by a polarizing beam splitter, include an AOM[1] to switch the light of the dipole trap and to control the optical power. The AOMs have a large aperture of ≈ 2 mm to allow the switching of beams with a respective large diameter and to avoid therefore the damage of the AOM crystals at high optical powers. The different AOM driving frequencies result in a 30 MHz relative frequency shift between both beams, which avoid the interference if the beams are overlapped in the crossed-beam optical dipole trap (see chapter 5). In the case of the tilted trap the light of the first order is coupled into a fiber by two achromats (tilted trap) or by two high-power resistant lens systems (horizontal trap), respectively (company: Linos). The fibers are mounted in a five axis fiber aligner system manufactured by New Focus (model 9091), which provides a good mechanical stability. The fibers which carry the light to the experiment have a large mode field diameter (MFD) between 15 μm and 20 μm and allow therefore to guide high laser powers. They use a photonic crystal structure and provide single-mode operation in a wavelength range between $0.6-1.0$ μm (company: Crystal Fibres). The fiber for the tilted trap (type: LMA-PZ-800, MFD 20 μm) is polarization maintaining around a wavelength of 1 μm. This fiber type was not available for the earlier installed horizontal trap (type: LMA 20, MFD 15 μm). Additionally a test beam of resonant 657 nm radiation can be coupled into one fiber, to inspect the overlap of the horizontal dipole trap with the MOT. On the side of the experiment a similar setup for the creation of both traps is realized. The light coming from the fiber is collimated and subsequently focused to a beam waist of ≈ 33 μm. The collimation lens (focal length $f = 100$ mm) as well as the focusing lens (focal length $f = 300$ mm) are best form lenses (company: B. Halle). The focusing lens is mounted on a three-axis translation stage, which allows to move the focus in each direction by ± 8 mm. The beam waist was measured by observing it with a CCD-camera. A change of the waist size could be not observed if the lens was moved by ± 3.0 mm perpendicular to the axis of beam propagation. Between both lenses the polarization optics are placed to generate circularly polarized light. Two photo detectors collect the stray light from beam traps and allow to monitor the optical power.

The measurements of this chapter are carried out in the horizontal trap with a time sequence illustrated in figure 4.5. After the usual preparation in the first stage of the MOT the loading of the dipole trap starts as soon as the second stage of the MOT is switched on and the temperature of the ensemble is low enough. Thereby the focus of the dipole trap laser beam is in or close to the center of the MOT. When the MOT is switched off the loading stops and untrapped atoms fall down under the influence of gravity. The duration of the simultaneous operation of dipole trap and MOT is denoted as loading time. After the loading period the dipole trap operates for another 100 ms in order to separate trapped from untrapped atoms. After this

[1]The AOMs are manufactured by Crystal Technology, type 3110-191 (tilted trap) and A.A, type AA MTS 80/A3 (horizontal trap).

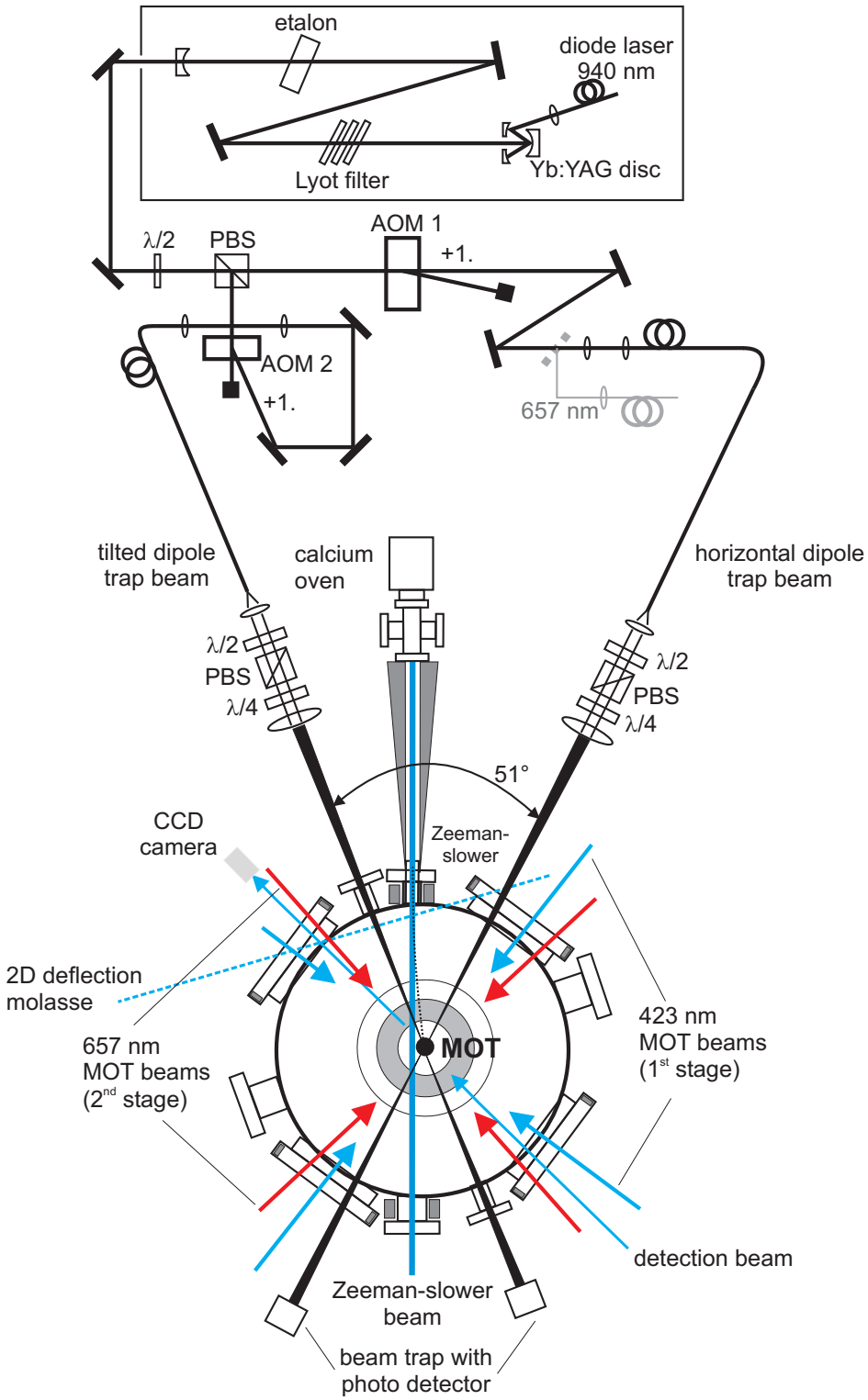

Figure 4.4: *Top view of the experimental setup with the beams of the horizontal and tilted dipole trap. This beam is tilted by 20° with respect to the horizontal plane, which corresponds with the drawing plane. An explanation of the different parts is given in the text as well as in Figure 2.2. AOM: acousto-optical modulator, PBS: polarizing beam splitter, $\lambda/2$, $\lambda/4$: retardation plates.*

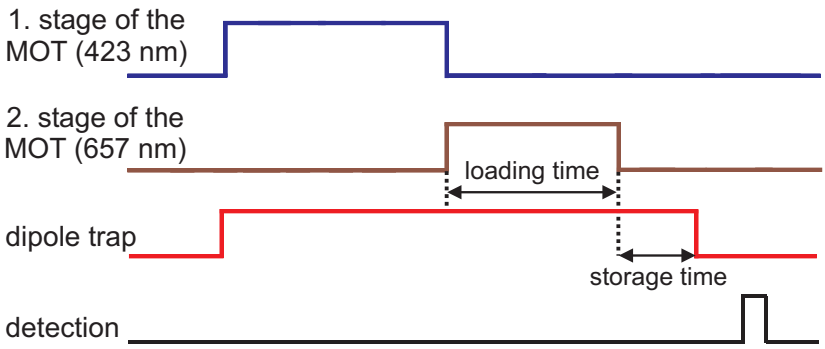

Figure 4.5: *Time sequence for the measurements with the dipole trap. The focus of the dipole trap laser beam is superimposed on the MOT in space and time. After the usual preparation in the 423 nm MOT the loading into the dipole trap becomes significant as soon as the temperature of the ensemble in the 657 nm MOT is low enough. When the loading of the trap is finished and the 657 nm MOT is switched off, the atoms are stored for variable times. The detection of the atoms is performed by taking absorption images or by measuring the fluorescence light.*

time all untrapped atoms fall down under the influence of gravity and have left the detection region. The period in which only the dipole trap operates is called storage time. After the storage time the atoms are released from the dipole trap and the cloud expands for 1 ms - 2 ms before it is detected. For detection either an absorption image is taken or the blue fluorescence is measured after the atoms were excited by 423 nm MOT light. At shorter expansion times the atomic ensemble is still too dense and the real number of atoms in the dipole trap would be underestimated in the detection step.

4.2.2 Loading rate of the dipole trap

At the beginning of the loading phase, the number of atoms increases as $N_{\mathrm{Dip}}(t) = r_0 \cdot N_{\mathrm{MOT}} \cdot t$, where r_0 is the loading rate and N_{MOT} is the number of atoms in the MOT, which is assumed to be constant. Figure 4.6 shows the initial loading behavior for an identical trap depth of 140 μK but different polarized light of the trapping beam. These trap depths are realized by an optical power of $P = 5.5$ W at a beam waist of $w_0 = 33$ μm. The linear fits to the loading data are used to derive a first approximation of the loading rates r_0. In the following the obtained values will be verified by a model, which include the loss mechanisms. The experimentally observed loading rates r_0 can be interpreted by the time $1/r_0$ in which on average one atom in the MOT achieves the region of the dipole trap and gets trapped. The influence of the dipole trap potential becomes significant in comparison to the temperature of the MOT atoms at a radius r_{eff} at which $U(r_{\mathrm{eff}}) = -k_{\mathrm{B}}T$. The radius is given by

$$r_{\mathrm{eff}} = w_0 \cdot \sqrt{\frac{\ln(\eta)}{2}}, \tag{4.6}$$

with $\eta = |U_0/k_{\mathrm{B}}T|$. The effective trapping volume of the dipole trap is approximated by a cylinder of the radius r_{eff} and the length of the MOT $V_{\mathrm{eff}} = \pi r_{\mathrm{eff}}^2 \sqrt{2\pi}\sigma$. At a tem-

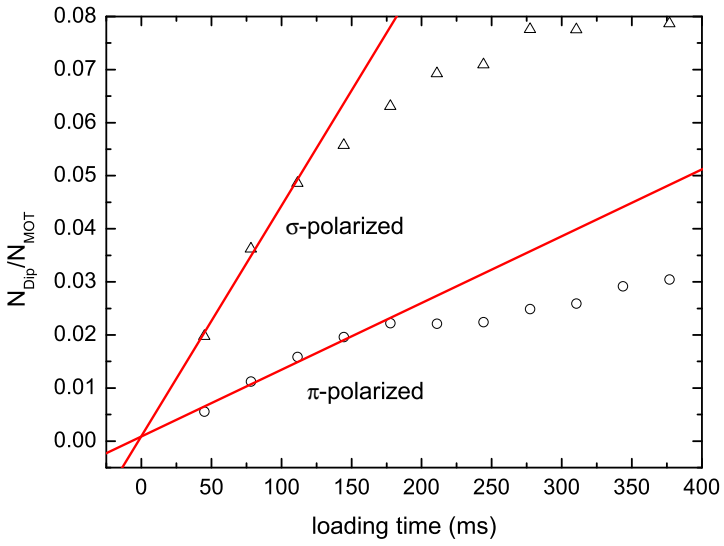

Figure 4.6: *Initial loading behavior in a dipole trap realized with linear (π) and circular (σ) polarized light. The number of atoms increases linearly in time until loss processes prevail over the loading rate and limit the maximum number.*

perature of $12\ \mu$K (rms velocity $v_{\mathrm{rms}} = 9$ cm/s) an MOT atom needs approximately 10 ms to cross the MOT. Since the MOT volume $V_{\mathrm{MOT}} = \sqrt{2\pi}^3\sigma^3$ is about 300 times larger than the volume V_{eff} of the dipole trap, only every $V_{\mathrm{MOT}}/V_{\mathrm{eff}} \cdot 10$ ms≈ 3.3 s an atom reaches the region of the dipole trap. During the transit time through the dipole trap the kinetic energy of the atom must be removed by the light of the second cooling stage. If the experimental parameters (waist w_0, optical power P) of the dipole trap with circular polarized light are considered, the frequency shift between the ground state and the Zeeman component $m = \mp 1$ of the excited state amounts to approximately 100 kHz in the center of the dipole trap. Inside the dipole trap the high frequency edge of the 657 nm cooling spectrum is therefore up to 100 kHz additionally red-detuned in comparison to the ideal cooling conditions in free space (see section 2.3). This only results in a marginal degradation concerning final temperature and density, if the situation in the MOT is considered (section 2.3). The approximated loading rate $r_0 = 0.3\ \mathrm{s}^{-1}$ shows therefore a good agreement with the measured rate $r_0 = (0.43 \pm 0.04)\ \mathrm{s}^{-1}$ for σ-polarized light. The deviation is probably due to the very simple interpretation of r_0. For π-polarized trapping light the expected frequency shift in the trap center is 800 kHz and an effective cooling is therefore only possible at the edge of the trapping volume. This qualitatively explains the lower loading rate of $r_0 = (0.13 \pm 0.01)\ \mathrm{s}^{-1}$.

4.2.3 Loss processes in the dipole trap

For longer loading times the number of transferred atoms reaches a maximum and then decreases. This is caused by loss processes in the dipole trap as well as in the MOT, which counteract the loading. The loss processes in the dipole trap are investigated in this section. For this purpose the number of atoms in the dipole trap is measured as a function of the storage time. As soon as the maximum in the number of atoms is reached, the MOT is switched off and the decay of the number of atoms is observed after a delay of 100 ms (see fig. 4.5).

To isolate the influence of the different experimental parameters, the measurement was carried out on the one hand with the 657 nm MOT light and on the other hand with the 453 nm quench light in addition. In both cases the quadrupole field of the MOT was switched off. These measurements were compared with the decay curve in the absence of MOT light. The decay of atoms from the trap is obviously not exponential (see fig. 4.7). For shorter storage times and therefore at higher densities in the trap one observes in all measurement configurations a faster decay of atoms. If the light of the second stage of the MOT is kept on during the measurement, this faster decay in the beginning is significantly higher than without MOT light. The additional irradiated quench light does not influence the decay. This obviously shows, that the increased scattering of cooling photons and therefore their increased reabsorption does not additionally limit the density. In the absence of MOT light the primarily fast decay can be attributed to the loss of the hottest atoms during the first 1 s (see fig. 4.7 b)). The non exponential decay is due to two-body collisions. The observed decay curve can be described by the following differential equation

$$\dot{N}_{\text{Dip}}(t) = -\gamma_{\text{Dip}} N_{\text{Dip}}(t) - \beta \int d^3r \rho^2(\vec{r},t) = -\gamma_{\text{Dip}} N_{\text{Dip}}(t) - \frac{\beta}{\sqrt{8} V_{\text{Dip}}} N^2_{\text{Dip}}(t), \qquad (4.7)$$

with the collisional loss coefficient β, the loss rate γ_{Dip} and the volume of the dipole trap V_{Dip}. For the dipole trap a three dimensional harmonic potential is assumed. The effective volume of the dipole trap is given by $V_{\text{Dip}} = \sqrt{2\pi}^3 \sigma_r^2 \sigma_z$ with σ_r and σ_z as radial and axial rms-radius of the cloud. In thermal equilibrium the resulting density distribution $\rho(\vec{r})$ is Gaussian in all directions. The cloud radii are related to the trap frequencies by $\sigma_i = \sqrt{k_{\text{B}} T/(m\omega_i^2)}$, with $i = r, z$. In the axis of beam propagation the calculated rms-radius is in good agreement with the value derived from the absorption images: e.g. at a temperature of 16 μK the calculated value amounts $\sigma_z = 790$ μm and the measured is $\sigma_z = (840 \pm 90)$ μm. In the radial direction $\sigma_r = 5.8$ μm a comparison with the absorption image was not possible, since the resolution of the imaging system was insufficient (see 2.2). Therefore the calculated radial frequency is used to calculate the ensemble densities, volumes and phase-space densities.

The solution of the differential equation 4.7 is

$$\frac{N_{\text{Dip}}(t)}{N_{\text{Dip}}(0)} = \exp(-\gamma_{\text{Dip}} t) \left[1 + \frac{N_{\text{Dip}}(0) \beta (1 - \exp(-\gamma_{\text{Dip}} t))}{\sqrt{8} \gamma_{\text{Dip}} V_{\text{Dip}}} \right]^{-1}. \qquad (4.8)$$

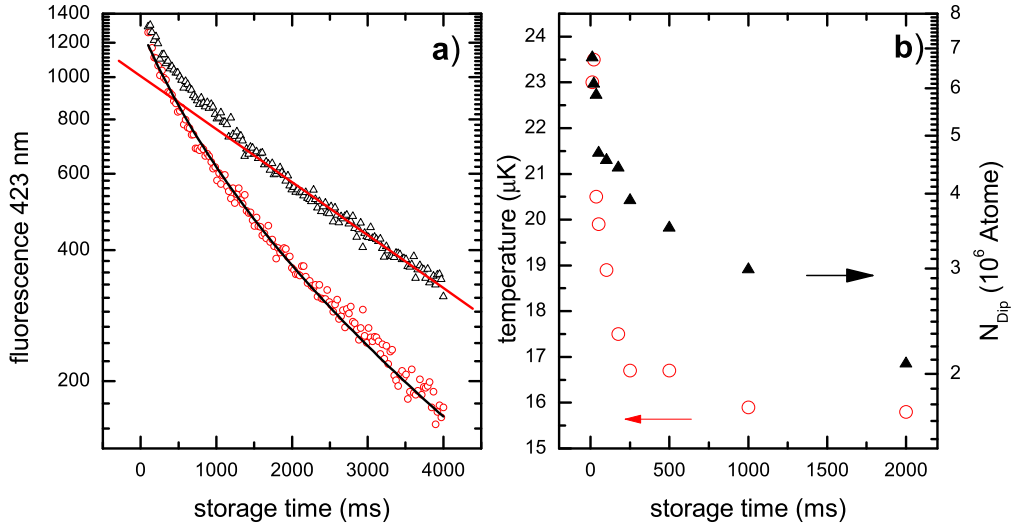

Figure 4.7: *a): Decay of atoms from the dipole trap as a function of storage time, without any MOT light (black triangles) and with the MOT light on (red circles). No influence on the decay is observed, if the quench light is irradiated in addition to the MOT light. The black solid line is a fit according to equation 4.8. The red solid curve describes the exponential decay* $(1/\gamma_{Dip} = (3.6 \pm 0.1)$ *s) after the hottest atoms are escaped from the trap, which is shown in b): The temperature (red circles) decreases during* ≈ 1 *s until a value around* 16 μ*K is reached. The corresponding number of particles are denoted by the black triangles.*

Here $N_{\mathrm{Dip}}(0)$ indicates the number of initially trapped atoms. The solution was used as a fit function for the decay curve with MOT light in order to evaluate the value of β. From the decay curve without MOT light the loss rate due to background collisions was determined to $1/\gamma_{\mathrm{Dip}} = (3.6 \pm 0.1)$ s (see fig. 4.7 a)). By keeping γ_{Dip} fixed to this value, the light induced loss rate β was determined. From the fluorescence curve (see fig. 4.7 a)) a rate coefficient of $\hat{\beta} = (1.44 \pm 0.04) \cdot 10^{-3}$/s could be derived, which depends on the trap volume. The relation between $\hat{\beta}$ and the density related, volume independent rate coefficient β is given by[1] $\beta = y_0\hat{\beta}/\rho_0$, with the initial fluorescence signal y_0 and the initial peak density ρ_0. To consider the initial temperature evolution of the ensemble (see fig. 4.7 b)), the loss coefficient β is derived from $\hat{\beta}$ at a storage time of $t_0 = 100$ ms (19 μK) and at $t_1 = 1$ s (16 μK). The range of the two-body loss coefficient is then given by $1.8 \cdot 10^{-13}$ cm^3/s $\leq \beta \leq 2.6 \cdot 10^{-13}$ cm^3/s.

[1]The temporal development of the fluorescence signal $y(t)$ is given by $\dot{y}(t) = -\gamma_{\mathrm{Dip}}y(t) - \frac{\hat{\beta}}{\sqrt{8}}y^2(t)$. Since the fluorescence signal is proportional to the number of atoms in the dipole trap ($y(t) = y_0 N_{\mathrm{Dip}}(t)/N_{\mathrm{Dip}}(0)$), this differential equation can be converted into the corresponding equation for the number of atoms: $\dot{N}(t) = -\gamma_{\mathrm{Dip}}N_{\mathrm{Dip}}(t) - \frac{\hat{\beta}y_0}{\sqrt{8}N_{\mathrm{Dip}}(0)}N^2_{\mathrm{Dip}}(t)$. By comparing the relevant coefficient with that one of equation 4.7 follows $\beta = y_0\hat{\beta}/\rho_0$.

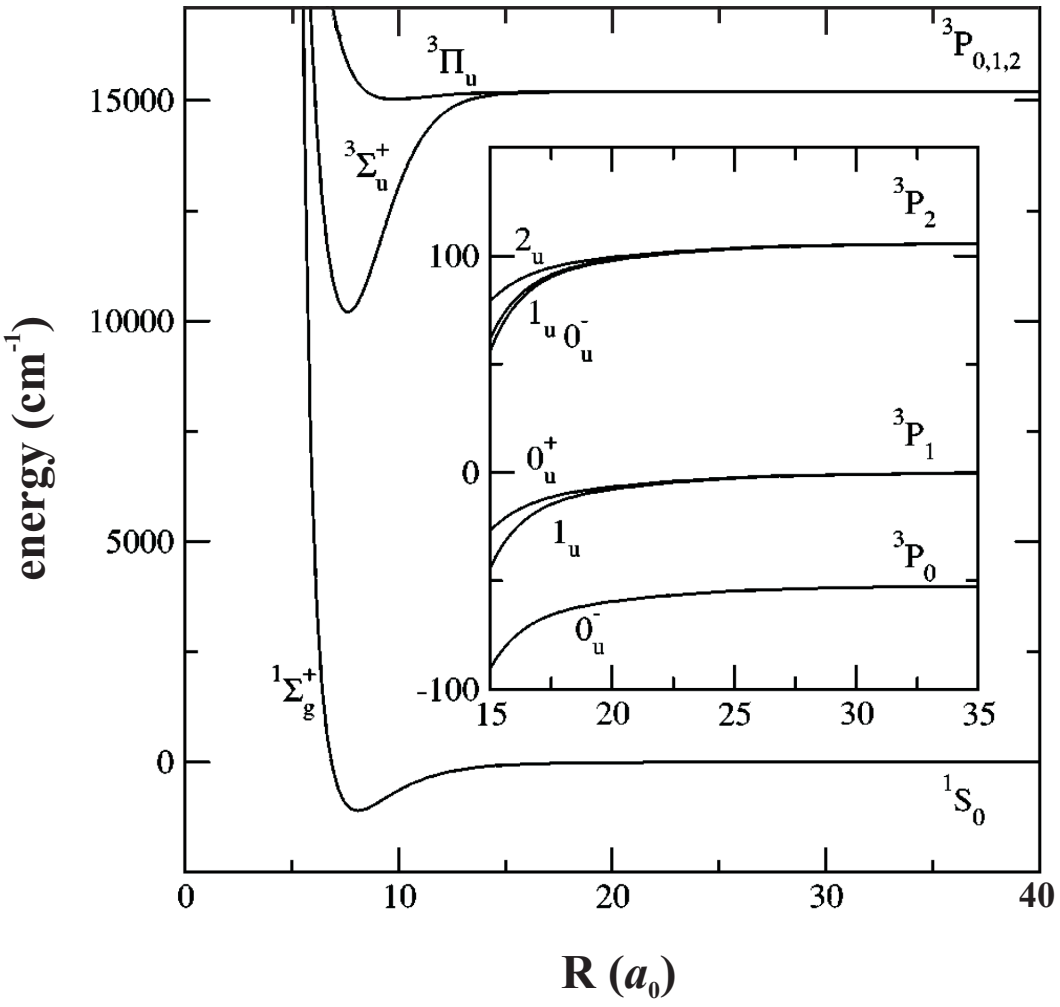

Figure 4.8: *Potentials of two calcium atoms as function of the interatomic distance R. At short range the potentials are labeled by their Hund´s case (a) symmetry. Inset: close to the $^3P+^1S$ asymptote the potentials are described by Hund´s case (c) symmetry. Figure taken from Ciuryło et al. [Ciu04].*

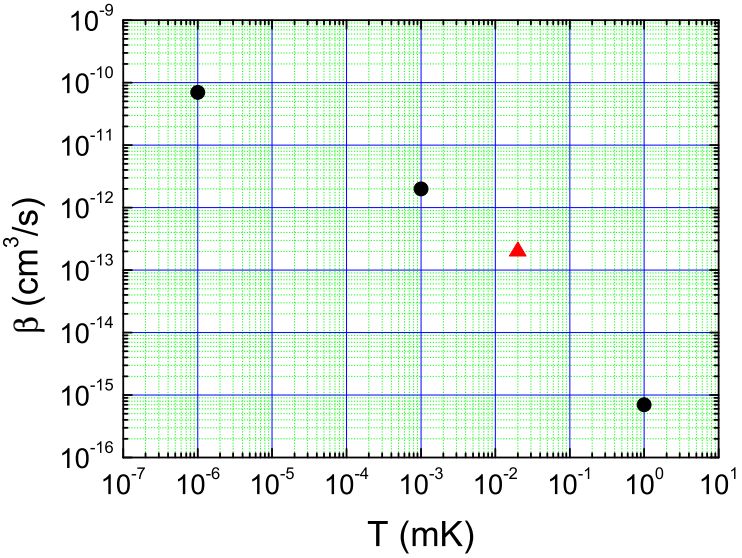

Figure 4.9: *Comparison of the experimentally obtained collisional loss coefficient β (red triangle) with the theoretically predicted values (black circles) for different ensemble temperatures. The predicted loss coefficients [Ciu04] are the peak values of the second vibrational level below the $^3P_1+^1S_0$ limit of the 0_u^+ band (see text).*

A possible explanation for the appearance of the light-induced losses at high ensemble densities is the formation of a bound molecular state by photoassociation of two colliding ground state atoms. The radiative decay of the generated Ca_2 molecule back to the ground state produces a pair of atoms with high kinetic energy, which is no longer trapped. The photoassociation process near the intercombination line was theoretically investigated by Ciuryło *et al.* [Ciu04] for Ca at temperatures between 1 nK and 1 mK. The authors modeled the last five vibrational levels below the $^3P_1+^1S_0$ asymptote for the 0_u^+ and 1_u potentials, which correlate to the $^3\Pi_u$ and $^3\Sigma_u^+$ potentials at short range, respectively (see fig. 4.8). The five vibrational lines of both potentials cover a frequency range of 100 GHz below the $^3P_1+^1S_0$ limit. The absolute position of the vibrational lines with respect to the $^3P_1+^1S_0$ limit can not be predicted due to the insufficient knowledge of the potentials. The peak rate coefficient of the second line below the dissociation limit of the 0_u^+ band was determined for different temperatures at a laser intensity of 1 W/cm^2. At a temperature of 1 μK an on resonant loss rate coefficient of 10^{-12} cm^3/s with a Doppler broadened linewidth of the order of 100 kHz was predicted. The observed collisional rate coefficient is one order of magnitude smaller, which could be the consequence of different effects. The model omits a possible recapture of the hot atoms, which are produced by the PA process and which would result in a reduced loss coefficient. In addition the higher temperature of the ensemble (≈ 20 μK) results in a broader thermal width ($k_B T$) of a PA line and therefore in a smaller rate coefficient. Figure 4.9

illustrates, that the determined loss rate fits well the predicted values between 1 nK and 1 mK. The difference can be due to the fact that a smaller intensity of the PA inducing MOT light was used. In total the cloud was irradiated by an intensity of $0.3\,\mathrm{W/cm^2}$, which was additionally distributed over the broadened spectrum of the cooling laser of 1.5 MHz. Also the broadened spectrum could be in the wings of a PA resonance.

4.2.4 Loading dynamics of the dipole trap

To completely describe the loading dynamics of the dipole trap the loading rate r_0 as well as the loss processes in the dipole trap and in the MOT must be included in a model. The loss of atoms in the MOT can be described by two rates, the loss rate from background collisions γ_{MOT} and the loss rate r_0, which accounts for the transfered atoms into the dipole trap. The loss processes in the dipole trap are given by background collisions γ_{Dip} and by the photoassociative loss rate constant β. This leads to a system of two coupled differential equations

$$\begin{aligned} \dot{N}_{\mathrm{MOT}}(t) &= -\gamma_{\mathrm{MOT}} N_{\mathrm{MOT}}(t) - r_0 N_{\mathrm{MOT}}(t) \\ \dot{N}_{\mathrm{Dip}}(t) &= -\gamma_{\mathrm{Dip}} N_{\mathrm{Dip}}(t) + r_0 N_{\mathrm{MOT}}(t) - \frac{\beta}{\sqrt{8} V_{\mathrm{Dip}}} N^2_{\mathrm{Dip}}(t). \end{aligned} \tag{4.9}$$

The model is compared with loading measurements for a dipole trap realized with linearly and circularly polarized light. This loading behavior is measured by temporary and spatially overlapping the dipole trap to the MOT. Subsequently for 100 ms only the dipole trap operates to remove all atoms that are not trapped. After the dipole trap is switched off the cloud expands for 2 ms before their atoms were excited by 423 nm radiation and the fluorescence signal was detected (see fig. 4.5).

The numerical solution of 4.9 is fitted to the loading curve for σ- and π-polarized light of the dipole trapping laser. Thereby the obtained collisional loss coefficient β from the storage time measurement (see 4.2.3) and the loading rate r_0 are varied. The independently determined lifetimes of dipole trap ($\gamma^{-1}_{\mathrm{Dip}} = (3.6 \pm 0.1)$ s) and MOT ($\gamma^{-1}_{\mathrm{MOT}} = (460 \pm 30)$ ms) are kept constant. The result in figure 4.10 shows a good agreement between model and measurement except of loading times longer than 6 s. At these times obviously the signal-to-noise ratio increasingly degrades and it is therefore hard to tell, if an additional effect, which is not covered by the model, could explain the deviation. The obtained loading rate $r_0 = (0.45 \pm 0.01)\,\mathrm{s^{-1}}$ for σ-polarized light is nearly four times higher in comparison to the dipole trap with π-polarized light ($r_0 = (0.126 \pm 0.006)\,\mathrm{s^{-1}}$), which is a result of the approach to free space cooling conditions inside the trap. Both values confirm the loading rates, which were derived from the initial slope of the loading curves (compare 4.2.2). The collisional loss coefficient amounts to $\beta = (1.95 \pm 0.15) \cdot 10^{-13}\,\mathrm{cm^3 s^{-1}}$ for the dipole trap realized with π-polarized light, which is in the range of the previously estimated β-values ($1.8 \cdot 10^{-13}\,\mathrm{cm^3/s} \leq \beta \leq 2.6 \cdot 10^{-13}\,\mathrm{cm^3/s}$, see 4.2.3). In the case of σ-polarized light, the loss constant $\beta = (2.7 \pm 0.1) \cdot 10^{-13}\,\mathrm{cm^3 s^{-1}}$ slightly exceeds this range. The difference in the two-body loss coefficient for linear and circular polarized light is obviously due to the fact that the 657 nm cooling spectrum within the

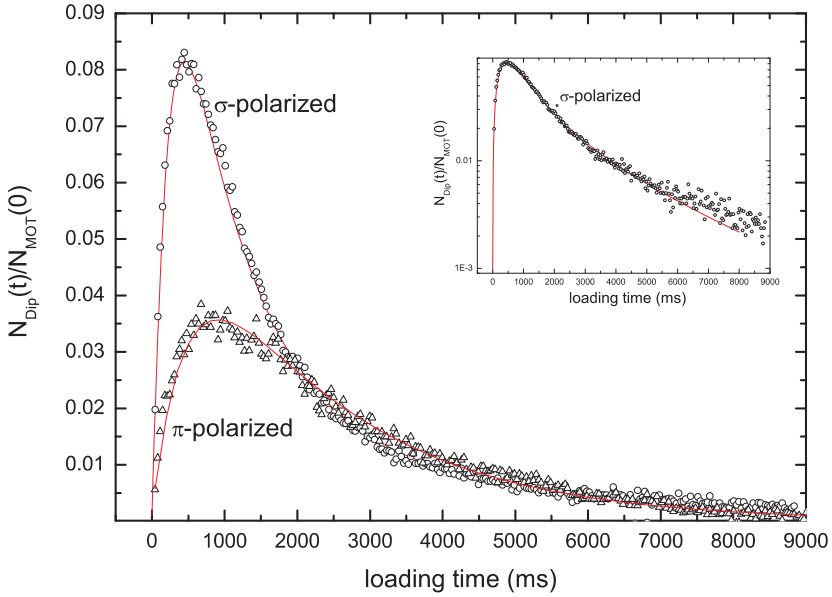

Figure 4.10: *Transfer efficiency from the MOT into the dipole trap as a function of the loading time for a dipole trap realized with linear (π) and circular (σ) polarized light. The solution of equation 4.9 is fitted to the data (red solid line). For σ-polarized trapping light the cooling conditions inside the dipole trap are more like in free space which results in a four times higher loading rate. The maximum of transfered atoms is limited by light assisted collisions (see text). For loading times longer than 6 s the number of remaining atoms is slightly higher than described by the model (see inset).*

center of the dipole trap is shifted differently. As it is pointed out in section 4.2.2, a frequency shift between the ground state and the Zeeman component $m = \mp 1$ of the excited state of about 100 kHz is expected inside the dipole trap with σ-polarized light. In the case of π-polarized light the frequency shift is expected to be approximately 800 kHz. Consequently the spectrum of the 657 nm radiation, which induces the PA process, is different red-detuned to the considered Zeeman component of the excited state and also to possible PA resonances.

The observed photoassociative losses limit the transfer of atoms from the MOT to the dipole trap to $\approx 8\%$. Without these losses, the model (see eq. 4.9) predicts a transfer of $\approx 15\%$. A better transfer of atoms should be expected if the capture radius r_{eff} (see eq. 4.6) is increased by a larger beam waist w_0. The resulting loading rate can be estimated under the assumption of a constant η-value of $\eta = |U_0/k_{\text{B}}| = 11.6$ at the different beam waists, as it was shown in section 4.2.2. Figure 4.11 illustrates the expected loading rates as a function of the waist as well as the necessary optical powers to realize a constant trap depth of $|U_0/k_{\text{B}}| = 140$ μK. As an example a beam waist of 54 μm is considered. The realization of a trap depth of 140 μK requires an optical power of 14.9 W. With the derived loading rate of $r_0 = 0.85$ s^{-1} the expected transfer of atoms to the dipole trap is calculated with the numerical solution of equation 4.9. For this the experimentally observed loss rates $\gamma_{\text{MOT}}^{-1} = 460$ ms, $\gamma_{\text{Dip}}^{-1} = 3.6$ s and $\beta = 2.7 \cdot 10^{-13}$ cm^{3}s^{-1} are considered, which result in a transfer of 18.5 %. In the

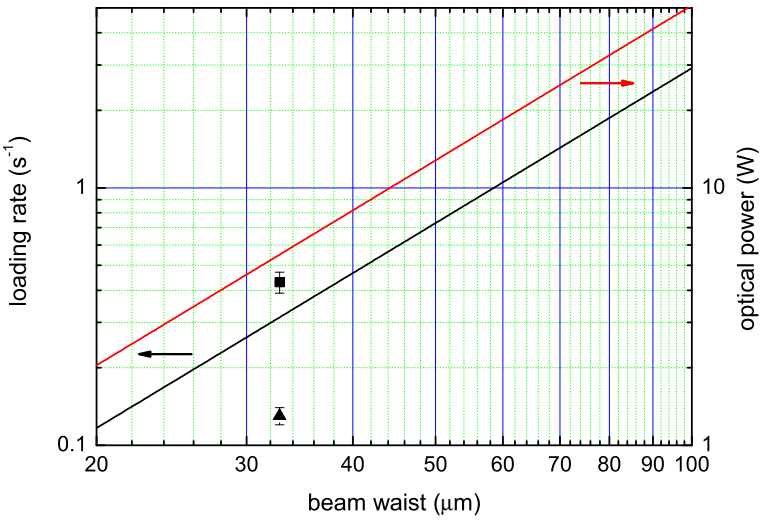

Figure 4.11: *Estimation of the loading rate (black curve) for different beam waists. The necessary optical power to keep the trap depth constant is shown in the red curve. The points are the measured loading rates for a dipole trap with σ-polarized light (black square) and with π-polarized light (black triangle).*

calculation the volume of the dipole trap is used, which is calculated by using the trap frequencies $\omega_r = 1000 \cdot 2\pi$ Hz, $\omega_r = 4.3 \cdot 2\pi$ Hz and an ensemble temperature of $16\ \mu$K.

4.3 Conclusion

This chapter described the realization of an optical dipole trap suitable for calcium atoms and subsequently it investigated the loading dynamics and the loss processes in the dipole trap. From considerations about narrow-line laser cooling in an optical dipole trap followed, that a dipole trap for calcium should operate at a wavelength of (983 ± 12) nm. Here the laser cooling of the second stage of the MOT is compatible with the dipole trap and the highest possible number of atoms should be transfered from the MOT into the dipole trap. Close to this wavelength (1030 nm) an optical dipole trap was realized by a Yb:YAG disc laser, which provides an optical power of 25 W in single-frequency operation. In the dipole trap a density dependent loss process was observed, caused by the light of the second stage of the MOT. These losses could be attributed to the photoassociative creation of calcium dimers, which results in a limitation in the number of atoms transfered from the second stage of the MOT to the dipole trap. The corresponding phase-space density is therefore limited to a value of $2.6 \cdot 10^{-3}$. The loading dynamics of the dipole trap was described by a model, which includes the loading rate and the relevant loss processes. By means of

the model it was predicted, that a two times higher transfer of atoms in the dipole can be expected, if the beam waist is increased to $54\ \mu$m. However this would be accompanied by an decrease of the phase-space density to $1.5 \cdot 10^{-3}$.

A successful way to further increase the phase-space density, which was already practised for ^{174}Yb, is the evaporation in a crossed-beam optical dipole trap [Tak03b]. ^{174}Yb has a similar electronic structure like earth alkaline elements and a scattering length of $19\ a_0 \leq a_s \leq 57\ a_0$ [Tak04]. The ^{40}Ca ground state scattering length and therefore the cross section in comparison to ^{174}Yb is significantly larger so that an efficient evaporative cooling similar to Yb should be applicable. Therefore chapter 5 investigates the loading dynamics and the loss processes in a crossed-beam dipole trap.

Chapter 5

Crossed-beam optical dipole trap

If two focused laser beams are crossed under an angle of about 90° a nearly isotropic dipole trap could be created. The potential in the crossing region, the so-called dimple, realizes a tight confining of the trapped atoms and allows to create high ensemble densities. This assures high elastic collision rates and a fast thermalization. Crossed-beam dipole traps are therefore suited for the application of evaporative cooling. Evaporative cooling in crossed-beam dipole traps allowed to achieve quantum-degeneracy, as it was successfully demonstrated for ^{87}Rb [Bar01], ^{133}Cs [Web03a], ^{52}Cr [Gri05] and for the alkaline earth-like element ^{174}Yb [Tak03b]. The large and positive ground state scattering length of ^{40}Ca (see chapter 3) offers the perspective of the realization of a calcium BEC with a similar experimental scheme. This chapter therefore investigates a crossed-beam dipole trap for ^{40}Ca.

The experiments with BECs in optical dipole traps showed, that it is important to tilt one of the dipole traps with respect to the horizontal plane. The potential of this trap combines the ac-Stark shift potential with the gravitational one and in one direction a lower or vanishing potential barrier is realized, which offers than in the crossed-beam trap an efficient way to evaporate. Furthermore this configuration allows to influence the particle number and phase-space density in the crossing region, since the number of atoms which surround this region can be influenced by the ratio of the optical power in the two beams, which leads to different loading conditions of the dimple.

In the dimple of the crossed-beam dipole trap the phase-space density is locally increased. This effect happened due to an adiabatic modification of the trapping potential: The increase of phase-space density starts as soon as one dipole trap is adiabatically overlapped to the other, resulting in the dimple potential. Atoms which surround the dimple in the single-beam dipole traps serve as a reservoir. Elastically colliding atoms of the reservoir fill the dimple until the local density satisfies the equilibrium condition $\rho(\vec{r}) \propto \exp(U(\vec{r})/k_\mathrm{B}T)$. As a result the local density in the dimple is increased whereas the temperature of the whole system (dimple and reservoir) stays constant, since the reservoir absorbs the excess energy from the elastic collisions in the dimple. It is therefore important, that the potential of the dimple is not deep enough to accumulate all atoms from the reservoir, since otherwise the phase-space density can not be increased. This so-called "dimple trick" was first

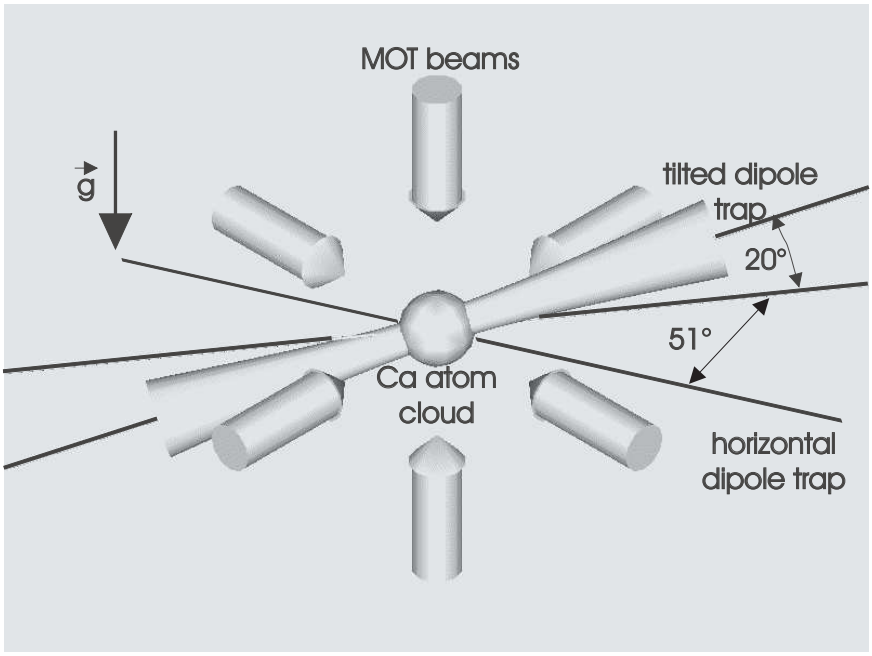

Figure 5.1: *Configuration of the two optical dipole traps and the MOT.*

suggested and experimentally demonstrated by Pinkse *et al.* [Pin97].

This chapter is organized as follows: After a description of the trapping potential follows the investigation, how the power ratio of the two beams influences the number of atoms in the crossing region as well as in the surrounding potential. Furthermore the effect of an adiabatic modification of the potential will be studied by ramping up the intensity of one of the two traps. The following section analyses the loss process in the high dense calcium ensemble in the dimple trap. Finally a model will be introduced, which describes the loading dynamics of the dimple.

5.1 Characterization of the crossed-beam dipole trap

As it is shown in the following, the gravitation not only influences the trapping potential of the tilted trap but also the potential of the crossed-beam trap. Therefore the following section first analyses the influence of gravity on the tilted trap and then the potential shape of the crossed-beam trap will be discussed. The ratio of the power in the two beams affects the number of atoms in the dimple. This is investigated in detail, followed by an experiment in which the dimple potential was switched on adiabatically.

5.1.1 Optical dipole potential - influence of gravity

The potential of the crossed-beam dipole trap is the sum of the potential of the horizontal and the tilted trap. In the previous chapter the considerations of the hor-

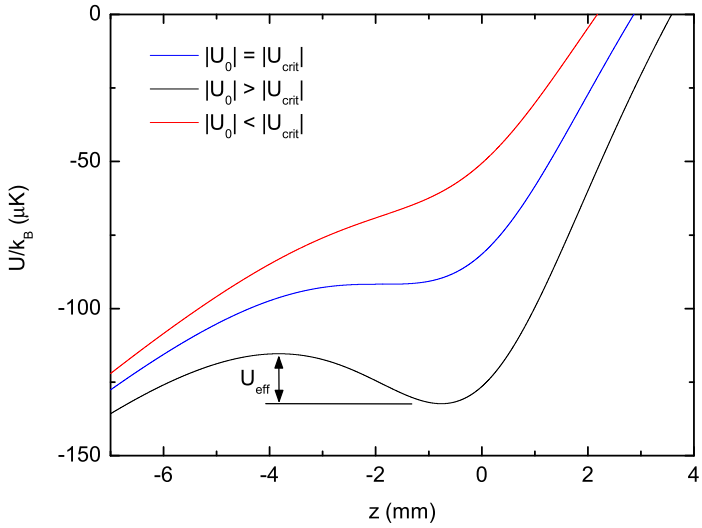

Figure 5.2: *Potential in the tilted dipole trap for different optical powers. Only if the dipole potential $|U_0|$ exceeds the critical value $|U_{crit}|$ a local minimum in the potential appears and it becomes possible to trap atoms. The realized dipole trap has an effective depth of U_{eff}.*

izontal trap neglected the influence of gravity. At the used optical powers of the trapping beam this was justified, since the dipole force was significantly smaller than the gravitational one, which acts along the vertical axis[1]. In the tilted trap the gravitational force also influences the potential along the direction of beam propagation. Along this direction the dipole and gravitational force are comparable at the used optical powers. Therefore it is necessary to calculate the critical value of the dipole potential U_{crit} at which dipole and gravitational force compensate each other. At this value the local potential minimum disappears and it becomes impossible to trap atoms (see fig. 5.2). The resulting force $F_y(y)$ acting on an atom in the horizontal beam in direction of gravity is given by

$$F_y(y) = F_{\text{dip},y} - mg = -\frac{\partial U(0,y,0)}{\partial y} - mg = -|U_0| \cdot \frac{4y}{w_0^2}\exp(-\frac{2y^2}{w_0^2}) - mg, \qquad (5.1)$$

where w_0 denotes the beam waist, m is the atomic mass, g is the gravitational acceleration and U_0 is the dipole potential of the ground state: $U_0 = -\alpha_g I(0,0,0)/(2\epsilon_0 c)$ (see eq. 4.1). The dipole force $F_{\text{dip},y}(y)$ has its maximum at $y = -w_0/2$. For holding atoms in the dipole trap, it is necessary that the dipole force at this point dominates over the gravitational force. Therefore the condition $|U_0| > |U_{\text{crit}}|$ must be fulfilled, with

$$U_{\text{crit}} = -mg \cdot \frac{w_0}{2}\exp(1/2). \qquad (5.2)$$

[1] In this chapter the vertical axis is denoted as y-axis.

If the beam propagates along the direction of gravity the resulting force is given by

$$F_y(y) = F_{\text{dip},y} - mg = -\frac{\partial U(0,y,0)}{\partial y} - mg = -\,|U_0| \cdot \frac{2y}{y_{\text{R}}^2} \cdot \left(1 + \left(\frac{y}{y_{\text{R}}}\right)^2\right)^{-2} - mg. \quad (5.3)$$

The dipole force $F_{\text{dip},y}(y)$ reaches its maximum at $y = -y_{\text{R}}/\sqrt{3}$ and the critical value for the dipole potential is given by

$$U_{\text{crit}} = -mg \cdot \frac{8 y_{\text{R}}}{\sqrt{3}^3}, \quad (5.4)$$

where $y_{\text{R}} = \pi w_0^2/\lambda$ denotes the Rayleigh length. Equations 5.2 and 5.4 show that the critical value $|U_{\text{crit}}|$, below which the local minimum disappears, depends on the trap confinement. For the potential along the axis of strong confinement in equation 5.2, $|U_{\text{crit}}|$ corresponds to an optical power of about 50 mW for the relevant trap parameters (polarizability of the ground state α_g at 1030 nm, $w_0 = 33\,\mu$m). Due to the smaller confinement in the axial direction along the beam propagation in the tilted trap (see eqn. 5.4), the optical power has to be above $P_{\text{crit}} = \epsilon_0 c \pi w_0^2\,|U_{\text{crit}}| \cdot \sin(\varphi)/\alpha_g = 3.2$ W in order to realize a local minimum. The angle $\varphi = 20^\circ$ accounts for the tilt of the trapping beam with respect to the horizontal plane.

The potential of the crossed-beam optical dipole trap shows three different regimes, which depend on the ratio of the optical power ($P_{\text{hor}}/P_{\text{tilt}}$) of the horizontal and the tilted beam (see fig. 5.3). Atoms can be stored in the crossing region of the two beams (dimple) and additionally in one of the single-beam dipole traps, which surrounds the dimple. In the following the potential is described by the depth of the dimple U_{Dimple} and by the potential barrier b, which is determined by the tilted trap:

- In case a) the potential of the horizontal trap dominates the potential of the crossed-beam trap ($P_{\text{hor}} > P_{\text{tilt}}$). Atoms are mainly stored in the horizontal trap, since the potential barrier b is high enough to prevent a loss of atoms in direction of the tilted beam. The dipole force in this beam is too small to support atoms against gravity. The depth of the dimple U_{Dimple} is identical with the depth of a dipole trap realized with a power of P_{tilt} if the influence of gravity is not considered.

- If the power in both beams are similar, one only observes atoms in the crossed region (case b)). Here the potential depth of the dimple U_{Dimple} achieves its maximum in comparison to the other situations. Atoms escape from the horizontal trap over the small barrier b of the tilted trap and after a storage time of 0.5 s (see fig. 5.4) only atoms in the dimple remain.

- If the power in the tilted trap is higher than the power in the horizontal one, atoms with high kinetic energy leak along the tilted beam axis over the potential barrier b (case c)). The potential depth U_{Dimple} is identical with the depth of the horizontal trap.

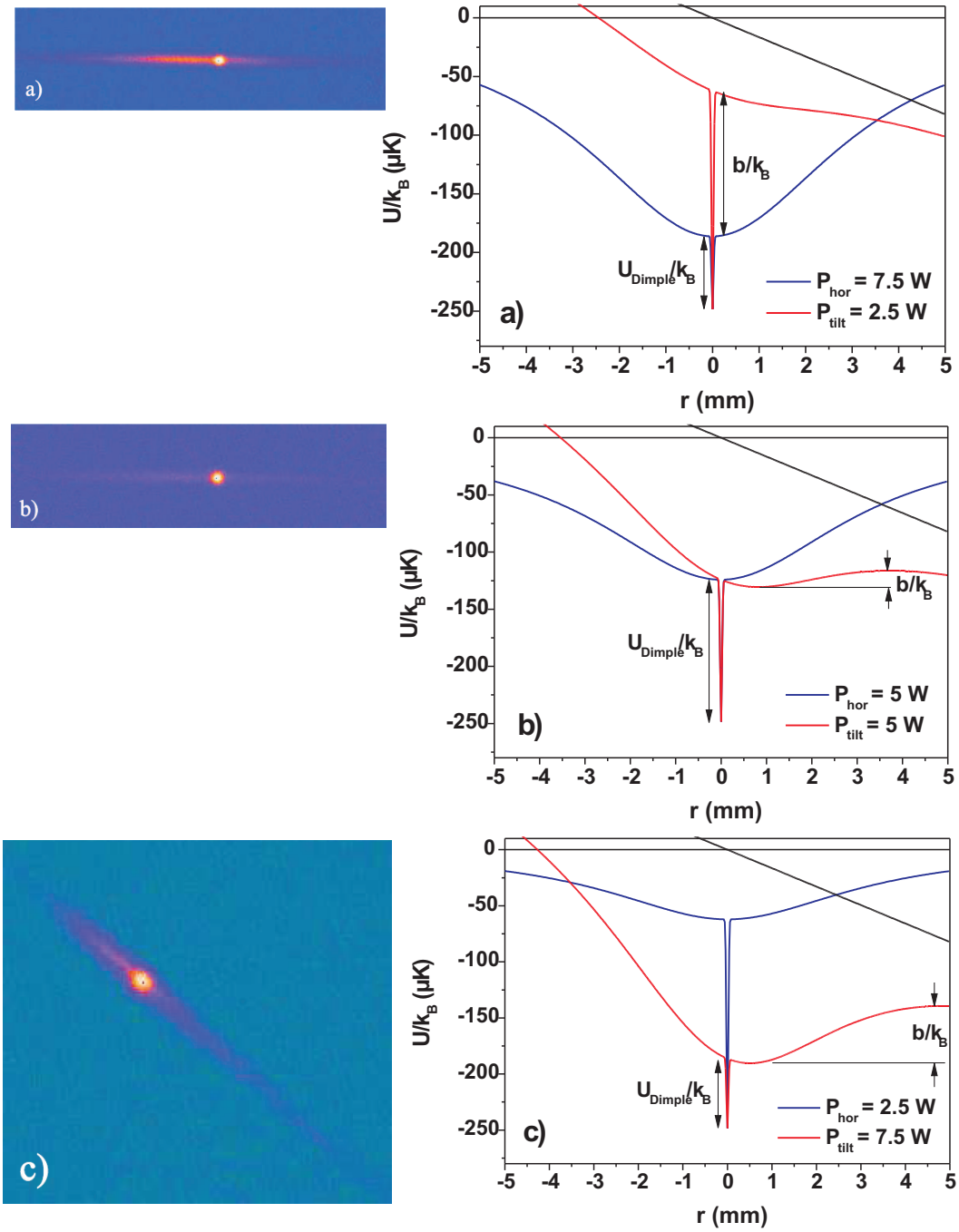

Figure 5.3: *The potential of the crossed-beam dipole trap for different optical power ratios in the two laser beams and the corresponding absorption images of the atomic cloud after* 1 *ms of expansion. The atoms were stored in the potential for* 0.5 *s (see fig. 5.4). The respective potential along the laser beam is shown. The black line shows the gravitational potential in the tilted trap. The potential of the tilted trap and the horizontal trap is indicated by a red and blue line, respectively. If the higher power is concentrated in the horizontal beam the atoms are mainly stored in the horizontal trap (case a)). In the case of similar power (case b)) the atoms escape in direction of the tilted trap since here the lowest potential barrier (denoted by b) is realized. Now the potential depth in the crossing point* U_{Dimple} *achieves its maximum. The barrier b is further lowered if the power in the tilted beam becomes higher than in the horizontal ones (case c)).*

For the determination of the density and the phase-space density of the ensemble in the dimple potential it is necessary to know the trap frequencies. For small extensions of the atomic sample the dipole potential of the crossed-beam trap $U_{\mathrm{cb}}(x,y,z)$ can be approximated by

$$U_{\mathrm{cb}}(x,y,z) = -|U_1|\left(1-\frac{2(x^2+z^2)}{w_0^2}\right) - |U_2|\left(1-\frac{2(y^2+z^2)}{w_0^2}\right), \tag{5.5}$$

where $|U_1|$ and $|U_2|$ are the potential depths of the single-beam dipole traps. For the trap frequencies follows

$$\omega_{\mathrm{x}} = \sqrt{\frac{4\,|U_1|}{mw_0^2}}, \qquad \omega_{\mathrm{y}} = \sqrt{\frac{4\,|U_2|}{mw_0^2}} \qquad \text{and} \qquad \omega_{\mathrm{z}} = \sqrt{\frac{4(|U_1|+|U_2|)}{mw_0^2}}. \tag{5.6}$$

The single-beam trap with the smaller potential depth $|U_i|$, with $i = 1, 2$, determines the effective depth of the dimple trap. Its value is identical with above introduced U_{Dimple}. With the mean frequency $\bar{\omega} = (\omega_x\omega_y\omega_z)^{1/3}$ the peak value of the density ρ_0 and the phase-space density ζ can be calculated

$$\rho_0 = N\left(\frac{m\bar{\omega}^2}{2\pi k_{\mathrm{B}}T}\right)^{3/2}, \qquad \zeta = N\left(\frac{\hbar\bar{\omega}}{k_{\mathrm{B}}T}\right)^{3}, \tag{5.7}$$

here N denotes the number of trapped atoms. The derived frequencies ω_x and ω_y are only valid if the two beams are crossed under an angle of $90°$. However the tilted beam and the horizontal beam are crossed under an angle of $\delta \approx 54°$ in the plane, which they define. For the same power in both beams, the main axis of the two trap frequencies are defined by the four points at which the intensity in both beams is drop off to $1/e^2$. From geometrical considerations the mean frequency in the plane of the two beams can be derived as $\omega_{\mathrm{plane}} = \omega_x\omega_y\sin(\delta)$, where ω_x and ω_y are the radial frequencies of the tilted and the horizontal trap (see 5.6). The mean frequency is then given by $\bar{\omega} = \left(\omega_{\mathrm{plane}}\omega_z\right)^{1/3}$. Exact calculations of the trap frequencies showed, that this approximation of the mean frequency $\bar{\omega}$ is still applicable for a power ratio of $1/2$, which is also used in the following investigations.

5.1.2 Influence of the power ratio $P_{\mathrm{hor}}/P_{\mathrm{tilt}}$ on the sample properties

To obtain a better understanding of the behavior of the atoms in the crossed-beam trap, this section experimentally investigates the influence of the optical power ratio between horizontal and tilted trap $P_{\mathrm{hor}}/P_{\mathrm{tilt}}$.

The number of atoms in the dimple and in the horizontal trap was measured by absorption images for different configurations of U_{Dimple} and b, realized by different ratios $P_{\mathrm{hor}}/P_{\mathrm{tilt}}$. For this purpose both dipole traps were temporary and spatially overlapped to the two-stage MOT and after a storage time of 0.5 s the number of atoms was detected (see fig. 5.4). Starting from a four times smaller Stark poten-

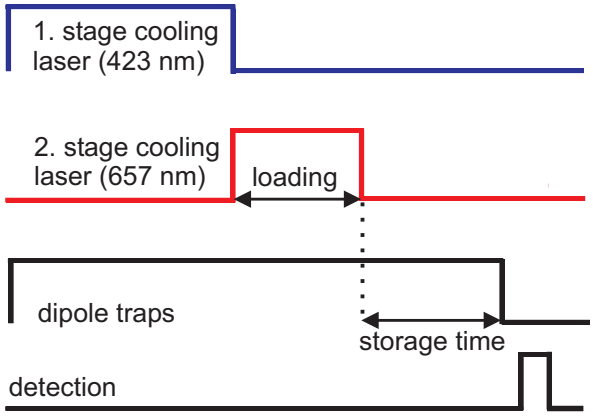

Figure 5.4: *Time sequence for the measurements in the crossed-beam dipole trap. After the usual preparation of atoms in the two-stage MOT both dipole traps are loaded. After the storage time an absorption image is taken.*

tial in the tilted trap than in the horizontal one (a situation comparable to case a) in fig. 5.3), the optical power was increased gradually until a power ratio of about 1 is realized (see case b) in fig. 5.3). For atoms in the horizontal trap, the increasing power in the tilted trap lowers the potential barrier b in direction of the tilted trap (compare case a) and b) in figure 5.3) and more and more atoms escape from the horizontal trap. Figure 5.6 a) therefore shows a falling number of atoms in the horizontal trap if the potential barrier b is reduced. The potential shapes show (see again fig. 5.3), that the trap depth in the crossing region U_{Dimple} increases with increasing power in the tilted trap. With an increasing trap depth U_{Dimple} in the dimple, the number of atoms in this region starts to increase, reaches a maximum around $U_{\mathrm{Dimple}}/k_{\mathrm{B}} = 80\ \mu$K and above this value the particle number again drops down. If the trap depth is increased, more and more atoms with higher kinetic energy could be captured in the crossing region. The final number of atoms around $3.5 \cdot 10^5$ seems to be limited by the density in the sample ($6 \cdot 10^{13}$ cm^{-3}). The limitation seems to be independent on the measurement sequences. The red colored points are measured if the dimple is loaded without the MOT (see fig. 5.5), which indicates that not light assisted collisions limit the number of atoms but three-body losses (see the following section). The decreasing number of atoms for larger trap depths is due to the smaller number of atoms in the horizontal trap at this power ratio, which results in a stop of loading (compare the upper curve in fig. 5.6 a)).

The investigation of the time evolution of the dimple atoms verify this assumption of a continuous loading of the dimple from the horizontal trap. The time evolution is measured for two ratios of optical power, if the dimple is loaded without MOT (see fig. 5.5). In the first case a depth of the dimple of $U_{\mathrm{Dimple}}/k_{\mathrm{B}} = 87\ \mu$K and a potential barrier of $b/k_{\mathrm{B}} = 70\ \mu$K was realized with a power of 6.5 W in the horizontal and 3.5 W in the tilted beam. These parameters result in $3.5 \cdot 10^5$ atoms in the dimple and $1.7 \cdot 10^6$ in the horizontal trap after a storage time of 0.5 s. In the second case a trap depth of $U_{\mathrm{Dimple}}/k_{\mathrm{B}} = 124\ \mu$K and a barrier of $b/k_{\mathrm{B}} = 7\ \mu$K was realized by a horizontal power of 4.7 W and a tilted power of 5.2 W. The corresponding number

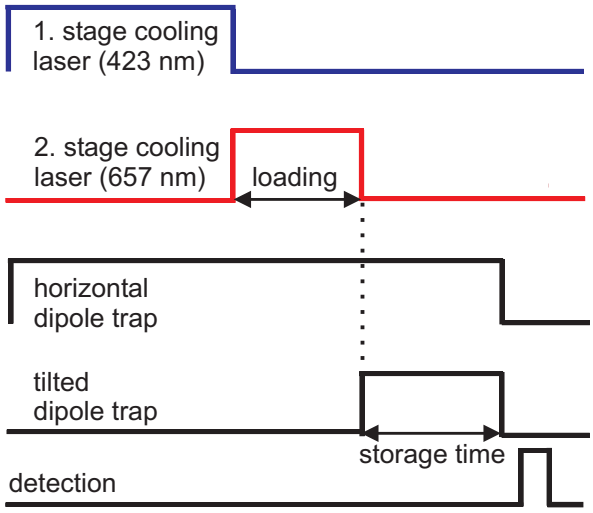

Figure 5.5: *Measurement sequence for the crossed-beam optical dipole trap. In comparison to the sequence in figure 5.4 the tilted trap will be overlapped to the horizontal one after switching-off the MOT.*

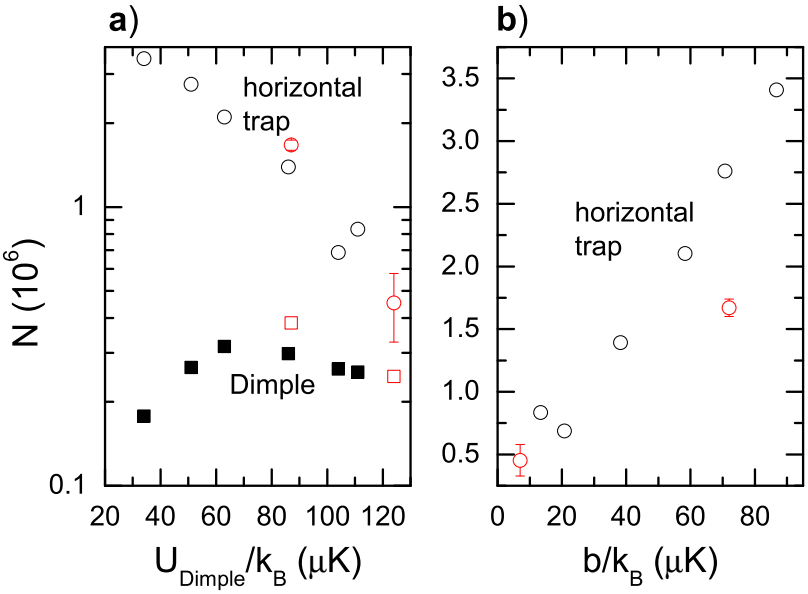

Figure 5.6: *Number of atoms in the crossing region and in the horizontal trap plotted against the potential depth of the dimple U_{Dimple} (figure a)). The number of atoms in the horizontal trap depends on the potential barrier b (figure b)), induced by the overlapping potential of the tilted trap. For trap depths of the dimple around 80 μK the number of atoms reaches a maximum. This is attributed to a limitation in density and a decrease in the reloading from the horizontal trap. The red colored points are from identical measurements realized, if the dimple is loaded without MOT.*

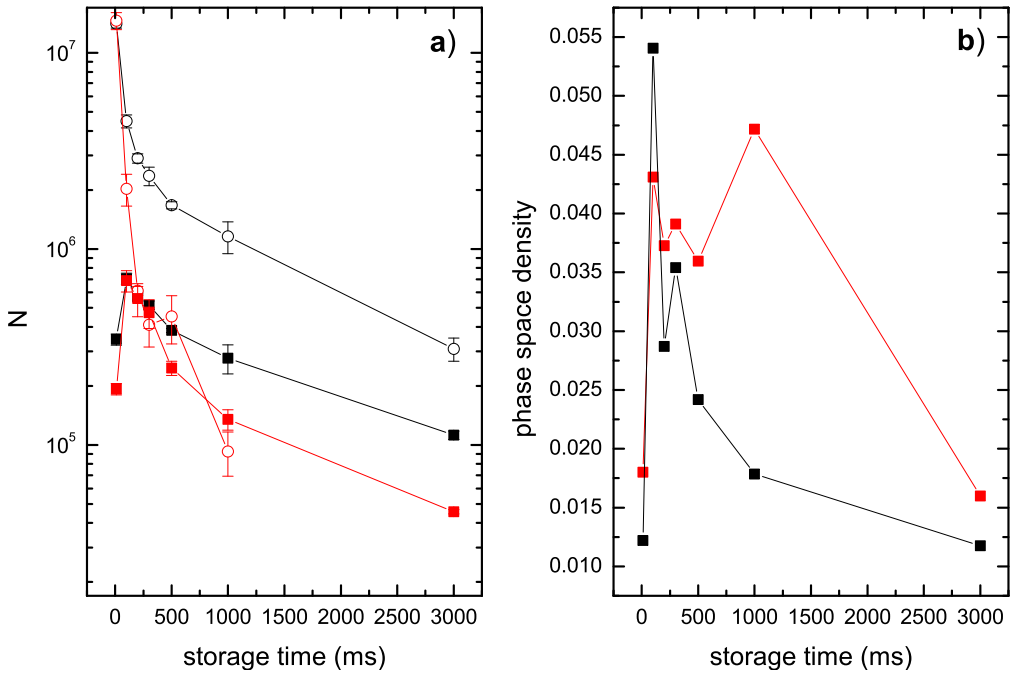

Figure 5.7: *Number of atoms in the dimple (squares) and in the horizontal trap (circles) as a function of storage time for different power ratios a). The corresponding phase-space density is shown in b). For a power of* 6.5 *W in the horizontal trap and* 3.5 *W in the tilted trap (black lines) a partly compensation of the atoms lost from the dimple is observed due to a reloading from the horizontal trap. A continuous loading is prevented in the case of similar powers with* 4.7 *W in the horizontal and* 5.2 *W in the tilted trap (red lines). This results in a lower number of atoms and a higher phase-space density, since an heating effect from the continuously loaded atoms does not take place.*

of particles are $2.5 \cdot 10^5$ in the dimple and $4.5 \cdot 10^5$ in the horizontal trap.

During the whole storage time the number of atoms are higher in the first case with $P_{\mathrm{hor}} = 6.5$ W, since atoms from the horizontal trap are continuously loaded. Without this loading process in the second case $P_{\mathrm{hor}} = 4.7$ W, atoms in the dimple disappear faster for storage times $t > 200$ ms. In both cases atoms are lost due to evaporation as indicated by the decrease of temperature (see fig. 5.8). During the loading process atoms from the horizontal trap are accelerated into the crossing region, which results in higher ensemble temperatures around 16 μK and lower phase-space densities compared to 11 μK in the second case. For this dimple, realized with a similar power, an ensemble lifetime of (1.6 ± 0.1) s was estimated from the decay curve. For the other case a higher lifetime of (2.00 ± 0.05) s was observed, which is obviously due to atoms, which are continuously loaded from the horizontal trap. The decay in the horizontal trap depends on the potential barrier b. In the first case ($b/k_{\mathrm{B}} = 70$ μK) a lifetime of (1.4 ± 0.1) s was observed after the evaporation. Due to the low barrier b almost all atoms are lost from the horizontal trap after a storage time of 1 s. The observed lifetime in the dimple is smaller than the lifetimes

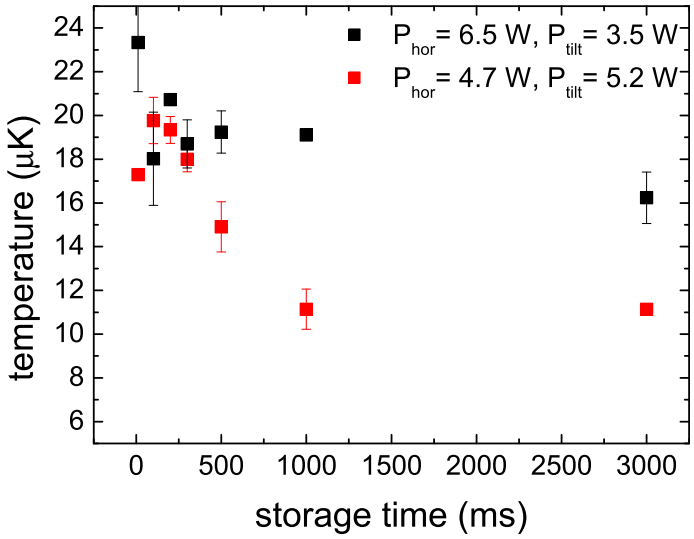

Figure 5.8: *Ensemble temperatures in the dimple as a function of the storage time. The black squares indicate the temperatures, which are observed for the atoms stored in a crossed-beam trap with a power of* 6.5 *W in the horizontal and* 3.5 *W in the tilted beam. The resulting temperatures for similar powers in the horizontal* (4.7 *W) and the tilted trap* (5.2 *W) are indicated by red squares.*

in the dipole trap ($\tau_{\mathrm{Dip}} = 3.6$ s), since the vacuum was not as good as during the measurements with the single-beam dipole trap (see chapter 4).

With regard to a subsequent evaporation the configuration realized with different powers has the advantage, that the atoms in the horizontal trap can serve as a reservoir during the forced evaporation process. In a similar configuration Griesmaier *et al.* [Gri05, Gri06] could evaporatively cool ^{52}Cr towards quantum-degeneracy. Due to the continuous loading from the reservoir, the number of atoms in the dimple stood nearly constant during the evaporation process.

5.1.3 Adiabatic generation of the crossed-beam dipole trap

The effect of an adiabatic generation of the dimple potential was studied by varying the time during which the power of the tilted dipole trap was ramped up (ramping time t_{ramp}). The ramping was started after the loading of the horizontal trap was completed, by switching-off the MOT. After the ramp was finished, the atoms were stored for 100 ms in the crossed trap and were then detected by an absorption image. With a maximum power of 3.5 W in the tilted beam and 5.4 W in the horizontal one, a 86 μK deep dimple and a 47 μK high potential barrier could be realized. Figure 5.9 shows the ratio $N_{\mathrm{Dimple}}/N_{\mathrm{total}}$ as a function of the ramping time. Here N_{Dimple} is the number of atoms in the dimple and $N_{\mathrm{total}} = N_{\mathrm{Dimple}} + N_{\mathrm{Dip}}$ is the total number of atoms in dimple and horizontal trap. For the comparison of the different ramping times t_{ramp}, it is necessary to consider the lifetime of the different traps

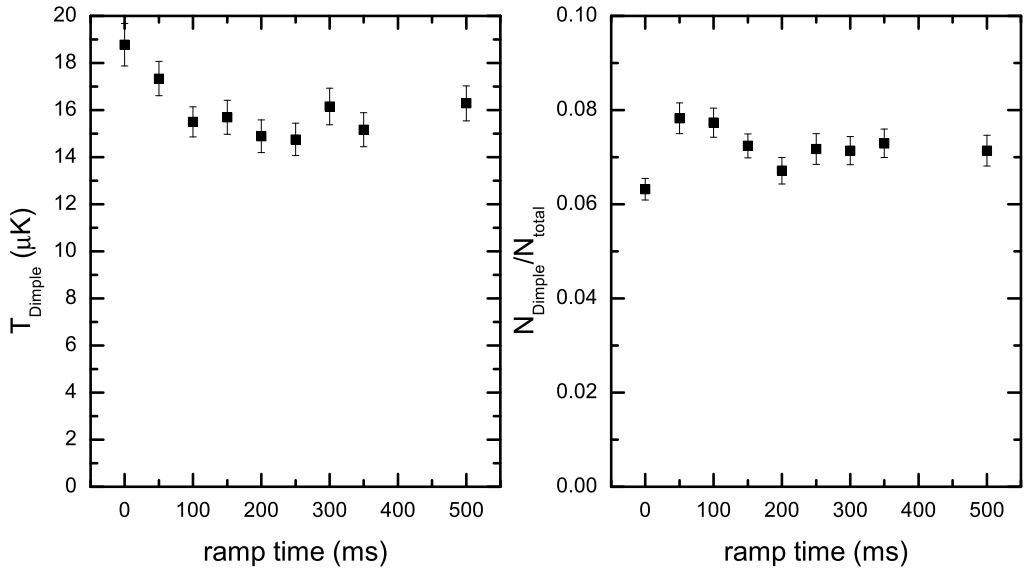

Figure 5.9: *Adiabatic generation of the dimple potential. Left: evolution of the ensemble temperature in the dimple as a function of different ramping times and right: the corresponding ratio N_{Dimple}/N_{total} (see text).*

($\tau_{\text{Dimple}} = 2$ s, $\tau_{\text{Dip}} = 1.4$ s). The particle numbers are therefore corrected by the factor $\exp(t_{\text{ramp}}/\tau_{\text{Dimple}})$ and $\exp(t_{\text{ramp}}/\tau_{\text{Dip}})$, respectively.

The data of the ratio $N_{\text{Dimple}}/N_{\text{total}}$ do not show an obvious difference between a sudden ($t_{\text{ramp}} = 0$ ms) and a slow ($t_{\text{ramp}} > 0$ ms) generation of the trapping potential of the dimple. However a slow and adiabatic generation has the advantage, that for the same ratio $N_{\text{Dimple}}/N_{\text{total}}$ a slightly smaller ensemble temperature could be realized. If the tilted trap is switched on with a ramping time of $t_{\text{ramp}} \geq 100$ ms a sample temperature around 16 μK could be observed whereas a sudden switching ($t_{\text{ramp}} = 0$ ms) produces temperatures around 19 μK. The adiabatic generation of the dimple with $t_{\text{ramp}} = 100$ ms allows therefore to increase of the phase-space density from about 0.02 ($t_{\text{ramp}} = 0$ ms) to approximately 0.04. The adiabatic generation of the dimple potential could not increase the number of atoms in the dimple and the ratio $N_{\text{Dimple}}/N_{\text{total}}$, which is probably due to a density limiting process. Although the dimple was generated abruptly ($t_{\text{ramp}} = 0$ ms), the measurements of section 5.1.2 show similar phase-space densities of about 0.045. This can be explained by the fact, that the whole power ($P_{\text{hor}} + P_{\text{tilt}} = 10$ W) in these measurements were higher, which results in a deeper potential and therefore according to equation 5.6 in higher trap frequencies and a higher phase-space density. Furthermore the position of one beam focus relative to the other can differ from measurement to measurement resulting in slightly different particle numbers and temperatures in the dimple.

5.2 Three-body losses in the crossing region

The previous investigations showed that the number of atoms, which can be transfered in the dimple, is limited on the one hand by the number of remaining atoms in the horizontal dipole trap and on the other hand by density dependent loss processes. Although the effect of photoassociative losses should be avoided if the dimple is loaded without MOT (see fig. 5.5), the number of atoms and the density in the dimple remained similar to the case in which the dimple is loaded with the MOT (see fig. 5.4). Furthermore an adiabatic formation of the dimple potential could not increase the number of dimple atoms. A density limiting process, which is independent from the 657 nm radiation of the MOT light, is the three-body recombination.

In this process three atoms collide and two of them form a dimer whereas the molecular binding energy ϵ is set free as kinetic energy. This energy is transfered to the created molecule ($\epsilon/3$) as well as to the third collision partner ($2\epsilon/3$). In comparison to the trap depth the released binding energy ϵ is large and the created molecule and the single atom escape from the trap. The event rate in this process is proportional to the third power of the sample density ρ. This section estimates the corresponding three-body loss coefficient L_3 from a decay measurement in the dimple and analyses its influence on the dimple atoms.

The measurement was carried out by loading the dimple without MOT (see fig. 5.5) to avoid two-body losses. With similar optical powers in both beams ($P_{\text{hor}} = 4.6$ W, $P_{\text{tilt}} = 4.8$ W) a background of atoms in the horizontal trap is only marginal. After about 100 ms nearly all atoms in the horizontal trap are disappeared and further loading of the dimple stops (see the following section). Then the decay of the number of atoms is measured. Besides the determination of the particle number in the dimple, the sample temperature is measured simultaneously by the time-of-flight technique in order to distinguish, if the first fast decay is due to evaporation of atoms with high kinetic energy or due to three-body losses.

Figure 5.10 shows the results of the decay and the temperature measurements. During the loss of atoms the temperature fluctuates around a value of 29 μK and seems to be independent, which indicates a three-body loss process and not a plain evaporation. The three-body loss of atoms in the dimple is described by the following differential equation

$$\dot{N}_{\text{Dimple}} = -L_3 \int d^3r \rho^3(\vec{r}) = -L_3 \left\langle \rho^2 \right\rangle N_{\text{Dimple}}, \tag{5.8}$$

with L_3 as three-body loss coefficient and $\langle \rho^2 \rangle$ as mean of the squared density. To deduce an equation in N, the three-body loss rate $L_3\rho^3$ is integrated over the sample volume under the assumption of thermal equilibrium (see section 4.2.3). In equation 5.8 the losses due to background collisions are not considered, since these losses are expected to become important only for longer storage times. After transforming the mean of the squared density into the number of atoms, one obtains

$$\dot{N}_{\text{Dimple}} = -\frac{L_3}{\sqrt{27}} \left(\frac{m\bar{\omega}^2}{2\pi k_{\text{B}} T} \right)^3 \cdot N^3_{\text{Dimple}} = -l_3 \cdot N^3_{\text{Dimple}}, \tag{5.9}$$

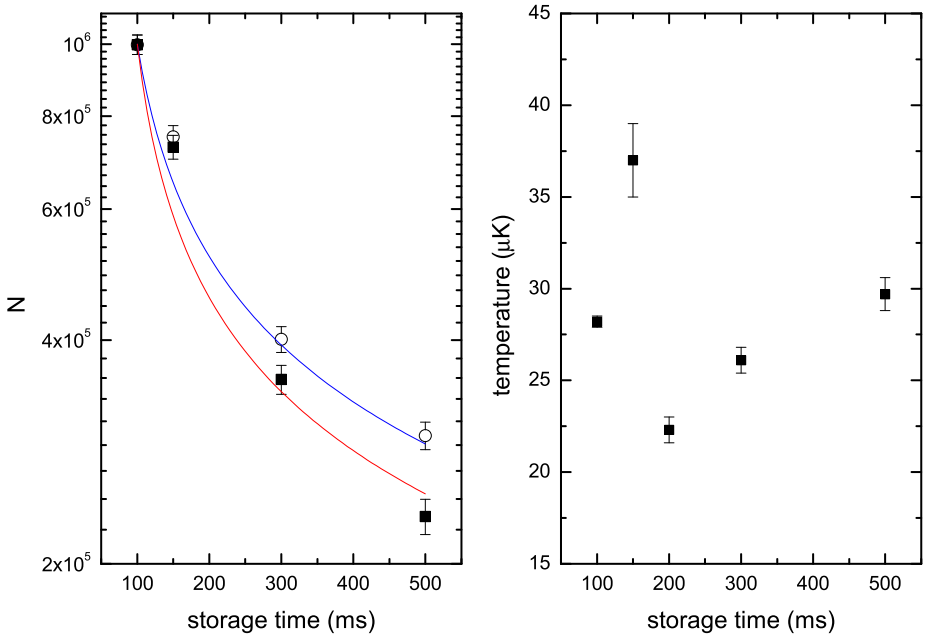

Figure 5.10: *Number of atoms (left) and the corresponding temperatures (right) in the dimple as function of the storage time. The black circles in the left graph show the particle numbers, which are corrected for background losses (see text). The red and blue curve are fits to the data according to equation 5.10.*

with the solution

$$N_{\text{Dimple}}(t) = \left(N_0^{-2} + 2l_3 t\right)^{-1/2}. \tag{5.10}$$

In equation 5.9 is $\bar{\omega}$ the mean trap frequency, m the atomic mass, T the temperature of the sample and k_{B} the Boltzmann constant. If the background losses are neglected the derived L_3 coefficients are to high. The particle numbers are corrected for background losses by multiplying the data with the factor $\exp(t/\tau_{\text{Dimple}})$. The lifetime $\tau_{\text{Dimple}} = 1.6$ s was determined from a separate measurement at low density and long storage times. With this correction the densities are overestimated which leads to smaller L_3 coefficients. The fits (see fig. 5.10) to the data with (blue curve) and without background correction (red curve) therefore determine the range of the three-body loss constant: $3 \cdot 10^{-27}$ cm^6/s$\leq L_3 \leq 4 \cdot 10^{-27}$ cm^6/s.

To classify this value a comparison to the L_3 coefficients of other atomic species is helpful. Theoretical investigations [Fed96] showed, that the three-body loss coefficient scales with the fourth power of the ground state scattering length a. This scaling is valid in the low-energy limit for large positive scattering lengths. With its lower value of the ground state scattering length $a = 340\ a_0$ the calcium coefficient follows together with the values of the other species nearly this theoretical prediction. The L_3 coefficients scale with an exponent of 4.4 ± 0.2. The three-body loss

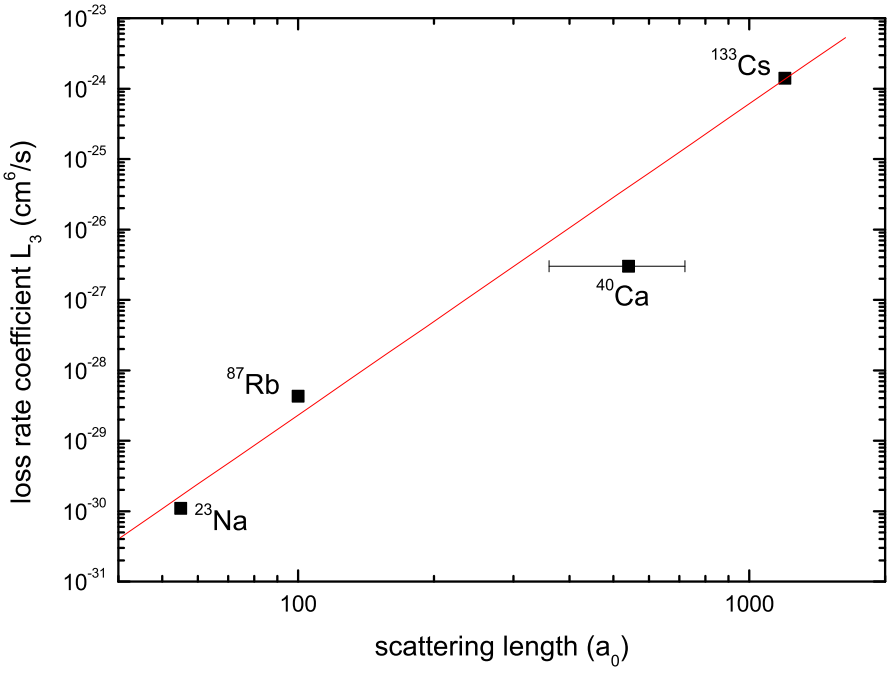

Figure 5.11: *Three-body loss coefficients of different atoms as function of their ground state scattering length. The L_3 constants nearly agree with the theoretically predicted a^4 upper limit. For a value of 340 a_0, which is the lower boundary of the determined scattering length, ^{40}Ca also follows this scaling.*

rate constant for sodium is measured in a condensate [Sta98] and the loss rate constants of ^{87}Rb [Bur97] as well as ^{133}Cs are non-condensate values like in the case of calcium. In the case of cesium the scattering length is magnetically tuned to a value of $a = 1200a_0$ [Web03b].

The estimated three-body loss coefficient leads at the realized dimple densities ($6 \cdot 10^{13}$ cm^{-3}) to a loss rate of approximately $10/$s, which is comparable to the loss rates due to two-body collisions (see fig. 5.12). It is therefore likely that in both sequences the particle number in the dimple is similar.

For an effective evaporative cooling in the crossed-beam optical dipole trap it is important, that the rate for inelastic two- and three-body collisions are significantly smaller than the rate for elastic collisions. The rate for elastic collisions γ_{el} is given by

$$\gamma_{\mathrm{el}} = \langle\rho\rangle\, \sigma_{\mathrm{el}}(T)\bar{u}(T), \tag{5.11}$$

with the mean density $\langle\rho\rangle = \int \rho^2(\vec{r})d^3r / \int \rho(\vec{r})d^3r = \rho_0/\sqrt{8}$, the mean relative velocity $\bar{u}(T) = 4\sqrt{k_{\mathrm{B}}T/\pi m}$ and $\sigma_{\mathrm{el}}(T)$ the elastic collision cross section. The cross section

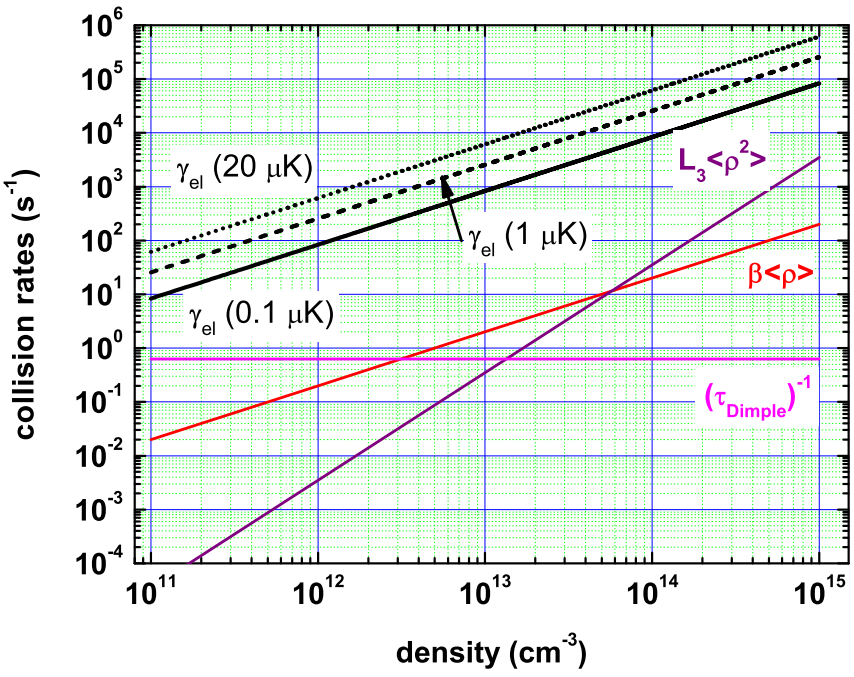

Figure 5.12: *Comparison of the elastic and inelastic collision rates for calcium as a function of density. The elastic collision rates γ_{el} are shown for different temperatures. The inelastic rates are due to two- $\beta\langle\rho\rangle$ and three-body losses $L_3\langle\rho^2\rangle$. Losses due to background collisions are indicated by τ^{-1}_{Dimple}.*

for an ensemble of identical bosons is given by [Dal99]

$$\sigma_{\mathrm{el}}(k_u) = \frac{8\pi a^2}{1 + k_u^2 a^2}, \tag{5.12}$$

with the relative atomic wave number $k_u = um/2\hbar$, depending on the relative velocity u. The expression leads to two limiting cases; for low energies ($k_u a << 1$) follows $\sigma_{\mathrm{el}}(k_u) = 8\pi a^2$ and for high energies ($k_u a >> 1$) the cross section reaches the so-called unitarity limit $\sigma_{\mathrm{el}}(k_u) = 8\pi/k_u^2$. With the mean value of the relative velocity $\bar{u}(T)$ a temperature dependent expression for σ_{el} can be derived

$$\sigma_{\mathrm{el}}(T) = \frac{8\pi^2 a^2 \hbar^2}{\pi\hbar^2 + 4k_{\mathrm{B}} T m a^2}. \tag{5.13}$$

Figure 5.12 compares the calculated elastic collision rates γ_{el} for different temperatures with the measured inelastic rates of two- $\beta\langle\rho\rangle$ and three-body $L_3\langle\rho^2\rangle$ collisions as well as the loss rate due to background collisions[1] $\tau^{-1}_{\mathrm{Dimple}}$. The elastic collision

[1]The rate of background collisions is calculated for the observed lifetime of the dimple ($\tau_{\mathrm{Dimple}} = 1.6$ s).

rates are calculated for the lower boundary of the scattering length $a = 340a_0$. Starting from a rate corresponding to the temperature of the present dimple ensemble ($20\ \mu$K), the elastic collision rates are calculated as well for temperatures ($1\ \mu$K and $0.1\ \mu$K) at which quantum-degeneracy is reached in other atomic species. Around temperatures of $1\ \mu$K and below, the cross section can be described by its temperature independent low energy limit $\sigma_{\text{el}} = 8\pi a^2$. These description is for temperatures around $20\ \mu$K not verified, since the cross section only amounts 60% of its low energy limit. Around temperatures of $200\ \mu$K the cross section reaches the unitarity limit. Over the full range of ensemble densities the elastic collision rates are significantly higher than the inelastic ones. Especially at sample densities between 10^{14} cm^{-3} and 10^{15} cm^{-3}, at which BECs are normally realized, the elastic collision rate at $0.1\ \mu$K is more than one order of magnitude larger in comparison to the three-body loss rate. This should allow an efficient evaporative cooling starting from the present ensemble in the dimple.

5.3 Loading behavior of the crossing region

The transfer of atoms from the horizontal dipole trap to the dimple is analysed without the second stage of the MOT. In the corresponding measurement sequence (see fig. 5.13) the tilted dipole trap overlaps the horizontal one for a variable time, but the detection always happens after the same period of time with respect to the turn-off of the MOT. In the comparison of different overlap times the influence of background collisions is therefore identical and can be neglected in this analysis. The measurement were carried out at similar optical powers P in the trapping beams ($P_{\text{hor}} = 4.4$ W, $P_{\text{tilt}} = 5.1$ W). Figure 5.14 shows how the number of atoms in the dimple and the horizontal trap depends on the overlap time. The atom number in the horizontal trap decays fast (220 ms) whereas the number of atoms in the dimple increases meanwhile until 10% of the intially stored atoms in the horizontal trap are transfered. Most atoms leave the trap after passing the crossing region over the potential barrier, which has a hight of approximately $b/k_{\text{B}} = 15\ \mu$K. Initially, directly after the tilted trap is switched on, the densities in dimple and horizontal trap are similar. Then during progressive overlap time the density increases until maximum densities around $6.7 \cdot 10^{13}$ cm^{-3} are achieved. The density increases due to elastic atom-atom collisions similar to the case of ytterbium [Tak03b] or cesium [Ham02]. The number of particles in the dimple grows until density dependent losses prevail and the horizontal trap is empty, which stops the loading of the dimple. The loading process can be described by the coupled differential equations

$$\begin{aligned} \dot{N}_{\text{Dip}}(t) &= -\tilde{\gamma}_{\text{Dip}} N_{\text{Dip}}(t) - \hat{r}_0 N_{\text{Dip}}(t) \\ \dot{N}_{\text{Dimple}}(t) &= \hat{r}_0 N_{\text{Dip}}(t) - l_3 \cdot N_{\text{Dimple}}(t)^3 \end{aligned} \tag{5.14}$$

where $\tilde{\gamma}_{\text{Dip}}$ describes the loss rate of atoms in the horizontal trap, $\hat{r}_0$ is the loading rate of the dimple and l_3 is the volume dependent three-body loss coefficient, introduced in equation 5.9. The losses due to background collisions do not need to be considered in this scheme (see above). The energy dissipation mechanism in the

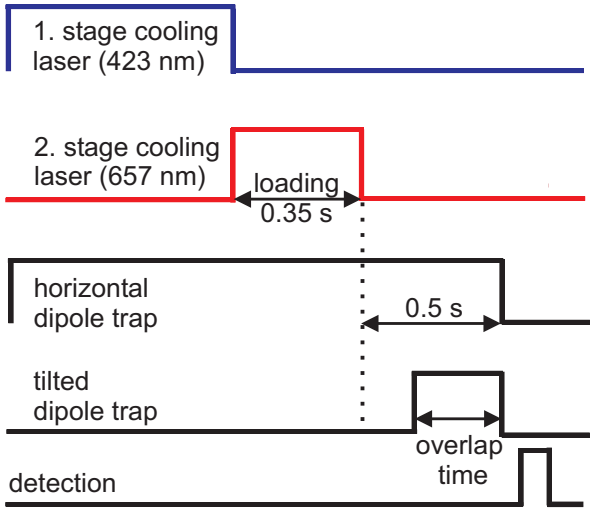

Figure 5.13: *Measurement sequence for the investigation of the loading behavior of the dimple.*

dimple is given by elastic atom-atom collisions. The loading rate $\hat{r}_0$ must be therefore proportional to the elastic collision rate γ_{el}

$$\begin{aligned} \hat{r}_0 &= q\gamma_{\mathrm{el}} = q\sigma(T)_{\mathrm{el}}\bar{u}(T)\,\langle\rho\rangle \\ &= q\sigma_{\mathrm{el}}(T)\bar{u}(T)\left(\frac{m\bar{\omega}^2}{2\pi k_{\mathrm{B}}T}\right)^{3/2}\frac{N_{\mathrm{Dip}}(t)}{\sqrt{8}} = \tilde{r_0}N_{\mathrm{Dip}}(t). \end{aligned} \tag{5.15}$$

Here q denotes the proportionality constant, $\sigma_{\mathrm{el}}(T)$ is the cross section and $\bar{u}(T)$ is the mean relative velocity. The mean density $\langle\rho\rangle$ in the horizontal trap is calculated from the mean frequency $\bar{\omega} = (\omega_r^2\omega_z)^{1/3}$, assuming thermal equilibrium (see section 4.2.3). By employing equation 5.15 for the differential equations follows

$$\begin{aligned} \dot{N}_{\mathrm{Dip}}(t) &= -\tilde{\gamma}_{\mathrm{Dip}}N_{\mathrm{Dip}}(t) - \tilde{r_0}N_{\mathrm{Dip}}^2(t) \\ \dot{N}_{\mathrm{Dimple}}(t) &= \tilde{r_0}N_{\mathrm{Dip}}^2(t) - l_3\cdot N_{\mathrm{Dimple}}^3(t). \end{aligned} \tag{5.16}$$

The numerical solution is fitted to the data (fig. 5.14) by varying the loading rate $\tilde{r_0}$ and the loss rate $\tilde{\gamma}_{\mathrm{Dip}}$. The three-body loss coefficient was kept constant at a value of $L_3 = 3\cdot 10^{-27}$ cm^{6}s^{-1} (see section 5.2). The initial loading rate of the dimple $\hat{r}_0 = \tilde{r_0}N_{\mathrm{Dip}}(0) = (1.7\pm 0.3)$ s^{-1} can be compared to the initial elastic collision rate, which is similar in the horizontal trap and in the dimple due to their equal initial densities. Under the assumption of a scattering length of $a = 340\,a_0$ and an average temperature of the ensemble of $T = 18\,\mu$K in dimple and horizontal trap, a collision rate of $\gamma_{\mathrm{el}} = 925$ s^{-1} can be derived. For the loading of the dimple only atoms in the crossing region contribute and the proportionality constant q is therefore estimated by the ratio of the volumes[1] $q = V_{\mathrm{Dimple}}/V_{\mathrm{Dip}} = 1/180$. In average one of the colliding atoms gets lost and carries away the excess of kinetic energy, which results in a

[1]The volumes are calculated in the harmonic approximation: $V = \left(\frac{m\bar{\omega}^2}{2\pi k_{\mathrm{B}}T}\right)^{-3/2}$, with $\bar{\omega}$ as mean frequency of the dipole trap or the dimple.

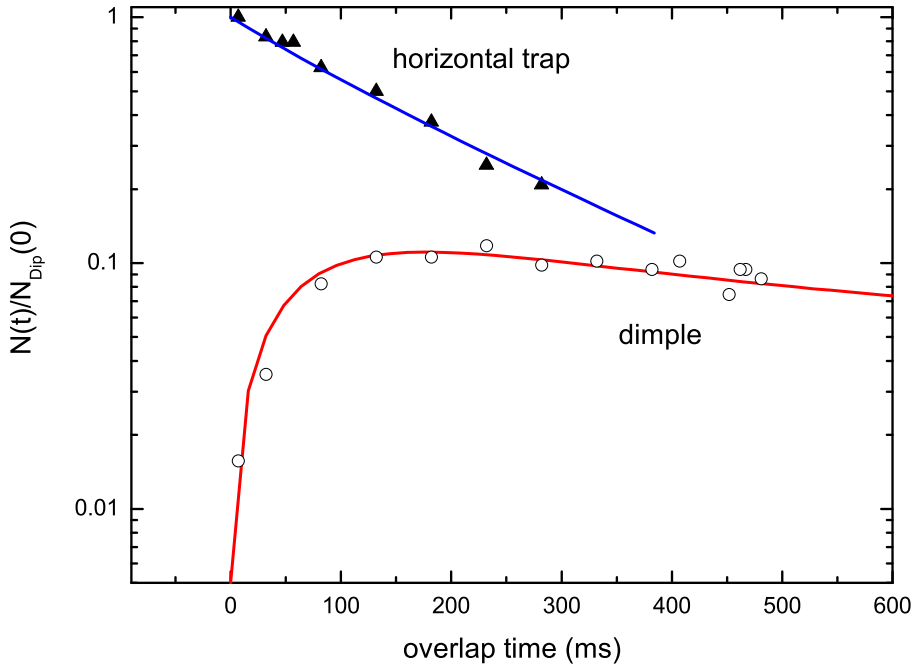

Figure 5.14: *Loading of the dimple without MOT. Initially $N_{Dip}(0) = 2.4 \cdot 10^6$ atoms are trapped in the horizontal dipole trap, which very fast escape (blue curve with an exponential time constant of 220 ms). The loading behavior of the dimple is described by the numerical solution of equation 5.16. Only the loading rate of the dimple is varied (red curve).*

value of $0.5\gamma_{\mathrm{el}}q = 2.6\ \mathrm{s}^{-1}$. The approximated value of the initial loading rate of the dimple $\hat{r}_0$ therefore confirms the order of magnitude of the measured value. The small discrepancy between measured and approximated loading rate can be explained by the simplicity of the model. The model assumes identical temperatures of the ensembles in dipole trap and dimple, which do not change during the loading process. However the ensemble temperature in the dimple have an initial value of about $16\ \mu$K and a final temperature of $20\ \mu$K. Furthermore the density and volume calculation are based on the frequencies deviated from the harmonic approximation and not from a measurement. Especially in the crossed-beam trap the calculated frequencies could deviate from reality if for instance the overlap of the beam foci is not perfect. Finally only a range of the scattering length a is known.

The loading process of the dimple is also investigated in the presence of the MOT. The trap parameters (optical power ratio, temperature) are similar and the storage time (0.5 s) is identical but here the loading time (see fig. 5.4) is varied instead of the overlap time (see fig. 5.13). Although the background collisions must be taken into account, a comparison should be possible for the initial loading process, since

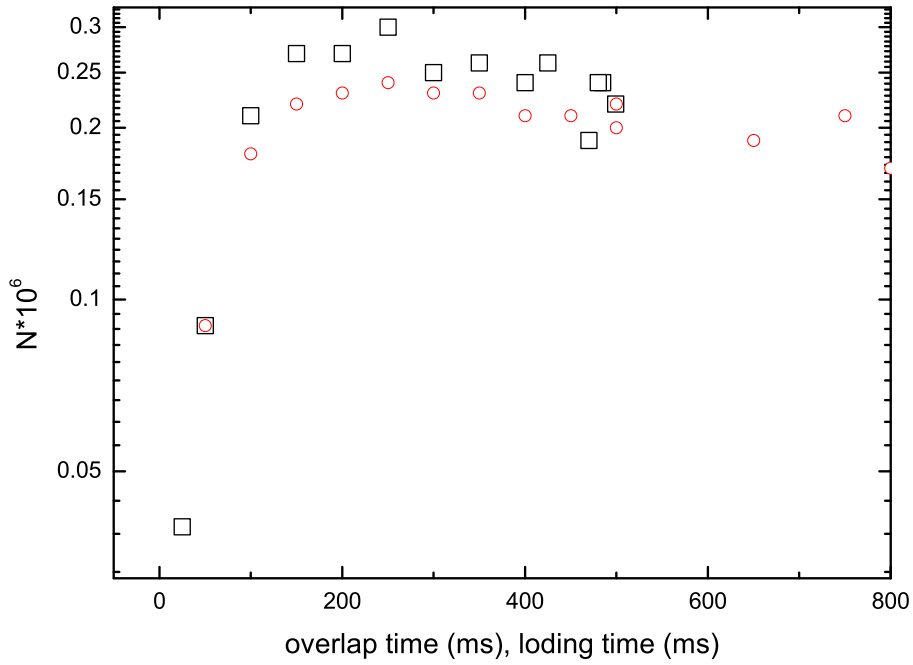

Figure 5.15: *Comparison of the loading behavior with and without MOT. The black squares denote the dimple loading without MOT by the variation of the overlap time and the red circles describe the loading with MOT by varying the loading time.*

for shorter storage times the loading rate and the density dependent loss rates prevail. In principal the loading process differs: a comparable loading of the horizontal dipole trap can not happened, because the atoms either escape in direction of the low potential barrier b or start to accumulate in the dimple. Therefore the dimple in principle is loaded by the MOT, whereas the capture range is probably given by the dipole trap. The accumulation of atoms in the dimple could be supported by elastic collisions as well as by laser cooling, comparable to the loading behavior in the single-beam dipole trap (see chapter 4). In the presence of the MOT, the density limitation in the dimple is given by three-body losses and light-induced two-body losses. The determined loss rate constants β and L_3 lead to a similar loss rates at the highest densities in the dimple (see fig. 5.12). Therefore the maximum transfer of atoms into the dimple is similar for both sequences.

Obviously the loading dynamics of the dimple is more complex in the presence of the MOT and for the development of a detailed model additional measurements are necessary.

5.4 Conclusion

A crossed-beam optical dipole trap for ^{40}Ca was experimentally realized and characterized. The trap is realized by a horizontally propagating laser beam and by a beam which is tilted by 20° with respect to the horizontal plane. Depending on the ratio of the optical power of the two beams the resulting potential allows not only to store atoms in the dimple but also in the horizontal dipole trap. The transfer of atoms from the horizontal trap into the dimple trap was analysed for different power ratios. A continuous loading of the dimple from the horizontal trap could be realized for a nearly two times higher power in the horizontal beam. It was possible to transfer up to 10% of the atoms from the single-beam dipole trap to the crossing region. The resulting ensembles of about $4 \cdot 10^5$ atoms have a phase-space density of up to 0.045. If the dipole trap was adiabatically switched on, the phase-space density could be increased by a factor of two but an enhancement of the number of atoms in the dimple was not observed. The number of dimple atoms and the phase-space density is similar if the dimple was loaded with and without the presence of the MOT. Without the MOT the accumulation of atoms in the crossing region and therefore the increase of the phase-space density happened by elastic collisions. The number of atoms in the crossing region was limited by three-body collisions. The obtained three-body loss constant $L_3 = (3.5 \pm 0.5) \cdot 10^{-27}$ cm^6/s is comparable to other atomic species, if the ground state scattering length of ^{40}Ca is taken into account. Two- and three-body loss rates had a similar magnitude at the observed densities ($6 \cdot 10^{13}$ cm^{-3}) in the dimple. This resulted in similar phase-space densities, whether the dimple was loaded in the presence of the MOT (the density was limited by two- and three-body losses) or if the dimple was loaded in the absence of the MOT (the density was only limited by three-body losses). The loading of the dimple could be modeled by taking into account the inelastic three-body loss rate and the elastic collision rate.

At densities and temperatures where the most atomic species reach quantum-degeneracy, the observed three-body loss rate is still more than one order of magnitude smaller than the expected elastic collision rate. The achievement of a calcium BEC seems therefore promising by evaporation in a crossed-beam dipole trap. For this process the present ensemble in the dimple already seems to be a promising starting point. This shows the comparison with the experiments of ^{174}Yb [Tak03b], ^{87}Rb [Bar01] or ^{52}Cr [Gri05, Gri06], which had similar initial collisional rates and numbers of particles before the ensembles were evaporatively cooled towards quantum-degeneracy in a crossed-beam dipole trap. In this connection the comparable higher phase-space density of the calcium ensemble could be an additional advantage.

Chapter 6

Conclusion and outlook

The present thesis dealt with the realization of an optical dipole trap suitable for ^{40}Ca atoms. The main intention of using a dipole trap was to increase the phase-space density of the laser-cooled calcium ensemble as far as density limiting processes allowed this. Additionally the s-wave scattering length was determined by photoassociation spectroscopy in order to clarify the prospects for a further increase of the phase-space density by evaporative cooling in the dipole trap. As a result density limiting effects could be identified in the dipole trap. Furthermore the loading behavior and the laser cooling within the dipole trap was investigated.

Based on a model, which explains laser cooling inside a dipole trap, it could be shown that the realization of a dipole trap is best compatible with the second stage of the MOT around a magic wavelength of 1 μm. A corresponding single-beam dipole trap was realized by a Yb:YAG disc laser. At typical experimental parameters 8% ($\approx 4 \cdot 10^6$ atoms) of the atoms in the MOT could be transfered to the dipole trap. The transfer is limited by light-induced two-body losses caused by the 657 nm MOT radiation. The corresponding two-body loss coefficient β amounts to $(2.2 \pm 0.4) \cdot 10^{-13}$ cm^3/s. The light-induced losses can be attributed to the formation of Ca_2-molecules by photoassociation at the $4s^2\ ^1\mathrm{S}_0 - 4s4p\ ^3\mathrm{P}_1$ asymptote. The experimentally derived β value is in agreement with the theoretical predictions by Ciuryło *et al.* [Ciu04].

The loading dynamics of the dipole trap could be described by a model, which includes the capture rate of atoms from the MOT as well as the loss rates in the MOT and dipole trap. From the model it could be concluded, that an increase of the particle number in the dipole trap can be only expected, if the capture volume of the dipole trap is increased by a larger beam waist. Considerations to increase the particle number in the dipole trap directly by the MOT, seem to be less successful. It became possible to decrease the temperature of the atoms in the MOT or to increase their density but this was accompanied with a significant smaller number of atoms. From the loading model of the dipole trap it could be concluded, that both effects may increase the capture rate but the absolute number of atoms would be unchanged or smaller.

As a result of all these investigations, the phase-space density could be increased from $1.5 \cdot 10^{-5}$ in the second stage of the MOT to a value of $2.6 \cdot 10^{-3}$ in the single-

beam dipole trap. This could be increased further by the realization of a crossed-beam optical dipole trap. In the crossing region of both dipole traps, the so-called dimple, a phase-space density of up to 0.045 was observed. It was possible to transfer up to 10% of the atoms from the single-beam dipole trap to the crossing region. If the dipole trap was adiabatically switched on, the phase-space density could be increased by a factor of two but an enhancement of the number of atoms in the dimple was not observed. The accumulation of atoms in the crossing region and therefore the increase of the phase-space density happened by elastic collisions. The number of atoms in the crossing region was limited by three-body collisions. The obtained three-body loss constant $L_3 = (3.5 \pm 0.5) \cdot 10^{-27}$ cm^6/s is comparable to other atomic species, if the ground state scattering length of ^{40}Ca is taken into account. At densities and temperatures where the most atomic species reach quantum-degeneracy the three-body loss rate is still more than one order of magnitude smaller than the expected elastic collision rate. The achievement of a calcium BEC seems therefore promising by evaporation.

Two- and three-body loss rates had a similar magnitude at the observed densities ($6 \cdot 10^{13}$ cm^{-3}) in the dimple. This resulted in similar phase-space densities, irrespective if the dimple was loaded in the presence of the MOT (the density was limited by two- and three-body losses) or if the dimple was loaded in the absence of the MOT (the density was only limited by three-body losses).

At temperatures in the microkelvin range the elastic collision rate is determined by the s-wave scattering length. Its value was determined by photoassociation spectroscopy at the $4s^2\ ^1\mathrm{S}_0 - 4s4p\ ^1\mathrm{P}_1$ asymptote. The range of rovibrational lines was significantly increased in comparison to previous photoassociation measurements [Zin00, Deg03]. This allowed a more accurate estimation of the ground state scattering length, since an extended range of internuclear distances was accessible. The photoassociation spectra are well described by a model, which includes the molecular potentials and the experimental parameters. By the comparison between the calculated and the measured spectra it became possible to determine the range of the s-wave scattering length. Its resulting value between $340\ a_0$ and $700\ a_0$ is in good agreement with the values derived from classical molecular spectroscopy and resolves the discrepancy to previous photoassociation measurements [Deg03]. The scattering length and therefore the cross section of ^{40}Ca seems to be sufficient large in comparison to elements, which could be Bose-Einstein condensed by evaporative cooling in a crossed-beam optical dipole trap.

For the creation of a calcium BEC all relevant parameters are determined. The magnitude of the s-wave scattering length promises high elastic scattering rates in the crossed-beam optical dipole trap, which are significantly higher than the loss rates at densities (10^{14} cm^{-3}-10^{15} cm^{-3}) and temperatures ($0.1\ \mu$K - $1\ \mu$K) at which the BEC is reached in other atomic species. The realized phase-space density of 0.045 in the present ensemble of $4 \cdot 10^5$ atoms in the crossed-beam dipole trap already seems to be a promising starting point for the realization of a BEC by evaporative cooling in this trap. This shows the comparison with the experiments of ^{174}Yb [Tak03b], ^{87}Rb [Bar01] or ^{52}Cr [Gri05, Gri06], which had similar initial collisional rates and numbers of particles before the ensembles were evaporatively

cooled towards quantum-degeneracy in a crossed-beam dipole trap. In this connection, the comparable higher phase-space density of the calcium ensemble could be an additional advantage. The present setup of the crossed-beam dipole trap would allow to implement forced evaporative cooling similar to the creation of the ^{174}Yb-BEC or the ^{52}Cr-BEC. In both experiments the configuration of the crossed-beam trap is realized in such a way, that the atoms in the horizontal trap serve as reservoir. The dimple is here permanently reloaded by atoms from the horizontal trap, by decreasing the power in this trap. This ensures that the number of dimple atoms stays as long constant as atoms could be reloaded from the horizontal trap. Starting with $2 \cdot 10^5$ atoms in the dimple, this evaporation method made it possible to create a BEC of 10^5 atoms in the case of ^{52}Cr [Gri05, Gri06].

Beside this promising approach the narrow intercombination line offers the possibility for laser cooling of the atoms within the dipole trap, which operates at the magic wavelength. The quench laser would be no longer necessary, since the potential of the dipole trap supports the atoms against gravity. The velocity selectivity of the narrow line offers the possibility to achieve ensemble temperatures near the recoil limit ($T = 1.1$ μK). If the narrow-line laser cooling will be realized in a three dimensional optical lattice it could be even possible to achieve quantum-degeneracy by laser cooling. Due to the narrow linewidth of the cooling transition, the density limiting process of the reabsorption of cooling photons is expected to be small. Calculations showed that this effect will be reduced in the so-called "festina lente" regime, characterized by the condition that the scattering rate, which is proportional to the linewidth, is small in comparison to the oscillation frequencies of the lattice [Cir96, Wol00]. To avoid photoassociative losses during laser cooling in a dipole trap or in a lattice, it will be necessary, that the frequency of the cooling laser is far away from any photoassociation resonances. If laser cooling on the intercombination transition does not lead to quantum-degeneracy, an additional evaporative step can be applied as described above.

Consequently calcium offers different approaches for the generation of a BEC. As a result of this work evaporative cooling in a crossed-beam dipole trap seems to be the most promising way, which can be easily implemented in the present experimental setup.

Applications of a calcium BEC may be found in atom interferometric precision experiments such as the determination of the fine-structure constant α or the gravitational constants g and G. In atom interferometry a matter wave is divided into two paths, redirected by mirrors and beam splitters and finally overlapped. From the resulting interference pattern the phase difference of the two paths is derived, which contains the constant of interest. Beam splitters and mirrors are realized by resonant light of the intercombination transition, which has the advantage of a very narrow linewidth. Previously the $^1S_0 - ^3P_1$ transition in calcium was used in frequency measurements and the developed atom interferometric techniques as well as the knowledge of the influence of external perturbations on the transition can be of particular advantage for experiments with BECs. The high dense BEC can lead to collisional shifts of the transition, which can be detected by the phase difference in the atom interferometer and can be used to characterize the BEC. In precision ex-

periments the density can be reduced by adiabatic expansion, which further reduces the temperature and improves the spacial coherence. To increase the achievable accuracy of the atom interferometer it will be then necessary to extend the experiment time. This can be realized if the BEC will be stored in an optical dipole trap or lattice, where the atoms are supported against gravity. If the dipole trap operates at the magic wavelength of 800 nm, differential phase shifts by the light field of the dipole trap can be excluded. Furthermore magnetic stray fields can not perturb the experiment, since this wavelength of the dipole trapping laser is magic for the magnetic field insensitive transition $\Delta m = 0$.

Calcium also offers interesting perspectives for another group of experiments, which investigates the generation and the interactions of cold molecules in optical dipole traps. In this connection the photoassociation at the intercombination transition is of essential importance: on the one hand it offers the possibility to create cold Ca_2 ground state molecules and on the other hand it is possible to manipulate the scattering length in the region of a photoassociation resonance. Calculations by Ciuryło *et al.* [Ciu04] predict that molecules in highly excited vibrational states close to the $^1S_0+^3P_1$ asymptote decay with a high probability to low vibrational levels of the ground state molecule. The optical manipulation of the scattering length at a so-called optical Feshbach resonance was predicted by Fedichev *et al.* [Fed96]. In this process the scattering length of two colliding ground state atoms can be tuned by optically coupling their scattering state to an excited molecular level. The variation of the scattering length is achieved by the detuning with respect to a molecular level and by the intensity. An optically induced change in the scattering length is accompanied by a loss of atoms caused by the spontaneous decay via the excited molecular state. It is expected that these losses will be significantly smaller for ^{40}Ca [Ciu05] than for the alkaline atoms[1], due to the narrow linewidth of the photoassociation transition. A tunable interaction strength may be interesting for the creation of heteronuclear molecules e. g. of an alkaline atom and an alkaline earth atom like ^{40}Ca. The two atoms form a polar molecule due to their different electron affinity. These polar molecules not only interact via the van-der-Waals force but also via the dipole-dipole force, which has a longer interaction range. These would offer the possibility to create a cold gas of polar particles, which can be not realized in a gas of single atoms.

[1] In an experiment with ^{87}Rb by Theis *et al.* [The04] an inelastic collision rate coefficient of $1.7 \cdot 10^{-10}$ cm^3/s is observed. For ^{40}Ca Ciuryło *et al.* [Ciu05] predict a value below$1.7 \cdot 10^{-12}$ cm^3/s.

Bibliography

[All03] O. Allard, C. Samuelis, A. Pashov, H. Knöckel and E. Tiemann, "Experimental study of the Ca_2 $^1S + {}^1S$ asymptote", Eur. Phys. J. D **26**, 155 (2003).

[All04] Olivier Allard, *Long-Range Interactions in the Calcium Dimer studied by Molecular Spectroscopy*, PhD thesis, Universität Hannover, Welfengarten 1, 2004, online available at http://www.tib.uni-hannover.de.

[And95] M. H. Anderson, J. R. Ensher, M. R. Mattews, C. E. Wieman and E. A. Cornell, "Observation of Bose–Einstein Condensation in a Dilute Atomic Vapor", Science **269**, 198 (1995).

[Ang02] J. R. Anglin and W. Ketterle, "Bose-Einstein condensation of atomic gases", Nature **416**, 211 (2002).

[Bar01] M. D. Barrett, J. A. Sauer and M. S. Chapman, "All-Optical Formation of an Atomic Bose–Einstein Condensate", Phys. Rev. Lett. **87**, 010404 (2001).

[Bev89] N. Beverini, F. Giammanco, E. Maccioni, F. Strumia and G. Vissani, "Measurement of the calcium $^1P_1$-$^1D_2$ transition rate in a laser-cooled atomic beam", J. Opt. Soc. Am. B **6**, 2188 (1989).

[Bin01] T. Binnewies, G. Wilpers, U. Sterr, F. Riehle, J. Helmcke, T. E. Mehlstäubler, E. M. Rasel and W. Ertmer, "Doppler cooling and trapping on forbidden transitions", Phys. Rev. Lett. **87**, 123002 (2001).

[Blo99] I. Bloch, T. W. Hänsch and T. Esslinger, "Atom Laser with a cw Output Coupler", Phys. Rev. Lett. **82**, 3008 (1999).

[Boh99] John L. Bohn and P. S. Julienne, "Semianalytic theory of laser-assisted resonant cold collisions", Phys. Rev. A **60**, 414 (1999).

[Bos24] S. N. Bose, "Plancks Gesetz und Lichtquantenhypothese", Zeitschrift für Physik **26**, 178 (1924).

[Bra95] C. C. Bradley, C. A. Sackett, J. J. Tollet and R. G. Hulet, "Evidence of Bose-Einstein Condensation in an Atomic Gas with Attractive Interactions", Phys. Rev. Lett. **75**, 1687 (1995).

[Bur97] E. A. Burt, R. W. Ghrist, C. J. Myatt, M. J. Holland, E. A. Cornell and C. E. Wieman, "Coherence, Correlations, and Collisions: What One Learns about Bose-Einstein Condensates from Their Decay", Phys. Rev. Lett. **79**, 337 (1997).

[Bus06] B. Bussery-Honvault and R. Moszynski, "Ab initio potential energy curves, transition dipole moments and spinorbit coupling matrix elements for the first twenty states of the calcium dimer", Mol. Phys. **104**, 2387 (2006).

[Chu85] S. Chu, L. Hollberg, J. E. Bjorkholm, A. Cable and A. Ashkin, "Three-Dimensional Viscous Confinement and Cooling of Atoms by Resonance Radiation Pressure", Phys. Rev. Lett. **55**, 48 (1985).

[Cir96] J. I. Cirac, M. Lewenstein and P. Zoller, "Collective laser cooling of trapped atoms", Europhys. Lett. **35**, 647 (1996).

[Ciu04] R. Ciuryło, E. Tiesinga, S. Kotochigova and P. S. Julienne, "Photoassociation spectroscopy of cold alkaline-earth-metal atoms near the intercombination line", Phys. Rev. A **70**, 062710 (2004).

[Ciu05] R. Ciuryło, E. Tiesinga and P. S. Julienne, "Optical tuning of the scattering length of cold alkaline-earth-metal atoms", Phys. Rev. A **71**, 030701 (2005).

[Coh90] Claude N. Cohen-Tannoudji and William D. Phillips, "New Mechanisms for Laser Cooling", Phys. Today page 33 (1990).

[Cru99] A. Crubellier, O. Dulieu, F. Masnou-Seeuws, M. Elbs, H. Knöckel and E. Tiemann, "Simple determination of Na_2 scattering lengths using observed bound levels at the ground state asymptote", Eur. Phys. J. D **6**, 211 (1999).

[Cur01] E. A. Curtis, C. W. Oates and L. Hollberg, "Quenched Narrow-Line Laser Cooling of ^{40}Ca to Near the Photon Recoil Limit", Phys. Rev. A **64**, 031403(R) (2001).

[Dal99] J. Dalibard, "Collisional dynamics of ultra-cold atomic gases", Proceedings of the international school of physics "Enrico Fermi" page 321 (1999).

[Dav95] Kendall B. Davis, Marc-Oliver Mewes, Michael R. Andrews, N. J. van Druten, D. S. Durfee, D. M. Kurn and Wolfgang Ketterle, "Bose–Einstein condensation in a gas of sodium atoms", Phys. Rev. Lett. **75**, 3969 (1995).

[Deg03] Carsten Degenhardt, Tomas Binnewies, Guido Wilpers, Uwe Sterr, Fritz Riehle, Christian Lisdat and Eberhard Tiemann, "Photoassociation spectroscopy of cold calcium atoms", Phys. Rev. A **67**, 043408 (2003).

[Deg04a] Carsten Degenhardt, *Freie und gespeicherte Calcium-Atome für ein optisches Frequenznormal*, PhD thesis, Universität Hannover, Welfengarten 1, 2004, online available at http://www.tib.uni-hannover.de.

[Deg04b] Carsten Degenhardt, Hardo Stoehr, Uwe Sterr, Fritz Riehle and Christian Lisdat, "Wavelength dependent ac-Stark shift of the $^1S_0$-$^3P_1$ transition at 657 nm in Ca", Phys. Rev. A **70**, 023414 (2004).

[Deg05] Carsten Degenhardt, Hardo Stoehr, Christian Lisdat, Guido Wilpers, Harald Schnatz, Burghard Lipphardt, Tatiana Nazarova, Paul-Eric Pottie, Uwe Sterr, Jürgen Helmcke and Fritz Riehle, "Calcium optical frequency standard with ultracold atoms: Approaching 10^{-15} relative uncertainty", Phys. Rev. A **72**, 062111 (2005).

[Did04] S. A. Diddams, J. C. Bergquist, S. R. Jefferts and C. W. Oates, "Standards of Time and Frequency at the Outset of the 21st Century", Science **306**, 1318 (2004).

[Dre83] R. W. P. Drever, J. L. Hall, F. V. Kowalski, J. Hough, G. M. Ford, A. J. Munley and H. Ward, "Laser Phase and Frequency Stabilization Using an Optical Resonator", Appl. Phys. B **31**, 97 (1983).

[Edm57] A. R. Edmonds, *Angular momentum in quantum mechanics*, (Princeton University Press, Princeton, New Jersey, 1957) .

[Eie03] B. Eiermann, B. Treutlein, Th. Anker, M. Albiez, M. Taglieber, K.-P. Marzlin and M. K. Oberthaler, "Dispersion Management for Atomic Matter Waves", Phys. Rev. Lett. **91**, 060402 (2003).

[Ein25] A. Einstein, "Quantentheorie des einatomigen idealen Gases", Sitzungsberichte der Preussischen Akademie der Wissenschaften **1**, 3 (1925).

[Ert85] W. Ertmer, R. Blatt, J. L. Hall and M. Zhu, "Laser Manipulation of Atomic Beam Velocities: Demonstration of Stopped Atoms and Velocity Reversal", Phys. Rev. Lett. **54**, 996 (1985).

[Fed96] P. O. Fedichev, M. W. Reynolds and G. V. Shlyapnikov, "Three-Body Recombination of Ultracold Atoms to a Weakly Bound s Level", Phys. Rev. Lett. **77**, 2921 (1996).

[Gie94] A. Giesen, H. Hügel, A. Voss, K. Wittig, U. Brauch, H. Opower, "Scalable Concept for Diode-Pumped High-Power Solid-State Lasers", Appl. Phys. B **58**, 365 (1994).

[Gra07] Ch. Grain, T. Nazarova, C. Degenhardt, F. Vogt, Ch. Lisdat, E. Tiemann, U. Sterr and F. Riehle, "Feasibility of narrow-line cooling in optical dipole traps", Eur. Phys. J. D **42**, 317 (2007).

[Gre02] Markus Greiner, Olaf Mandel, Tilman Esslinger, Theodor W. Hänsch and Immanuel Bloch, "Quantum phase transition from a superfluid to a Mott insulator in a gas of ultracold atoms", Nature **415**, 39 (2002).

[Gri05] A. Griesmaier, J. Werner, S. Hensler, J. Stuhler and T. Pfau, "Bose-Einstein Condensation of Chromium", Phys. Rev. Lett. **94**, 160401 (2005).

[Gri06] A. Griesmaier, J. Stuhler and T. Pfau, "Production of a chromium Bose-Einstein condensate", Applied Physics B **82**, 211 (2006).

[Ham02] M. Hammes, H.-C. Nägerl D. Rychtarik and R. Grimm, "Cold-atom gas at very high densities in an optical surface microtrap", Phys. Rev. A **66**, 051401(R) (2002).

[Hän75] T. W. Hänsch and A. L. Schawlow, "Cooling of gases by laser radiation", Opt. Commun. **13**, 68 (1975).

[Han06] D. Hansen and A. Hemmerich, "Observation of Multichannel Collisions of Cold Metastable Calcium Atoms", Phys. Rev. Lett. **96**, 073003 (2006).

[Hes86] H. F. Hess, "Evaporative cooling of magnetically trapped and compressed spin-polarized hydrogen", Phys. Rev. B **34**, 3476 (1986).

[Ido00] Tetsuya Ido, Yoshitomo Isoya and Hidetoshi Katori, "Optical-dipole trapping of Sr atoms at a high phase-space density", Phys. Rev. A **61**, 061403 (2000).

[Jon06] Kevin M. Jones, Eite Tiesinga, Paul D. Lett and Paul S. Julienne, "Ultracold photoassociation spectroscopy: Long-range molecules and atomic scattering", Rev. Mod. Phys. **78**, 483 (2006).

[Kat99a] Hidetoshi Katori, Tetsuya Ido, Yoshitomo Isoya and Makoto Kuwata-Gonokami, "Magneto-optical trapping and cooling of strontium atoms down to the photon recoil temperature", Phys. Rev. Lett. **82**, 1116 (1999).

[Kat99b] Hidetoshi Katori, Tetsuya Ido and Makoto Kuwata-Gonokami, "Optimal Design of Dipole Potentials for Efficient Loading of Sr Atoms", J. Phys. Soc. Jap. **68**, 2479 (1999).

[Kis94] Th. Kisters, K. Zeiske, F. Riehle and J. Helmcke, "High-resolution spectroscopy with laser-cooled and trapped calcium atoms", Appl. Phys. B **59**, 89 (1994).

[Let88] Paul D. Lett, Richards N. Watts, Christoph I. Westbrook, William D. Phillips, Phillip L. Gould and Harold J. Metcalf, "Observation of Atoms Laser Cooled below the Doppler Limit", Phys. Rev. Lett. **61**, 169 (1988).

[Lis02] Ch. Lisdat, N. Vanhaecke, D. Comparat and P. Pillet, "Line shape analysis of two-colour photoassociation spectra on the example of the Cs_2 ground state", Eur. Phys. J. D **21**, 299 (2002).

[Mac01] Mette Machholm, Paul S. Julienne and Kalle-Antti Suominen, "Calculations of Collisions Between Cold Alkaline Earth Atoms in a Weak Laser Field", Phys. Rev. A **64**, 033425 (2001).

[Met99] Harold J. Metcalf and Peter van der Straten, *Laser Cooling and Trapping*, (Springer, New York, Berlin, Heidelberg, 1999) .

[Mic05] P. G. Mickelson, Y. N. Martinez, A. D. Saenz, S. B. Nagel, Y. C. Chen, T. C. Killian, P. Pellegrini and R. Côté, "Spectroscopic Determination of the s-Wave Scattering Lengths of ^{86}Sr and ^{88}Sr", Phys. Rev. Lett. **95**, 223002 (2005).

[Naz07] Tatiana Nazarova, *Towards the Quantum Noise Limit in Ramsey-Bordé Atom Interferometry*, PhD thesis, Fakultät für Mathematik und Physik der Gottfried Wilhelm Leibniz Universität Hannover, 2007, online available at http://www.tib.uni-hannover.de.

[Pin97] P. W. H. Pinkse, A. Mosk, M. Weidemüller, M. W. Reynolds, T. W. Hijmans and J. T. M. Walraven, "Adiabatically Changing the Phase-Space Density of a Trapped Bose Gas", Phys. Rev. Lett. **78**, 990 (1997).

[Por01] S. G. Porsev, M. G. Kozlov, Yu. G. Rakhlina and A. Derevianko, "Many-body calculations of electric-dipole amplitudes for transitions between low-lying levels of Mg, Ca, Sr", Phys. Rev. A **64**, 012508 (2001).

[Pro85] J. Prodan, A. Migdall, W. Phillips, I. So, H. Metcalf and J. Dalibard, "Stopping Atoms with Laser Light", Phys. Rev. Lett. **54**, 992 (1985).

[Raa87] E. L. Raab, M. Prentiss, A. Cable, S. Chu and D. E. Pritchard, "Trapping of Neutral Sodium Atoms with Radiation Pressure", Phys. Rev. Lett. **59**, 2631 (1987).

[Rus98] F. Ruschewitz, J. L. Peng, H. Hinderthür, N. Schaffrath, K. Sengstock and W. Ertmer, "Sub-Kilohertz Optical Spectroscopy with a Time Domain Atom Interferometer", Phys. Rev. Lett. **80**, 3173 (1998).

[Sta98] D. M. Stamper-Kurn, H.-J. Miesner, A. P. Chikkatur, S. Inouye, J. Stenger and W. Ketterle, "Optical Confinement of a Bose-Einstein Condensate", Phys. Rev. Lett. **80**, 2027 (1998).

[Sto04] Hardo Stoehr, *Diodenlaser mit Hertz-Linienbreite für ein optisches Calcium-Frequenznormal*, PhD thesis, Universität Hannover, Welfengarten 1, 2004, online available at http://www.tib.uni-hannover.de.

[Tak03a] Masao Takamoto and Hidetoshi Katori, "Spectroscopy of the $^1S_0 \rightarrow {}^3P_0$ Clock Transition of ^{87}Sr in an Optical Lattice", Phys. Rev. Lett. **91**, 223001 (2003).

[Tak03b] Yosuke Takasu, Kenichi Maki, Kaduki Komori, Tetsushi Takano, Kazuhito Honda, Mitsutaka Kumakura, Tsutomu Yabuzaki and Yoshiro Takahashi, "Spin-Singlet Bose–Einstein Condensation of Two-Electron Atoms", Phys. Rev. Lett. **91**, 040404 (2003).

[Tak04] Y. Takasu, K. Komori, K. Honda, M. Kumakura, T. Yabuzaki and Y. Takahashi, "Photoassociation Spectroscopy of Laser-Cooled Ytterbium Atoms", Phys. Rev. Lett. **93**, 123202 (2004).

[The04] M. Theis, G. Thalhammer, K. Winkler, M. Hellwig, G. Ruff, R. Grimm and J. Hecker Denschlag, "Tuning the Scattering Length with an Optically Induced Feshbach Resonance", Phys. Rev. Lett. **93**, 123001 (2004).

[Tie96] Eite Tiesinga, Carl J. Williams, Paul S. Julienne, Kevin M. Jones, Paul D. Lett and William D. Phillips, "A Spectroscopic Determination of Scattering Lengths for Sodium Atom Collisions", J. Res. Natl. Inst. Stand. Technol. **101**, 505 (1996).

[Toj06] Satoshi Tojo, Masaaki Kitagawa, Katsunari Enomoto, Yutaka Kato, Yosuke Takasu, Mitsutaka Kumakura and Yoshiro Takahashi, "High-Resolution Photoassociation Spectroscopy of Ultracold Ytterbium Atoms by Using the Intercombination Transition", Phys. Rev. Lett. **96**, 153201 (2006).

[Trä07] F. Träger (editor), *Springer Handbook of Lasers and Optics*, (Springer, New York, Berlin, Heidelberg, 2007).

[Vog99] Kurt R. Vogel, Timothy P. Dinneen, Alan Gallagher and John L. Hall, "Narrow-Line Doppler Cooling of Strontium to the Recoil Limit", IEEE Trans. Instrum. Meas. **48**, 618 (1999).

[Wal89] H. Wallis and W. Ertmer, "Broadband laser cooling on narrow transitions", J. Opt. Soc. Am. B **6**, 2211 (1989).

[Web03a] Tino Weber, Jens Herbig, Michael Mark, Hanns-Christoph Nägerl and Rudolf Grimm, "Bose–Einstein Condensation of Cesium", Science **299**, 232 (2003).

[Web03b] Tino Weber, Jens Herbig, Michael Mark, Hanns-Christoph Nägerl and Rudolf Grimm, "Three-Body Recombination at Large Scattering Lengths in an Ultracold Atomic Gas", Phys. Rev. Lett. **91**, 123201 (2003).

[Wei99] J. Weiner, V. S. Bagnato, S. Zilio and P. S. Julienne, "Experiments and theory in cold and ultracold collisions", Rev. Mod. Phys. **71**, 1 (1999).

[Wes04] R. Wester, S.D. Kraft, M. Mudrich, M.U. Staudt, J. Lange, N. Vanhaecke, O. Dulieu and M. Weidemüller, "Photoassociation inside an optical dipole trap: absolute rate coefficients and Franck–Condon factors", Appl. Phys. B **79**, 993 (2004).

[Wol00] Steffen Wolf, Steven J. Oliver and David S. Weiss, "Suppression of Recoil Heating by an Optical Lattice", Phys. Rev. Lett. **85**, 4249 (2000).

[Yas06] Masami Yasuda, Tetsuo Kishimoto, Masao Takamoto and Hidetoshi Katori, "Photoassociation spectroscopy of ^{88}Sr: Reconstruction of the wave function near the last node", Phys. Rev. A **73**, 011403 (2006).

[Zel06] T. Zelevinsky, M. M. Boyd, A. D. Ludlow, T. Ido, J. Ye, R. Ciuryło, P. Naidon and P. S. Julienne, "Narrow Line Photoassociation in an Optical Lattice", Phys. Rev. Lett. **96**, 203201 (2006).

[Zin00] G. Zinner, T. Binnewies, F. Riehle and E. Tiemann, "Photoassociation of cold Ca atoms", Phys. Rev. Lett. **85**, 2292 (2000).

List of Publications

Parts of this thesis were published and presented in advance in journals and on conferences.

Publications in refereed journals

1. Ch. Grain, T. Nazarova, C. Degenhardt, F. Vogt, Ch. Lisdat, E. Tiemann, U. Sterr, and F. Riehle, *Feasibility of narrow-line cooling in optical dipole traps*, Eur. Phys. J. D **42**, 317-324 (2007).

2. F. Vogt, Ch. Grain, T. Nazarova, U. Sterr, F. Riehle, Ch. Lisdat, and E. Tiemann, *Determination of the calcium ground state scattering length by photoassociation spectroscopy at large detunings*, Highlight Paper, Eur. Phys. J. D **44**, 73-79 (2007).

Conference contributions

1. Spring meeting of the Deutsche Physikalische Gesellschaft 2009, Hamburg, O. Appel, F. Vogt, U. Sterr, F. Riehle, *Auf dem Weg zum Calcium-BEC* (oral).

2. Spring meeting of the Deutsche Physikalische Gesellschaft 2008, Darmstadt, F. Vogt, J. S. R. Vellore Winfred, U. Sterr, F. Riehle, *Ladedynamik optischer Dipolfallen bei Erdalkaliatomen* (poster).

3. Spring meeting of the Deutsche Physikalische Gesellschaft 2007, Düsseldorf, F. Vogt, Ch. Grain, T. Nazarova, U. Sterr, F. Riehle, Ch. Lisdat, E. Tiemann, *Bestimmung der Grundzustandsstreulänge von ^{40}Ca mit Photoassoziationsspektroskopie* (poster).

4. Workshop on Quantum Engineering based on Atoms and Photons 2007, Hannover, F. Vogt, Ch. Grain, T. Nazarova, U. Sterr, F. Riehle, Ch. Lisdat, E. Tiemann, *Determination of the ground state scattering length of by ^{40}Ca photoassociation spectroscopy* (poster).

5. 16. Norddeutscher Lasertag 2006, Hannover, F. Vogt, Ch. Grain, T. Nazarova, U. Sterr, F. Riehle, Ch. Lisdat, E. Tiemann, *Determination of the Ca Scattering Length by photoassociation spectroscopy* (poster).

6. Spring meeting of the Deutsche Physikalische Gesellschaft 2006, Frankfurt, F. Vogt, Ch. Grain, C. Degenhardt, Ch. Lisdat, T. Nazarova, U. Sterr, F. Riehle, *Laserkühlung auf schmalen Linien in optischen Dipolfallen* (oral).

7. Workshop on Quantum Engineering with Photons, Atoms and Molecules 2005, Les Houches, France, Felix Vogt, Carsten Degenhardt, Christian Lisdat, Tatiana Nazarova, Christophe Grain, Uwe Sterr, and Fritz Riehle, *Optical Dipole Traps for Calcium Atoms* (poster).

Danksagung

Hiermit möchte ich allen danken, die zum Gelingen dieser Arbeit beigetragen haben. Mein besonderer Dank gilt:

- Herrn Prof. Dr. Wolfgang Ertmer für die Betreuung dieser Arbeit von Seiten der Universität Hannover und für die Leihgabe des Yb:YAG-Scheibenlasers mit dessen Hilfe die Untersuchungen in der Dipolfalle durchgeführt werden konnten. Auch möchte ich Herrn Prof. Dr. Ertmer stellvertretend für die Anregungen und den Erfahrungsaustausch innerhalb des Sonderforschungsbereichs 407 danken.

- Herrn Prof. Dr. Fritz Riehle für die Betreuung dieser Arbeit von Seiten der Physikalisch-Technischen Bundesanstalt, sein Engagement und seine stete Hilfsbereitschaft.

- Herrn Dr. Uwe Sterr für die vielen Anregungen und Diskussionen rund um diese Arbeit in experimenteller wie theoretischer Hinsicht.

- Herrn Prof. Dr. Eberhard Tiemann, Herrn PD Dr. Christian Lisdat und Herrn Dr. Christophe Grain für die erfolgreiche Zusammenarbeit während der Experimente zur Photoassoziation und darüberhinaus.

- Frau Dr. Tatiana Nazarova und Herrn Dipl.-Phys. Oliver Appel für die erfolgreiche Zusammenarbeit im Calcium Labor.

- Herrn Dr. Sebastian Kraft für das Korrekturlesen einiger Teile dieser Arbeit.

- Frau Dr. Gesine Grosche für die ein oder andere Diskussionsmöglichkeit.

- Herrn Patrik Knigge und Herrn Klemens Budin für die Herstellung der ungezählten mechanischen Teile.

- Herrn Dipl.-Ing. Mattias Misera und Herrn Dipl.-Ing Friedhelm Mensing für die Herstellung zahlreicher elektronischer Bauteile.

- Frau Birgit Voss, Frau Elke Hünitzsch, Frau Katrin Pfennig sowie Frau Gunhild Faber für die freundliche Unterstützung in administrativen Fragen.

- Meinen Eltern für die stete Unterstützung.

Diese Arbeit wurde gefördert von der Deutschen Forschungsgemeinschaft im Rahmen des Sonderforschungsbereichs 407 *Quantenlimitierte Messprozesse mit Atomen, Molekülen und Photonen*.